UNIVERSITY *of* TASMANIA | AMC Australian Maritime College

THE HYDRODYNAMIC AND STRUCTURAL LOADING CHARACTERISTICS OF STRAIGHT AND HELICAL-BLADED VERTICAL AXIS TIDAL AND CURRENT FLOW TURBINES

by

Philip John Marsh, B.E. B.A. M.Phil

National Centre for Maritime Engineering and Hydrodynamics
Australian Maritime College

Submitted in fulfilment of the requirements for the degree of Doctor of Philosophy

University of Tasmania
October, 2015

Declarations

I declare that this thesis contains no material which has been accepted for a degree or diploma by the University or any other institution, except by way of background information and duly acknowledged in the thesis, and that, to the best of my knowledge and belief, this thesis contains no material previously published or written by another person, except where due acknowledgement is made in the text of the thesis.

This thesis may be made available for loan and limited copying in accordance with the *Copyright Act 1968*

Signed: _____
Philip John Marsh

Date: 28/10/2015

Statement of Published Work Contained in Thesis

The publishers of the papers comprising Chapters 3, 5, 6, A1 and A2 hold the copyright for that content, and access to the material should be sought from the respective journals and conference proceedings. The remaining non published content of the thesis, Chapters 2, 4 and 7 are submitted and under review, and may be made available for loan and limited copying and communication in accordance with the Copyright Act 1968.

Statement of Co-Authorship

The following people and institutions contributed to the publication of work undertaken as part of this thesis:

- Philip John Marsh, University of Tasmania (Candidate)
- Professor Dev Ranmuthugala, University of Tasmania (Author 1)
- Associate Professor Irene Penesis, University of Tasmania (Author 2)
- Professor Giles Thomas, University College London (Author 3)

For all works the Candidate was the primary author. Author 1, Author 2, and Author 3 assisted with research direction, advice, and presentation. [Candidate: 70%, Author 1: 10%, Author 2: 10%, Author 3: 10%]

We the undersigned agree with the above stated proportion of work undertaken for each of the published (or submitted) peer-reviewed manuscripts contributing to this thesis

Signed:

Professor Dev Ranmuthugala
Primary Supervisor
National Centre for Ports and Shipping
Australian Maritime College
University of Tasmania

Associate Professor Irene Penesis
Co-Supervisor
National Centre for Maritime Engineering and Hydrodynamics
Australian Maritime College
University of Tasmania

Professor Giles Thomas
Co-Supervisor
Department of Mechanical Engineering
University College London

Acknowledgements

First and foremost this work has been fun! Initial trepidation was quickly replaced by enjoyment due to the support, encouragement, and inspiration of all those who made this work possible.

I would like to thank my supervisory team, Dev Ranmuthugala, Irene Penesis, and Giles Thomas. The support over the last few years has been amazing. Throughout my thesis you have provided incredible levels of inspiration, encouragement, and guidance. The work environment created by your support was perfect. It's been a great experience to work with you; the level of development of not only my research but also my academic and professional skills is invaluable.

Special thanks go to Luciano Mason for the computational assistance, the insightful questions, and cups of coffee. Our daily discussions were a joy, and kept me amused, up to date, and certainly well caffeinated. I wish you all the best in the future and hope to be sitting at your coffee table soon. And that's after lunch with Konrad Zurcher, to whom I also owe many thanks!

Thanks must also go to Geli Kourakis and Jonathan Binns for their assistance with the computational cluster facilities, without which this work would not have been possible. Thanks also to the fellow CFD'ers at the AMC; Zhi Quan Leong, Max Haase, Alex Ashworth-Briggs, Alex Conway, and Christopher Polis. The CFD discussions, assistance, and even celebrations of victories created a work environment that has been a joy.

Lastly, thanks to Debbie, my love. This work is dedicated to you.

Abstract

Vertical axis cross flow tidal and current flow turbines are proposed to generate electrical energy from the ocean's kinetic energy, however little is known of their performance and loading characteristics. In this work, fixed pitch straight and helical-bladed vertical axis turbines were investigated using numerical simulation models to perform examinations of the influence of geometrical layout and rotational rate on power output, torque fluctuations, mounting forces, structural stress, and deflection magnitudes. These studies were conducted to establish the relative merits of various turbine configurations, including variations in strut section, strut-blade mounting tab design, strut location, as well as varying degrees of blade helicity and section angle inclination. To establish performance and loading parameters, transient Computational Fluid Dynamics (CFD) and Double Multiple Streamtube (DMS) hydrodynamic simulation models were developed, which were then coupled with structural models using beam theory and Finite Element Analysis (FEA) techniques. Extensive verification and validation of the hydrodynamic results against Experimental Fluid Dynamics (EFD) results from literature for turbines of differing geometrical layouts was performed to ensure simulation accuracy.

Simulation results show that numerical models can accurately simulate performance when compared to EFD results if suitable modelling techniques are utilised. The results show that significant differences in performance characteristics such as power output and mounting force magnitudes occur for turbines with differing geometrical layouts. Straight-bladed turbines were found to generate higher power output, torque fluctuation levels, mounting forces, structural stress, and deflection magnitudes than helical turbines of the same frontal area, as a result of the blade inclination of the helical turbine to the inflow. The influence of strut design on power output was also significant, with low-drag struts located at the blade tips generating the highest power output when compared to turbines with high-drag struts located at the quarter-span location. For both straight and helical turbines the highest stress magnitudes were found at the blade-strut joints. Overall these results demonstrate that straight-bladed turbines are better suited for harnessing tidal and current flow ocean energy than helical-bladed turbines, as they generate higher power outputs whilst not incur-

ring any significantly adverse structural penalties. These results are significant as previous numerical simulation and EFD works have concentrated on each configuration individually, with little known of their respective merits.

The numerical models developed as part of this work are capable of accurately capturing the complex behaviour of vertical axis turbines for differing geometrical layouts, allowing for future design investigations to be conducted without the need for EFD. The development of these models, and the inclusion of suggested simulation guidelines in this work, has created a useful design toolbox for future use that is suitable for turbine optimisation studies as well as coupling with fatigue evaluations to ensure turbine longevity.

TABLE OF CONTENTS

LIST OF FIGURES **xiv**

LIST OF TABLES **xxii**

NOMENCLATURE **xxiv**

ABBREVIATIONS **xxviii**

1 THESIS INTRODUCTION **1**

1.1 Introduction 2

1.1.1 Problem Definition 3

1.1.2 Objectives 6

1.2 Geometric Models 7

1.3 Methodology 8

1.4 Key Considerations 10

1.4.1 Hydrodynamic Considerations 10

1.4.2 Structural Loading Considerations 10

1.4.3 Geometric Considerations 11

1.4.4 Assumptions and Limitations 11

1.5 Novel aspects 12

1.6 Thesis Outline 13

2 THE INFLUENCE OF TURBULENCE MODEL AND TWO AND THREE-DIMENSIONAL DOMAIN SELECTION ON THE SIMULATED PERFORMANCE CHARACTERISTICS OF VERTICAL AXIS TURBINES 17

Abstract . . . 18

2.1 Introduction . . . 18

2.2 Numerical Simulation . . . 20

2.2.1 Turbine Geometry . . . 20

2.2.2 Key Performance Parameters . . . 21

2.2.3 Turbulence and Boundary Layer Modeling . . . 22

2.2.4 Computational Fluid Dynamics (CFD) Models . . . 24

2.2.5 Mesh Independence Studies . . . 26

2.3 Results and Discussion . . . 30

2.3.1 Computational Fluid Dynamics Simulations . . . 31

2.3.2 Computational Requirements and Numerical Simulation Recommendations . . . 35

2.3.3 Numerical Simulation Recommendations . . . 36

2.3.4 Geometrical Effects on Power Output . . . 36

2.3.5 Flow Visualisation . . . 37

2.4 Conclusions . . . 38

3 THREE-DIMENSIONAL NUMERICAL SIMULATIONS OF STRAIGHT-BLADED VERTICAL AXIS TIDAL TURBINES INVESTIGATING POWER OUTPUT, TORQUE RIPPLE AND MOUNTING FORCES 39

Abstract . . . 40

3.1 Introduction . . . 40

3.2 Numerical Simulations . . . 43

3.2.1 Turbine Geometry . . . 43

3.2.2 Key Performance Parameters . . . 43

3.2.3 Computational Domain and Boundary Conditions . . . 45

3.2.4 Turbulence Model and Discretisation Schemes 46
3.2.5 Grid Independence Studies 47
3.2.6 Numerical Simulation Time 52
3.3 Results and Discussion 52
3.3.1 Validation of Numerical Simulations with Experimental Fluid Dynamics 52
3.3.2 Numerical Simulation of Power Output 54
3.3.3 Influence of Strut Section and Blade-Strut Joint Design 55
3.3.4 Influence of Strut Location 56
3.3.5 Vortex Shedding Visualisation 56
3.3.6 Torque Ripple Simulations 57
3.3.7 Turbine Mounting Force Simulations 60
3.3.8 Validation of Inline Forces with Experimental Fluid Dynamics 60
3.3.9 Inline and Lateral Force Simulations 62
3.4 Conclusions 62

4 COMPARISONS BETWWEEN DMS AND CFD BLADE FORCE SIMULATIONS OF STRAIGHT-BLADED VERTICAL AXIS TIDAL TURBINES 64

Abstract 65
4.1 Introduction 65
4.2 Numerical Simulation 66
4.2.1 Turbine Geometry 67
4.2.2 Double Multiple Streamtube Model 68
4.2.3 Computational Fluid Dynamics Models 72
4.3 Results 77
4.3.1 Flow Visualisation 79
4.3.2 Computational Requirements 80
4.4 Conclusions 81

5 NUMERICAL SIMULATION OF STRAIGHT-BLADED VERTICAL AXIS TIDAL TURBINES 82

Abstract . . . 83

5.1 Introduction . . . 83

5.2 Numerical Simulation . . . 84

5.2.1 Turbine Geometry . . . 85

5.2.2 Computational Fluid Dynamics Models . . . 85

5.2.3 Key Performance Parameters . . . 89

5.2.4 Mesh Independence Studies . . . 89

5.2.5 Double Multiple Streamtube Model . . . 92

5.3 Results . . . 93

5.3.1 Computational Fluid Dynamics Simulations . . . 93

5.3.2 Double Multiple Streamtube Simulations . . . 96

5.3.3 Maximum Power Output Predictions . . . 97

5.3.4 Geometrical Effects on Power Output . . . 98

5.3.5 Flow Visualisation . . . 99

5.3.6 Computational Requirements . . . 99

5.3.7 Numerical Simulation Guidelines . . . 100

5.4 Conclusions . . . 100

6 NUMERICAL INVESTIGATION OF THE INFLUENCE OF BLADE HELICITY ON THE PERFORMANCE CHARACTERISTICS OF VERTICAL AXIS TIDAL TURBINES 102

Abstract . . . 103

6.1 Introduction . . . 103

6.2 Turbine Geometry . . . 105

6.3 Numerical Simulation Methodology . . . 108

6.4 Validation Studies . . . 112

6.5 Computational Requirements . . . 115
6.6 Results and Discussion . . . 115
6.6.1 Influence of helicity on power output . . . 115
6.6.2 Influence of blade section inclination on power output . . . 117
6.6.3 Influence of helicity on torque oscillation levels . . . 118
6.6.4 Influence of helicity on turbine mounting forces . . . 121
6.7 Conclusions . . . 125

7 NUMERICAL SIMULATION OF THE LOADING CHARACTERISTICS OF STRAIGHT AND HELICAL-BLADED VERTICAL AXIS TIDAL TURBINES 127

Abstract . . . 128
7.1 Introduction . . . 128
7.2 Turbine Geometry . . . 130
7.3 Numerical Simulation Methods . . . 131
7.3.1 Hydrodynamic Simulations . . . 131
7.3.2 Structural Simulations . . . 135
7.4 Results and Discussion . . . 138
7.4.1 Normal and Tangential Force Coefficients . . . 138
7.4.2 Straight-Bladed Turbine Loading and Deflection Simulations . . . 140
7.4.3 Helical Turbine Normal Force Coefficients . . . 145
7.4.4 Helical Turbine Loading and Deflection . . . 147
7.4.5 Straight and Helical Bladed Turbine Loading Comparisons . . . 150
7.4.6 Computational Requirements . . . 151
7.5 Conclusions . . . 152

8 SUMMARY, CONCLUSIONS AND FUTURE WORK 153

8.1 Summary and Conclusions . . . 154
8.2 Findings and Limitations . . . 155

8.2.1 Geometrical Findings 156

8.2.2 Numerical Simulation Models Findings and Limitations 156

8.3 Future Work 160

8.4 Implications for the future 161

REFERENCES **162**

A APPENDIX A: Three Dimensional Numerical Simulations of a Straight-Bladed Vertical Axis Tidal Turbine **167**

B APPENDIX B: Performance Predictions of a Straight-Bladed Vertical Axis Turbine Using Double-Multiple Streamtube and Computational Fluid Dynamics Models **188**

LIST OF FIGURES

1.1 Vertical axis turbine used for tidal and current power generation showing definition of blades, struts and shaft, along with location of generator and drivetrain above the waters surface (*New Energy Corporation* 2014) 2

1.2 Examples of (a) straight (*T-Vision* 2015) and (b) helical-bladed (*Vertical Axis Wind Turbines vs Horizontal Axis Wind Turbines* 2015) vertical axis turbine configurations 5

1.3 Validation CFD models showing (a) one-bladed (Strickland et al. 1979, Webster 1978), (b) Lucid helical (Bachant 2011, Bachant & Wosnik 2015), (c) and (d) Rawlings three-bladed (Rawlings 2008), (e) AMC three-bladed, and (f) three-bladed (Strickland et al. 1979, Webster 1978) turbines (struts not modelled - see Chapters 4 and 5) 8

1.4 Straight (a) and helical-bladed turbine showing geometrical notations and definition of blade overlap angle ϕ 9

1.5 Definition of section inclination angle of the blade sections to the horizontal rotation plane for the 15° helical turbine 9

1.6 Definitions of lateral, inline, and vertical forces 11

2.1 Vertical axis turbine showing definitions of key geometrical features 19

2.2 Turbine A and B strut section and location detail. Dimensions in mm (Rawlings 2008) 21

2.3 Blade surface inflation layer mesh density for: (a) k-ω SST Wall Function and (b) fully resolved 3D k-ω SST models showing differences in mesh density with 10 and 30 layers respectively 23

2.4 Example of C_p convergence for Turbine A at λ=2.75 at an inflow velocity of 1.5 ms^{-1} 24

2.5 Mesh domain for 3D model showing overall mesh domain, GGI interface, and inflation layer detail on the blade surface for the 3D k-ω SST Turbine A model 25

2.6 Domain nomenclature and sizing for the (a) half, and (b) full 3D CFD models. Dimensions in turbine diameter d and span s 26

2.7 Domain boundary nomenclature and sizing for 2D domain. Total 2D domain thickness of 0.01m. Dimensions in turbine diameter *d*. Symmetry on both horizontal surfaces 27

2.8 Mesh element count independence for Turbine A CFD models at λ=2.75 and an inflow velocity of 1.5 ms^{-1}. Results for 2D SST model shown on right for clarity 27

2.9 Time Independence for Turbine A CFD models at λ=2.75 and an inflow velocity of 1.5 ms^{-1} 28

2.10 Non-dimensional first cell height ($y+$) independence study for Turbine A at λ=2.75 and an inflow velocity of 1.5 ms^{-1}. The optimal $y+$ was approximately $y+$=0.75, except for the 3D k-ω SST Wall Function model where optimal $y+$=29 29

2.11 Comparison of first and second order numerical discretisation schemes with EFD C_p with error bars from literature for Turbine A at an inflow velocity of 1.5 ms^{-1} and λ=2.75 (Rawlings 2008) 30

2.12 Comparison of $C_p - \lambda$ curves for Turbine A at an inflow velocity of 1.5 ms^{-1}. EFD results with error bars from literature (Rawlings 2008) 31

2.13 Comparison of $C_p - \lambda$ curves for Turbine B at an inflow velocity of 1.5 ms^{-1}. EFD results from literature (Rawlings 2008) 32

2.14 Comparison of the increase in wall shear stress simulated by the 3D k-ω SST fully turbulent model when compared to the 3D k-ω SST Transitional models, Turbine A at λ=3.5 at an inflow velocity of 1.5 ms^{-1} 34

2.15 Vortex structure visualisation for Turbine A at λ=2.75 for the 2D k-ω SST model. Vorticity in stationary frame from 1 to 20 s^{-1} at an inflow velocity of 1.5 ms^{-1} 37

2.16 Vortex shedding visualisation for Turbine A at λ=2.75 for the 3D k-ω SST model. Vorticity of 16 s^{-1} at an inflow velocity of 1.5 ms^{-1} at λ=2.75 37

3.1 Vertical Axis turbine for tidal and current power generation (*New Energy Corporation* 2014) 41

3.2 Turbines A, B, and C strut section, strut location and blade-strut joint detail (Rawlings 2008) 44

3.3 Domain boundary nomenclature and sizing, dimensions in turbine diameters D. Plane of symmetry on bottom surface 45

3.4 Mesh domain showing overall mesh domain, GGI interface, and inflation layer detail on the blade surface 46

3.5 Mesh density independence study for Turbine A at an inflow velocity of 1.5 ms^{-1} and λ=2.75 48

3.6 Comparison of mesh density on surfaces of blades and struts between (a) 8.5 million and (b) 27 million elements 48

3.7 Time step independence study for Turbine A at an inflow velocity of 1.5 ms^{-1} and λ=2.75 49

3.8 Comparison of flow velocity for domain heights of 1.25D and 2.5D showing increase in velocity due to flow constriction, Turbine A at an inflow velocity of 1.5 ms^{-1} and λ=2.75 50

3.9 Velocity in stationary frame comparisons for half domain and full domain for Turbine A at an inflow velocity of 1.5 ms^{-1} and λ=2.75 51

3.10 Comparison of CFD and EFD $C_p - \lambda$ curves for Turbines A and B at an inflow velocity of 1.5 ms^{-1}. Error bars only reported for EFD Turbine A (Rawlings 2008) 54

3.11 Comparisons of CFD $C_p - \lambda$ curves for Turbines A, B, and C at an inflow velocity of 1.5 ms^{-1} 55

3.12 Blade tip and strut vortex structures for Turbine A and C, vorticity in stationary frame of 25 s^{-1} at an inflow velocity of 1.5 ms^{-1} and λ=2.75. Vortex strength of 25 s^{-1} chosen solely to illustrate differences between Turbines A and C 57

3.13 Vortex structure visualisation for Turbine B at λ=1.5 and λ=2.75 showing vortex generation. Time series of isosurfaces of vorticity in stationary frame from 9 to 35 s^{-1} at an inflow velocity of 1.5 ms^{-1} on plane 0.05m from horizontal symmetry 58

3.14 Torque Ripple Factor (TRF) determination for Turbine A at an inflow velocity of 1.5 ms^{-1} and λ=2.75 59

3.15 Comparison of CFD Torque Ripple Factor (TRF) for Turbines A, B, and C at an inflow velocity of 1.5 ms^{-1} 60

3.16 Definitions of lateral, inline and vertical forces 61

3.17 Comparison of average CFD and EFD inline force coefficients for Turbine B at an inflow velocity of 1.5 ms^{-1} (Rawlings 2008) 61

3.18 Comparisons of average inline, average lateral and maximum force coefficients for Turbines A, B, and C at an inflow velocity of 1.5 ms^{-1} 62

4.1 Three-bladed turbine (a) geometrical details and (b) force nomenclature showing normal (F_n) and tangential (F_t) force coefficient definitions. Dimensions in m (Strickland et al. 1979, Webster 1978) 67

4.2 DMS Streamtube Model showing an example of the streamtube method for calculation of upstream and downstream flow values $V_{\infty i}$, V, V_e and V through one streamtube 68

4.3 Flowchart of DMS iteration process 73

4.4 Domain boundary nomenclature and sizing. Dimensions in meters (m) and turbine diameters (D) 74

4.5 Mesh element count independence for three-bladed turbine at a rotational rate of 0.746 rads^{-1} and an inflow velocity of 0.091 ms^{-1} 76

4.6 Time independence for the three-bladed turbine at a rotational rate of 0.746 rads^{-1} and an inflow velocity of 0.091 ms^{-1} 76

4.7 Normal (a) and tangential (b) force coefficients for the one-bladed turbine compared to EFD results (Strickland et al. 1979, Webster 1978) at a rotational rate of 0.746 rads^{-1} and an inflow velocity of 0.091 ms^{-1} 78

4.8 Normal (a) and tangential (b) force coefficients for the three-bladed turbine compared to EFD results (Strickland et al. 1979, Webster 1978) at a rotational rate of 0.746 rads^{-1} and an inflow velocity of 0.091 ms^{-1} 79

4.9 Vortex shedding comparisons between (a) one and (b) three-bladed turbines at a rotational rate of 0.746 rads^{-1} and an inflow velocity of 0.091 ms^{-1} . . . 80

4.10 Influence of boundary walls on tip vortex generation of three-bladed turbine at a rotational rate of 0.746 rads^{-1} and an inflow velocity of 0.091 ms^{-1}. Isosurfaces of vorticity of 0.5 s^{-1} 81

5.1 Turbine A and B strut section and location detail. Dimensions in mm 85

5.2 Detail of meshing of 3D k-ω SST model showing: (a) full domain, (b) rotating domain, (c) meshing of blades and shaft and (d) inflation layer detail on the blades 86

5.3 Inflation layer mesh density for (left) wall function and (right) fully resolved 3D CFD models 87

5.4 Domain boundary nomenclature and sizing for 3D models. Dimensions in turbine diameter D 88

5.5 Domain boundary nomenclature and sizing for 2D domain. Total 2D domain thickness of 0.01m. Dimensions in turbine diameter D 88

5.6 Element count independence for Turbine A CFD models at λ=2.75 and an inflow velocity of 1.5 ms^{-1} 90

5.7 Time Independence for Turbine A CFD models at =2.75 and an inflow velocity of 1.5 ms^{-1} 91

5.8 Non-dimensional first cell height ($y+$) independence study for Turbine A at λ=2.75 and an inflow velocity of 1.5 ms^{-1} 92

5.9 DMS Streamtube Model showing an example of the streamtube method for calculation of upstream and downstream flow values V_1 and V_2 93

5.10 Comparison of $C_p - \lambda$ curves for Turbine A at an inflow velocity of 1.5 ms^{-1} 94

5.11 Comparison of $C_p - \lambda$ curves for Turbine B at an inflow velocity of 1.5 ms^{-1} 95

5.12 Comparison of Turbine A DMS model with EFD and CFD $C_p - \lambda$ curves at an inflow velocity of 1.5 ms^{-1} 96

5.13 Turbine A and B $C_p - \lambda$ curves using 3D k-ω SST CFD models at an inflow velocity of 1.5 ms^{-1} 98

5.14 Vortex Structure visualisation for Turbine B at λ=1.5 showing downstream vortex convection. Isosurfaces of vorticity at an inflow velocity of 1.5 ms^{-1} . 99

6.1 Straight (a) and helical (b) bladed vertical axis turbines, including the definition of the helical blade overlap angle, ϕ 104

6.2 Definition of section inclination angle of the NACA634021 blade section to the horizontal rotation plane 107

6.3 Example of C_p convergence for the 0° turbine at λ=2.75 at an inflow velocity of 1.5 ms^1 110

6.4 Domain boundary nomenclature and sizing for (a) symmetrically reduced and (b) full domain. Dimensions in relation to turbine diameter, D, and span, S . 111

6.5 Example of spatial and temporal independence for the 0° and 15° blade overlap turbines at λ=2.75 at an inflow velocity of 1.5 ms^1 112

6.6 Comparison of CFD and EFD $C_p - \lambda$ curves for Lucid turbine at an inflow velocity of 1 ms^1 (Bachant 2011, Bachant & Wosnik 2015) 113

6.7 Comparison of CFD and EFD $C_p\lambda$ curves for the 0° and 0°A turbines at an inflow velocity of 1.5 ms^{-1}. Error bars only reported for Turbine 0° (Rawlings 2008) 114

6.8 Comparison of CFD $C_p - \lambda$ curves for blade overlap angles from 0° to 120° at an inflow velocity of 1.5 ms^{-1} 116

6.9 Comparison of inclination of flow for 0°, 60°, and 120° overlap angle turbines at an inflow velocity of 1.5 ms^{-1}, λ=2.75 116

6.10 Vortex shedding comparisons between the 60° and 0° overlap angle turbines, vorticity of 16 s^{-1} at an inflow velocity of 1.5 ms^{-1} at λ=2.75 117

6.11 Section inclination effects on the $C_p-\lambda$ curves of the 15° overlap angle turbines with section inclination angles of -15°, 0°, +15°, +30° and +45° at an inflow velocity of 1.5 ms^{-1} 118

6.12 Variations in C_m for one revolution for the 0° and 60° overlap angle turbines at an inflow velocity of 1.5 ms^{-1} at λ=2.75 119

6.13 Angle of attack variations with span for the 0° and 60° overlap angle turbines at an inflow velocity of 1.5 ms^{-1} at λ=2.75 119

6.14 Comparisons of $TRF - \lambda$ for varying overlap angles turbines from 0° to 120° at an inflow velocity of 1.5 ms^{-1} 120

6.15 Comparisons of TRF- for 15° overlap angle helical turbines with section inclination angles from 15° to 45° at an inflow velocity of 1.5 ms^{-1} 121

6.16 Definitions of lateral, inline, and vertical force vectors for the 3D CFD domains 122

6.17 Comparison of average CFD and EFD inline force coefficient, C_{FX}, for the 0° blade overlap (Rawlings 2008) and Lucid (Bachant 2011, Bachant & Wosnik 2015) turbine at an inflow velocity of 1.5 ms^{-1}. Lucid error bars reported in EFD (Bachant & Wosnik 2015), no error bars reported in EFD for 0° blade overlap turbine (Rawlings 2008) 123

6.18 Comparison of average inline, C_{FX}, lateral, C_{FY}, vertical, C_{FZ}, and maximum, force coefficients, C_{FMax} for the 0° and 15° overlap angle helical turbines at 1.5 ms^{-1} 124

6.19 Cyclical mounting forces loading for the 15° blade overlap angle turbine for one revolution at an inflow velocity of 1.5 ms^{-1} 124

7.1 Straight (a) and helical-bladed (b) vertical axis turbines, showing definitions of azimuth rotational angle θ, and blade overlap angle ϕ 129

7.2 DMS model showing an example of the streamtube method for calculation of upstream and downstream flow velocity values V_1 and V_2 132

7.3 Simulation domain boundary nomenclature and sizing used for straight and helical CFD models. Dimensions in relation to turbine diameter, D, and height, S, as shared by the two turbine designs 133

7.4 ANSYS structural model of helical turbine showing loading conditions including imported pressures, rotational velocity, gravity, and the fixed supports . . 137

7.5 Straight-bladed turbine normal force coefficient simulations for one revolution using the DMS and CFD models at λ=1.5, 2.75, and 3.5 139

7.6 Signed maximum von Mises blade stress and total deflection comparisons for the DMS-Beam, CFD-Beam, and CFD-FEA straight-bladed turbine models at λ=1.5. Positive deflection is outwards away from the shaft 141

7.7 Change in location of maximum blade stress and deflection between 0° and 135° found by CFD-FEA straight-bladed turbine model at λ=1.5. The location of the maximum stress and deflection is shown by the red label 141

7.8 Signed von Mises blade stress and total deflection comparisons for the DMS-Beam, CFD-Beam, and CFD-FEA straight-bladed turbine models at λ=2.75. Positive deflection is outwards away from the shaft 142

7.9 Signed von Mises blade stress and deflection comparisons for the DMS-Beam, CFD-Beam, and CFD-FEA straight-bladed turbine models at λ=3.5. Positive deflection is outwards away from the shaft 143

7.10 Turbine von Mises stress magnitudes in Pa for one turbine rotation at λ=2.75. Deflection scale increased by 150 to highlight structural deformation 144

7.11 Stress concentration in Pa at bottom blade-strut fillet showing the location of maximum von Mises Stress of 90.51 MPa at the azimuth angle of 0° at λ=2.75146

7.12 Maximum von Mises Stress at the bottom blade-strut fillet over one revolution determined using the straight-bladed CFD-FEA turbine model at λ=1.5, 2.75, and 3.5 146

7.13 Yield safety factor for the straight-bladed CFD-FEA simulation results for one revolution at λ=1.5, 2.75, and 3.5 147

7.14 Normal force coefficient simulations for one revolution for the helical CFD model at λ=1.5, 2.75, and 3.5 148

7.15 Helical turbine signed von Mises blade stress and deflection comparisons found using CFD-FEA models at λ=1.5, 2.75, and 3.5. Positive deflection is outwards away from the shaft 149

7.16 Maximum helical-bladed turbine von Mises stress levels comparing λ=1.5, 2.75, and 3.5 149

7.17 Comparisons of the maximum von Mises Stress magnitudes determined using the CFD-FEA models for the straight and helical turbine models at λ=1.5, 2.75, and 3.5 150

LIST OF TABLES

2.1 Shared Geometry of Turbines A and B (Rawlings 2008) 20

2.2 Domain Boundary Conditions for all CFD Models 26

2.3 Domain Size Independence Study for Turbine A for Half Domain 3D CFD Model Shown in Figure 6 at an Inflow Velocity of 1.5 ms^{-1} and λ=2.75 . . . 30

2.4 Simulation Time and Computational Requirements for One Turbine Revolution. Turbine A at λ=2.75 at an Inflow Velocity of 1.5 ms^{-1} 35

3.1 Common Geometrical Features of the Three Turbine Configurations (Rawlings 2008) 43

3.2 Domain Boundary Conditions for CFD Models 45

3.3 Domain Size Independence Study for Turbine A at 1.5 ms^{-1} and λ=2.75 . . . 50

3.4 Comparison of C_p for Symmetrical and Full Domains at an Inflow velocity of 1.5 ms^{-1} and λ=2.75 51

3.5 Main CFD Simulation Settings 52

4.1 Turbine Geometry for CFD and EFD Models (Webster 1978) 67

4.2 Determination of Gormont Coefficients M_1, M_2, and γ_{mx} 72

4.3 Domain Boundary Conditions for the CFD model (Strickland et al. 1979, Webster 1978) 75

5.1 Shared Geometry of Turbines A and B 85

5.2 Domain Boundary Conditions for all CFD Models 87

5.3 Predictions of the Magnitude and λ Location of Maximum C_p for Turbines A and B at an Inflow Velocity of 1.5ms^{-1}. Percentage Error Compared to Maximum EFD C_p 98

5.4 Simulation Time and Computational Requirements for One Turbine Revolution. Turbine A at λ=2.75 at an inflow velocity of 1.5 ms^{-1} 100

6.1 Turbine Design Parameters 106

6.2 Turbine Geometrical Parameters 107

6.3 Validation Turbine Geometrical Design Parameters (Bachant 2011, Rawlings 2008) 108

6.4 Boundary Conditions for all Turbines 111

6.5 Spatial and Temporal Independence Results 112

7.1 Shared Geometry of the Straight and Helical Turbines 131

7.2 Boundary Conditions for the Straight and Helical Turbines 134

7.3 Material Properties used for Straight-bladed and Helical Turbine Structural Analysis 137

7.4 Computational Requirements for One Revolution of the Straight-Bladed Turbine at λ=2.75 151

NOMENCLATURE

Greek Symbols

Symbol	Description	Units
α	Angle of Attack	rad
α_b	Effective Angle of Attack	rad
α_i	Induced Angle of Attack	rad
α_0	Zero-lift Angle of Attack	rad
α_{ref}	Reference Angle of Attack	rad
α_{ss}	Static Stall Angle of Attack	rad
$\dot{\alpha}$	Rate of Change of Angle of Attack	rads^{-1}
ϵ	Blade Camber	%
λ	Tip Speed Ratio	-
ν	Kinematic Viscosity	$\text{m}^2 s^{-1}$
ω	Rotational Rate	rads^{-1}
ϕ	Blade Overlap Angle	Degrees
ρ	Water density	kgm^{-3}
σ	Stress	Pa
θ	Azimuth Angle	rad

Roman Symbols

Symbol	Description	Units
AR	Blade Aspect Ratio	-
c	Blade Chord	m
c_a	Strut Chord	m
C_D	Drag Coefficient	-
C_{D_0}	Drag Coefficient at zero α	-
C_D^{Dyn}	Dynamic Drag Coefficient	-
C_{D_f}	Finite Span Drag Coefficient	-
C_{D_∞}	Freestream Drag Coefficient	-
C_{D_i}	Induced Drag Coefficient	-
C_{D_l}	Finite Span Lift Coefficient	-
$C_{D_{Strut}}$	Strut Drag Coefficient	-
C_{FX}	Inline Force Coefficient	-
C_{FY}	Lateral Force Coefficient	-
C_{FMAX}	Maximum Force Coefficient	-
C_{FZ}	Vertical Force Coefficient	-
C_L	Lift Coefficient	-
C_L^{Dyn}	Dynamic Lift Coefficient	-
C_{L_∞}	Freestream Lift Coefficient	-
C_m	Moment Coefficient	-
$C_{m_{Max}}$	Maximum Moment Coefficient	-
$C_{m_{Min}}$	Minimum Moment Coefficient	-
C_N	Normal Force Coefficient	-
C_p	Power Coefficient	-

C_{P_1}	Upstream Power Coefficient	-
C_{P_2}	Downstream Power Coefficient	-
C_{up_θ}	Upstream Torque at θ	Nm
$\overline{C_{Q_1}}$	Upstream Average Torque Coefficient	-
C_T	Tangential Force Coefficient	-
$\overline{C_{T_{up}}}$	Upstream Torque	Nm
d	Turbine diameter	m
E	Modulus of Elasticity	Pa
F_c	Centrifugal Force	N
F'	Downstream Tip Loss Factor	-
F	Upstream Tip Loss Factor	-
F_{up}	Upstream Momentum Factor	-
H	Turbine Height	m
I	Area Moment of Inertia	m^4
K_1	Moment of Inertia Proportionality Coefficient	-
L_e	Effective Blade Length	m
m	Blade Mass	kg
M_b	Blade Bending Moment	Nm
N	Number of Turbine Blades	-
r	Radius	m
R_e	Blade Reynolds Number	-
S	Turbine frontal area	m^2
$\overline{T_a}$	Average Resistive Torque	Nm
T	Turbine torque	Nm

t	Blade Thickness	-
TRF	Torque Ripple Factor	-
u	Interference Factor	-
u_{new}	Iteration Interference Factor	-
u'	Second Interference Factor	-
V	Inflow Velocity	ms^{-1}
V'	First Induced Velocity	ms^{-1}
V''	Second Induced Velocity	ms^{-1}
V_1	Upstream Velocity	ms^{-1}
V_2	Downstream Velocity	ms^{-1}
V_e	Equilibrium Velocity	ms^{-1}
V_{∞_i}	Freestream Velocity	ms^{-1}
W	Local Relative Velocity	ms^{-1}
y	Blade thickness / 2	m
$y+$	Dimensionless Distance of 1st Cell Height from Wall	-

ABBREVIATIONS

2D	Two-Dimensional
3D	Three-Dimensional
AMC	Australian Maritime College
BSL-RSM	Baseline-Reynolds Stress Model
DMS	Double Multiple Streamtube
CFD	Computational Fluid Dynamics
CWC	Circulating Water Channel
DNS	Direct Numerical Simulation
EFD	Experimental Fluid Dynamics
FEA	Finite Element Analysis
FSI	Fluid Structure Interaction
LES	Large Eddy Simulation
SST	Shear Stress Transport
URANS	Unsteady Reynolds-Averaged Navier Stokes

Chapter 1

Thesis Introduction

1.1 Introduction

Since the 1850s fossil fuels have dominated energy supply, however the desire to utilise alternative energy sources has led to a growing interest in harnessing the energy held within the oceans. This energy source is estimated to exceed 7,400 EJ/yr, easily surpassing human requirements (Arvizu et al. 2011). Currently there are over 200 differing devices proposed to harness ocean energy, with the development of many of these devices at an early stage of technical maturity (Osman et al. 2011). These devices capture and transform the energy from ocean waves, tidal and non-tidal current flows, and ocean thermal energy sources into useable electrical energy. Horizontal and vertical axis turbines are two devices proposed to capture the kinetic energy held within tidal and non-tidal current flows. Of the two, fixed pitch cross flow turbines such as vertical axis turbines, as shown in Figure 1.1, might be better suited for transforming the oceans tidal and current energy as they offer two inherent advantages over their horizontal counterparts. Vertical axis turbines are insensitive to flow direction and hence require no yawing mechanisms. Additionally, the drivetrain and electrical generators can be installed above the water's surface, easing installation and servicing (Dai & Lam 2009, Kirke 2011, Sutherland et al. 2012). However, deployment is severely limited as structural failures of similar onshore turbines in the 1970's and 1980's, caused by a lack of understanding of their unique structural properties, has restricted research and hence commercial development (Sutherland et al. 2012). Significant barriers to widespread usage exist, as little is known of their complex hydrodynamic and structural properties, making the design of these devices challenging.

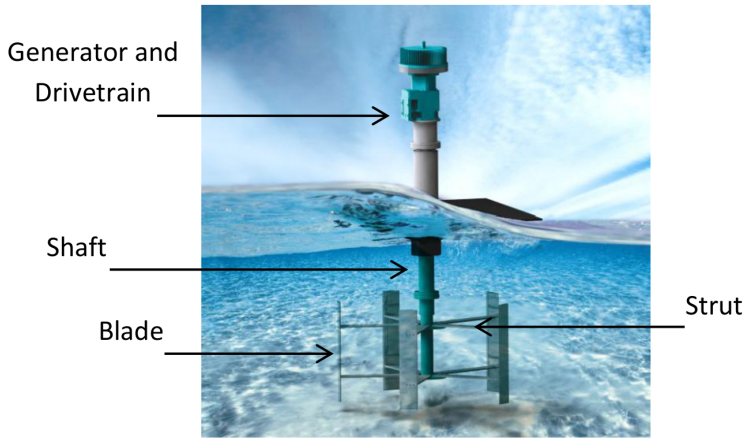

Figure 1.1: Vertical axis turbine used for tidal and current power generation showing definition of blades, struts and shaft, along with location of generator and drivetrain above the waters surface (*New Energy Corporation* 2014)

The installation and deployment of marine tidal and current flow turbines has proven difficult; with most commercial scale turbines deployed experiencing structural failures. Examples of such failures include:

- OpenHydro - all 12 blades of a 1MW tidal turbine destroyed in less than 20 days after deployment in the Bay of Fundy in 2009 (*OpenHydro* 2015);
- Atlantis Resources - blade failure of the AK1000 turbine during initial turbine operation at the EMEC test facility in Orkney(*Update on AK1000 blade replacement* 2015);
- Verdant Power - fixed blade failure at the blade roots of the three-bladed 35kW turbines within one day of deployment in New York (*Marine Renewable Energy Technologies* 2008); and
- SeaGen - blade failure at the blade roots of the SeaGen 600kW turbine as a result of overloading and fatigue cracking of the blades (Fraenkel 2010).

The reasons for these failures are often kept in confidence due to the competitive nature of the marine energy industry. However, these failures indicate that more research into blade design and loading characterisation is required to ensure the longevity of marine turbines. Detailed investigation of these characteristics will enable the improved design of turbines that will be robust enough to withstand ocean environments and become commercially successful.

1.1.1 Problem Definition

Vertical axis cross flow turbines generate power by transforming the hydrodynamic forces generated on the rotating turbine blades into normal and tangential forces, with the tangential forces generating torque and hence power that can be harnessed. However, as the turbine rotates the relative angle between the inflow and the rotating blades induces an angle of attack on the blades that varies with azimuth, resulting in significant variations of the normal force generated over each revolution. Research has found that optimal power is generated by slender blade sections with low thickness to chord ratio that have high lift/drag ratios (Paraschivoiu 2002). However, the use of slender blades carries significant structural penalties, as variations in normal forces can cause large bending moments and hence high stresses on the blade sections. Unlike horizontal axis designs, structural loading may further be compromised by the design and geometrical layout of the support struts shown in Figure

1.1. These radial arms support the blades loads generated, and use sections to minimise hydrdynamic drag. The cyclic nature of the normal and tangential forces also results in cyclical loading patterns, which can lead to high-cycle fatigue failure if not adequately accounted for as they are subject to a very high number of stress reversals over their intended operational life (Paraschivoiu 2002, Scheurich et al. 2011). If commercial scale vertical axis turbine deployments are to be successful, detailed understanding of hydrodynamic and structural loading characteristics is required, which will in turn allow for fatigue life-cycle determination.

Two vertical axis turbine geometries are prevalent, straight and helical-bladed, as shown in Figure 1.2. Helical turbines differ from straight-bladed turbines as the blades prescribe a helix around the rotational axis. However, considerable uncertainty exists over whether helical turbines generate more power than straight-bladed turbines, with Experimental Fluid Dynamics (EFD) finding conflicting results (Bachant 2011, Gorlov 1998, 2002, Niblick 2012). In addition, although previous EFD work has investigated power output for individual straight-bladed or helical turbines (Niblick 2012, Rawlings 2008), comparative studies using EFD are rare due to the complexity and expense of manufacturing and testing multiple physical models. If performed, this research is rarely extended to evaluate structural loading characteristics, due to the difficulties associated with measuring the stresses underwater on rotating turbine structures. Although methods for the investigation of both hydrodynamic and structural characteristics using EFD exist, concentration on the maximisation of power output necessary for commercial success has led to research focusing on hydrodynamic factors, such as blade section and turbine geometrical design, rather than structural considerations. As an alternative to EFD, recent advances in numerical simulation techniques appear promising, and offer new ways to investigate these hydrodynamic and structural characteristics.

Simulation of vertical axis turbine hydrodynamics can be performed using numerical modelling techniques. However, the modelling of vertical axis turbines is notoriously difficult due to the existence of complex hydrodynamic flow properties including simultaneous separated and attached flow fields, large degrees of dynamic stall, and significant blade-vortex interaction effects (Klimas 1982, Scheurich et al. 2011). Recent advances in high performance computing now allows for the investigation of complex hydrodynamic flow and pressure fields using numerical methods such as Computational Fluid Dynamics (CFD). The increase in computational power enabled by cluster computing also enables the extension of simulation models past Two-Dimensional (2D) investigations to transient Three-Dimensional (3D)

Figure 1.2: Examples of (a) straight (*T-Vision* 2015) and (b) helical-bladed (*Vertical Axis Wind Turbines vs Horizontal Axis Wind Turbines* 2015) vertical axis turbine configurations

models that include all turbine geometrical features. The development of CFD models using Unsteady Reynolds Average Navier-Stokes (URANS)-based simulations appears promising, with the ability to capture key performance coefficients such as power output along with rendering of the flow field enabling the visualisation of vortex structures (Castelli et al. 2010). However, the application of URANS-based model is challenging due to difficulties in the selection of turbulence model, mesh independence, and mesh quality factors. This study concentrated on these URANS-based simulations, with extensive verification and validation performed against published EFD to ensure the accuracy of the results obtained.

Alongside URANS-based simulations, computational methods such as Large Eddy Simulation (LES) and Direct Numerical Simulation (DNS) techniques can also be used to model turbine hydrodynamics; however they are extremely computationally demanding when compared to URANS methods (ANSYS 2010*a*). Models to simulate turbine power output using LES have been developed, however they are limited to 2D or 2.5D approaches as a result of the excessive mesh sizing required to capture the turbine boundary layer flow (Iida et al. 2007, Li et al. 2013). DNS simulations are even harder, being prohibitively computationally expensive even for 2D models with unrealistically low flow Reynolds numbers (Chen 2011). The drawbacks of the 2D approaches include the inability to capture any strut or blade tip effects, resulting in poor resolution of the complex 3D flow fields exhibited by vertical axis turbines, and thus 2D approaches were not used in this present study. Given the high computational demand of the LES and DNS methods, this thesis concentrated on URANS-based simulations.

Simpler modelling techniques such as Double Multiple Streamtube (DMS) models can be used to model and predict turbine performance, using methods based on momentum theory (Paraschivoiu 2002, Strickland et al. 1979). Through the addition of correction factors these models can simulate complex hydrodynamic effects such as dynamic stall, allowing for computationally efficient simulation of most turbine parameters (Dai & Lam 2009, Masson et al. 1998, Lain & Osorio 2010, Paraschivoiu 2002). In this work, DMS simulations are performed, with results compared to URANS-based simulations and published EFD to evaluate the accuracy of the DMS models developed.

Alongside the hydrodynamic models, turbine structural characteristics can be evaluated using beam theory or Finite Element Analysis (FEA) methods (Hameed & Afaq 2013, Li et al. 2014, Paraschivoiu et al. 2012, Tsai & Chen 2014). These methods, although not commonly performed on vertical axis turbines, are much computationally simpler that hydrodynamic modelling, with well-defined analysis methods. However, the accuracy of the structural models directly reflects the accuracy of the underlying hydrodynamic models, presenting a challenging simulation task.

Other methods exist which have varying degrees of computational efficiency. Free vortex models, which track eddy shedding downstream using continuous vortex lines or vortex points, can determine power output and blade forces, as well as the structure of the turbine wake (Islam et al. 2008, Strickland et al. 1979). The source of circulation used by these models is EFD lift and drag data or by analytical methods such as conformal mapping (Strickland et al. 1979). As the turbine wake structure was not investigated as part of this present work, only DMS models were used due to their computational efficiency (Paraschivoiu 2002).

1.1.2 Objectives

The key driver of this research was to investigate and compare the hydrodynamic and structural loading characteristics of straight and helical-bladed vertical axis turbines using numerical simulation techniques. This work specifically seeks to answer the following question:

Are straight or helical-bladed vertical axis turbines more suited for ocean tidal and current power generation when evaluated using power output, mounting force, and structural loading criteria?

To answer the research question, initial efforts concentrated on establishing the accuracy of numerical models in simulating straight-bladed vertical axis turbine performance for differing geometrical configurations. These studies were then extended to evaluations of helical turbine performance parameters, with comparisons made to the straight-bladed turbine results. Following on from this, numerical evaluation of the structural loading of the straight and helical-bladed turbines was performed, enabling comparison between the two designs. At all stages of this work verification and validation studies were performed against EFD results published in literature to establish the accuracy of the models developed, as well as the influence of modelling parameters on this accuracy. This approach was developed to gain clear insight not only into the hydrodynamic and structural characteristics of vertical axis turbines, but also into the numerical simulation techniques themselves. This contribution opens up new opportunities for turbine improvement, enabling enhanced designs based on both hydrodynamic and structural considerations.

1.2 Geometric Models

Validation of the numerical models was considered a key objective of this thesis to ensure the accuracy of the simulation models developed, with most validation performed against published data available in the literature. These models, with differing geometrical layouts, enabled the evaluation of the hydrodynamic models capability to capture geometrical influences on performance parameters including power output. The results from six EFD tests were used for validation purposes for turbine geometries that included:

- two EFD straight-bladed turbines from literature, as shown in Figures 1.3c and 1.3d (Rawlings 2008) used to evaluate the influence of strut location, strut section, and blade-strut joints on CFD models power output predictions;
- one helical EFD turbine from literature shown in Figure 1.3b (Bachant 2011, Bachant & Wosnik 2015) used to examine the capability of CFD models to simulate helical turbine hydrodynamic performance parameters;
- two EFD turbines from literature (Strickland et al. 1979, Webster 1978) shown in Figures 1.3(a) and 1.3(f) that incorporated strain gauges to examine the validity of blade force simulation results for one and three-bladed turbines; and
- one EFD turbine that was used during testing conducted at the Australian Maritime College (AMC) as shown in Figure 1.3e used for initial modelling investigations.

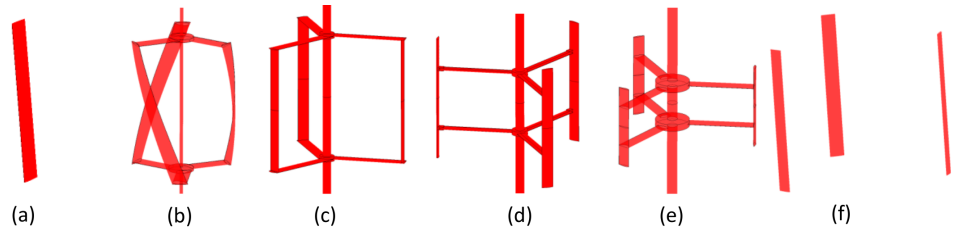

Figure 1.3: Validation CFD models showing (a) one-bladed (Strickland et al. 1979, Webster 1978), (b) Lucid helical (Bachant 2011, Bachant & Wosnik 2015), (c) and (d) Rawlings three-bladed (Rawlings 2008), (e) AMC three-bladed, and (f) three-bladed (Strickland et al. 1979, Webster 1978) turbines (struts not modelled - see Chapters 4 and 5)

The key numerical investigations were performed on a series of turbine models of the same height, span, blade chord, and strut design. The baseline 0° (straight-bladed) turbine design was geometrically similar to a previously tested EFD turbine from literature (Rawlings 2008), to permit validation of the numerical modelling techniques used. The turbines were designed with ascending blade overlap angles and thus helicity (ϕ) as shown in Figure 1.4 of 0°(straight-bladed), 15°, 30°, 60° and 120°, allowing the direct characterisation of blade overlap with power output, torque fluctuation levels, and mounting forces. Additionally, the influence of hydrodynamic profile alignment with the blade leading edge was evaluated by inclining the profile from the horizontal plane from -15° to +45° as shown in Figure 1.5 for the 15° blade overlap helical turbine shown in Figure 1.4 to determine if section alignment influenced power output. Structural analysis was performed on the 0° and 15° turbines with 0° blade section inclination, as shown in Figure 1.5, as results indicated that as helicity increased beyond 15° power output reduced signifigantly, reducing the turbine's utility to harness ocean energy.

1.3 Methodology

The hydrodynamic and structural characteristics of straight and helical-bladed vertical axis turbines were investigated using the following three key steps:

- a literature review included in each chapter that examined previous hydrodynamic and structural characteristics research, including any relevant numerical modelling techniques;
- development, verification, and validation of hydrodynamic DMS and CFD numerical simulation models to obtain power output, torque fluctuations, mounting forces, and strut location influences; and

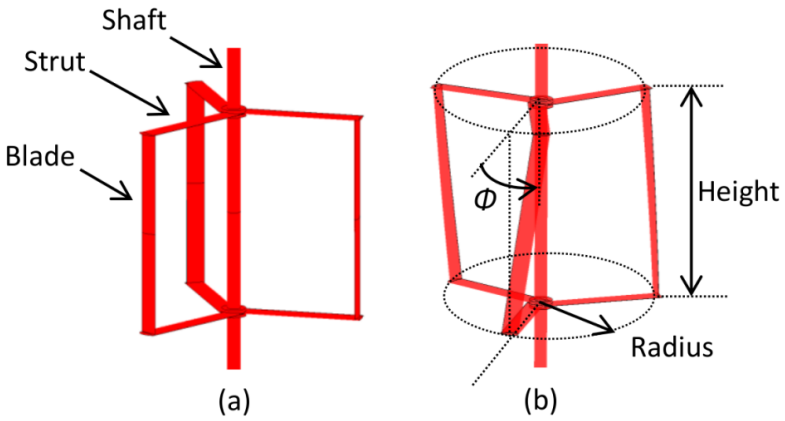

Figure 1.4: Straight (a) and helical-bladed turbine showing geometrical notations and definition of blade overlap angle ϕ

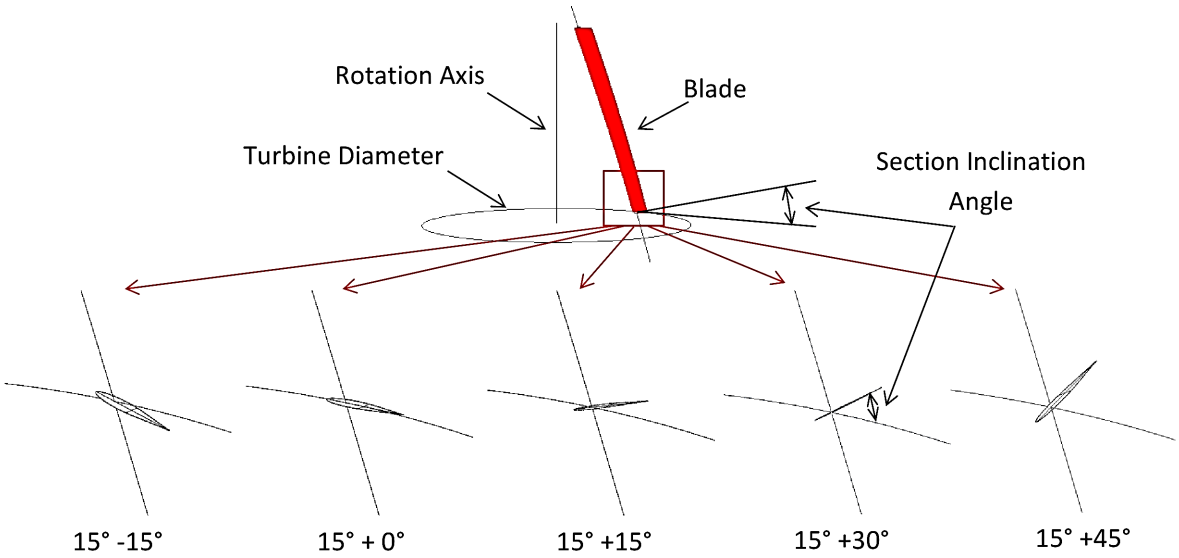

Figure 1.5: Definition of section inclination angle of the blade sections to the horizontal rotation plane for the 15° helical turbine

- coupling of developed hydrodynamic models to structural FEA and beam theory models to determine the structural characteristics of straight and helical-bladed vertical axis turbines, including the relative merits of the different geometrical configurations.

1.4 Key Considerations

1.4.1 Hydrodynamic Considerations

Key to this work is the determination of the hydrodynamic forces and pressures generated by vertical axis turbines as they rotate. These are evaluated at a series of rotational rates corresponding from start-up to over speed conditions, expressed as the tip speed ratio, λ, defined as the ratio of the tip velocity to the inflow velocity. The key performance components investigated in this work were the:

- turbine power output, a measure of turbine efficiency in converting kinetic energy, expressed as the non-dimensionalised power coefficient C_p;
- torque ripple factor, TRF, determined using non dimensionalised coefficients of the moment generated by the turbine, allowing the evaluation of torque fluctuations generated by the rotating blade;
- normal and tangential blade forces, geometrically defined relative to the blade chord, and non-dimensionalised by dynamic pressure and blade chord;
- inline, lateral, and vertical mounting forces as shown in Figure 1.6; and
- hydrodynamic flow visualisation, which was utilised to increase understanding of flow behaviour, giving insight into the nature of flow properties such as vortex shedding and flow diffusion.

1.4.2 Structural Loading Considerations

To establish the structural loading characteristics of vertical axis turbines, evaluation of structural loading was performed using beam theory and FEA models. These models examined loading by determining the:

- stress and deflection of the turbine blades and struts, performed using beam theory and FEA techniques, with the stress calculations signed according to the blade deflecting

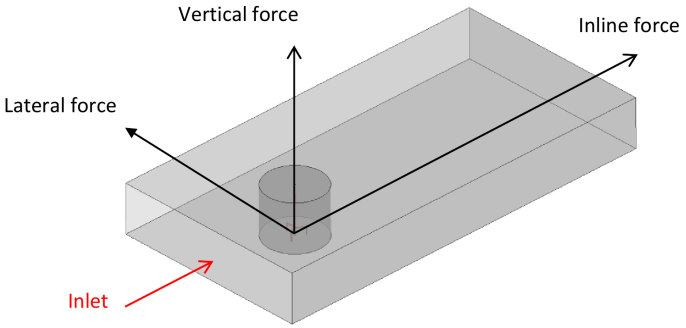

Figure 1.6: Definitions of lateral, inline, and vertical forces

inwards towards the turbine shaft (-) or outwards (+) to enable the evaluation of any cyclical loading patterns; and

- yield stress safety factors, to gain insight into loading margins against material yield strength properties.

1.4.3 Geometric Considerations

The relative performance of straight and helical-bladed vertical axis turbines was examined using turbines of the same frontal area and blade chord, ensuring that no Reynolds or Froude number scaling was required. To ensure widespread applicability, the numerical models developed incorporated corrections for Reynolds number effects, either inherently in the case of the URANS CFD models, or by lookup lift and drag tables for the DMS model. This ensures that the models developed as part of this work can be used for simulations of turbines with differing geometrical dimensions or differing inflow and rotational rates to those studied here. Although the influence of drive train or generator losses was not simulated the models developed could be utilised as input for drive train and generator analysis models, if required.

1.4.4 Assumptions and Limitations

This study sought to validate all numerical simulation models against EFD data to ensure the accuracy of the simulated results. The power output, mounting forces, and normal and tangential blade forces were validated against EFD from literature for both straight and helical-bladed turbines (Bachant 2011, Bachant & Wosnik 2015, Rawlings 2008, Strickland et al. 1979, Webster 1978). However, no EFD data was available to validate structural blade stress and deflection simulation results. To overcome this, two separate numerical methods,

one based on EFD lift and drag data tables, the other on solutions to the Navier-Stokes equations, were used to determine the force coefficient predictions. These were then coupled to two separate numerical methods of determining blade stress and deformation, using well established structural FEA and beam theory methods (ANSYS 2013, Council 2007). This work could however be compared to future EFD work using strain gauges to validate the relationships determined in this study.

The vertical axis turbines studied in this work operated in low Reynolds numbers regimes, as the EFD data from literature used for model validation was obtained at Reynolds numbers of less than 5×10^5 (Bachant 2011, Bachant & Wosnik 2015, Rawlings 2008, Strickland et al. 1979, Webster 1978). Although the numerical simulations were restricted, all simulation models developed accounted for the influence of Reynolds number on hydrodynamic lift and drag forces, and hence can be used for alternative flow velocities. The velocities examined also correspond to realistic tidal flow velocities for ocean turbine installations (Osman et al. 2011).

1.5 Novel aspects

This study provides a significant contribution through the application of numerical simulation methods to investigate and research rarely studied turbine characteristics. The novel aspects of this work include the following:

- Evaluation and comparison of the hydrodynamic and structural loading characteristics of both helical and straight-bladed turbines. Although previous work has investigated each design individually (Khalid et al. 2013, Hameed & Afaq 2013, Li et al. 2014, Paraschivoiu et al. 2012, Tsai & Chen 2014), this study is pioneering as it not only evaluates each turbine individually, but provides a comparative study of the two designs.
- The hydrodynamic and structural loading numerical models included the blade and strut geometry, allowing for the evaluation of strut and blade-strut joint loading. Previous work has concentrated solely on blade loading (Khalid et al. 2013, Hameed & Afaq 2013, Li et al. 2014, Tsai & Chen 2014).
- Three-dimensional CFD studies were performed, whereas previous studies were performed using 2D or 2.5D models that do not account for strut or blade tip losses (Dai

& Lam 2009, Li et al. 2013, Lain & Osorio 2010, Malipeddi & Chatterjee 2012, Navabi 2008, Beri et al. 2011, Gretton 2009).

- Structural loading simulations were performed over rotational rates ranging from starting, maximum power, to over speed conditions. Previous numerical simulations of structural loading work have concentrated on single rotational rates (Hameed & Afaq 2013, Li et al. 2014, Paraschivoiu et al. 2012, Tsai & Chen 2014).

- A comparison of the influence of blade helicity on power output, mounting forces, and torque ripple was performed using a series of ascending blade overlap angles. Numerical comparisons of the influence of helicity are rarely, if ever, published, with only limited EFD studies performed to date (Gorlov 1998, 2002, Niblick 2012, Shiono et al. 2002).

- Evaluations of the mounting forces generated by straight and helical-bladed turbines were performed. Although they have previously been obtained using EFD (Bachant 2011, Bachant & Wosnik 2015, Rawlings 2008), numerical studies are rare.

- Comparisons of the relative merits of the numerical methods used for hydrodynamic and structural turbine analysis, including the examination of the computational efficiency of each model. Previous studies have used only one numerical method, not allowing any comparison of the benefits and disadvantages of the numerical methods utilised (Hameed & Afaq 2013, Khalid et al. 2013, Li et al. 2014, Paraschivoiu et al. 2012, Tsai & Chen 2014).

1.6 Thesis Outline

This work was completed as a series of journal and conference papers and are collated and presented as chapters within this thesis as outlined below. The chapters follow the evolution of both numerical simulation models and turbine geometries, culminating in the development of structural analysis models for straight and helical-bladed turbines.

Chapter 1: The introductory chapter frames the research questions, provides a broad outline of the methodology and geometrical models used, and the objectives of the study. Identification of the novel aspects of the work are discussed, along with consideration of any limitations.

Chapter 2: This paper introduces the CFD modelling of two straight-bladed vertical axis turbines using a commercial URANS solver. Simulations of two geometrically differing vertical axis turbines were performed to obtain turbine power output using 2D and 3D URANS models using the k-ω Shear Stress Transport (k-ω SST) and Baseline-Reynolds Stress Models (BSL-RSM) turbulence models. All models were benchmarked against published EFD data, with consideration of 2D and 3D models, turbulence model selection, laminar-to-turbulent transition effects, mesh sizing, domain sizing, temporal step, and boundary layer independence. The computational costs of the models were evaluated and weighed against solution accuracy.

Chapter 3: The second paper supports the finding in Chapter 2 with a more comprehensive analysis of CFD modelling techniques for three straight-bladed vertical axis turbines. These turbine models differed in strut cross-section and their location along the blade, to examine the predictive capacity of commercial transient URANS models in determining power output, torque fluctuation levels, and mounting forces. Comparisons of URANS predictions for the power output and mounting force against experimental results from literature allowed the validation of the numerical models developed. An investigation into the selection of grid independence factors, with appropriate mesh sizing and temporal treatments was completed to allow for accurate representation of the maximum power output. Initial assessment of strut geometrical influences were established, with their optimal location for the given design identified.

Chapter 4: Paper three introduces the DMS model to simulate turbine blade forces. The DMS model incorporates the Gormont dynamic stall model to account for variations in blade angle of attack due to turbine rotation. The developed DMS model, along with the k-ω SST CFD models outlined in Chapters 2 and 3, were used to simulate the blade normal and tangential force data from a series of EFD testing from literature on one and three-bladed turbines, with results compared to EFD to determine the respective accuracy of each of the numerical hydrodynamics models. The influence of blade number on turbine power output was also evaluated using DMS and k-ω SST CFD models to characterise the influence of wake effects.

Chapter 5: This conference paper examines two of the straight-bladed turbine models simulated in Chapters 2 and 3 using the DMS and k-ω SST CFD models developed in Chapters 2-4, with results compared to EFD data from literature. In contrast to Chapter 4, the mod-

els developed concentrate on power output instead of blade forces to determine the accuracy of the DMS and k-ω SST CFD models in simulating turbine power output. Examinations of the computational requirements of each numerical model were performed, alongside the determination of any limitations, enabling the development of numerical analysis guidelines for power output simulations of vertical axis turbines. The models analysed in this Chapter were used as input to characterise turbine blade loading in Chapter 7.

Chapter 6: The fourth paper concentrates on establishing any differences, and thus any advantages between helical and straight-bladed turbines using k-ω SST CFD numerical techniques. The numerical simulation of helical turbines was investigated, with verification and validation of the developed k-ω SST CFD models carried out against EFD results from literature. The influence of helicity on power output, torque ripple, and mounting forces was investigated, with flow visualisation of vortex shedding performed to interpret blade inclination effects. The extension of the k-ω SST CFD model to enable the modelling of helical turbines outlined in this chapter allowed for the future examination of structural loading characteristics for both straight and helical turbines performed in Chapter 7.

Chapter 7: Paper five couples the validated DMS and k-ω SST CFD hydrodynamic models developed in Chapters 2-6 to structural analysis models using both FEA and beam theory, enabling comparisons of the various combinations. Two turbine designs were examined, one straight-bladed and one helical turbine with a low degree of blade overlap. The models presented form a transient model of the structural loading as the turbine rotates, allowing detailed investigation of stress and deflection magnitudes at varying turbine rotational rates. The location of maximum stress is probed, along with its relationship with rotational angle. The suitability of each simulation technique is outlined, along with computational requirements and any limitations. Considerations of structural loading differences between the two turbine designs is presented, along with options to reduce structural loading if required. Finally, recommendations for the best turbine design for ocean deployment are outlined.

Chapter 8: Concludes this work by providing an overall summary of results, discussing key findings, and any consequences for future research. The geometrical design implications of the results are presented, along with recommendations for future research.

Appendices: Appendix A: outlines initial efforts to develop CFD and DMS models and validate results against EFD data obtained at AMC using numerical models with and without

struts or strut correction factors. Cost limitations of the EFD testing allowed for only one turbine to be tested, with research efforts turning to validation using published EFD data for multiple turbine geometries, as performed in Chapters 2-7. **Appendix B** further outlines initial efforts to simulate vertical axis turbine power output by developing CFD models and comparing results to EFD data obtained at the AMC.

Chapter 2

The Influence of Turbulence Model and Two and Three-Dimensional Domain Selection on the Simulated Performance Characteristics of Vertical Axis Turbines

This chapter has been submitted for publication in the Journal *Renewable Energy*, and at the time of writing is under review. The citation for the research article is:

Marsh P., Ranmuthugala, D., Penesis, I., & Thomas, G, The Influence of Turbulence Model and Two and Three-Dimensional Domain Selection on the Simulated Performance Characterisitcs of Verticla Axis Turbines, *Renewable Energy*. [Under review, 2015].

Abstract

Computational Fluid Dynamics (CFD) models were developed to simulate the power output of two geometrically differing vertical axis turbines. To evaluate the influence of numerical modeling techniques on these power output predictions simulations were performed using Two-Dimensional (2D) and Three-Dimensional (3D) models, as well as the Baseline-Reynolds Stress Models (BSL-RSM) model and the k-ω Shear Stress Transport (k-ω SST) in its fully turbulent and laminar-to-turbulent transition model formulation. The highest correlation with EFD power output from literature was found using the 3D k-ω SST Transition model, although it was extremely demanding computationally. The fully turbulent 3D k-ω SST model also offered accurate prediction of power output for most rotational rates. The 3D BSL-RSM model results poorly simulated power output and came at a high computational cost. Poor output predictions were also obtained using 2D k-ω SST models, as they were unable to account for 3D flow effects. Results indicated that it was necessary to fully resolve all boundary layers, with models using wall functions poorly resolving power outputs. The authors suggest that 3D fully turbulent k-ω SST models with fully resolved boundary layers are used to simulate turbine performance.

2.1 Introduction

The potential of using ocean energy to generate renewable energy has led to increased interest in vertical axis turbines, as they are a viable option to transform the oceans tidal and current kinetic energy into electricity (Arvizu et al. 2011). Vertical axis turbine designs as shown in Figure 2.1 exhibit two key advantages over competing ocean energy device designs: they are insensitive to inflow direction and all electrical components can be mounted above the water surface (Marsh et al. 2013). When combined, these factors enable simple and robust turbine designs for ocean installations. However, little is known of their complex hydrodynamic properties, as previous research and development has concentrated on horizontal axis designs as commonly utilised in the wind energy industry (Scheurich et al. 2011). If ocean turbines are to be successfully deployed at commercial scales, detailed understanding of their operational characteristics is essential. This can be obtained through numerical simulations such as Computational Fluid Dynamics (CFD) or by Experimental Fluid Dynamics (EFD).

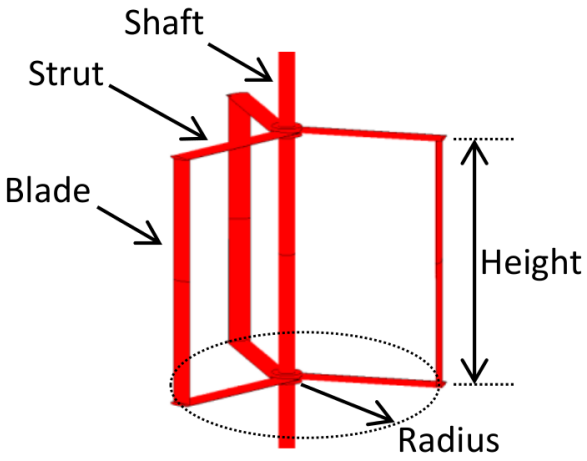

Figure 2.1: Vertical axis turbine showing definitions of key geometrical features

Vertical axis turbines are commonly studied using CFD models as they allow for turbine performance investigations without the expense of EFD. The majority of CFD simulations are performed using Two-Dimensional (2D) models due to their reduced computational requirements when compared to Three-Dimensional (3D) models. However, these 2D approaches often significantly over predict maximum power output (Castelli et al. 2010, Danao 2012, Malipeddi & Chatterjee 2012, Matre et al. 2013) due to the highly 3D nature of turbine hydrodynamic flow (Marsh et al. 2012). Numerical simulations are also commonly performed using fully turbulent models (Alidadi 2009, Castelli et al. 2010, Danao 2012, Malipeddi & Chatterjee 2012, Marsh et al. 2012, Matre et al. 2013), again due to their computational efficiency. However, the influence of laminar-to-turbulent flow transition on power output predictions is unknown, and may be significant as turbines can operate in low Reynolds number dominated flows (Marsh et al. 2013). For turbulence modeling the (k-ω Shear Stress Transport ((k-ω SST) model is prevalent (Castelli et al. 2010, Dai & Lam 2009, Gretton 2009, Nobile et al. 2011, Lain & Osorio 2010, Marsh et al. 2012, 2013, 2015a,b), due to its ability to model both free stream and wall bounded flows accurately. However, studies of the influence of alternative turbulence modeling schemes on the accuracy of power output predictions are limited. Combined, the influence of these modeling factors on power output predictions is unknown and was the key driver for this research.

Numerical simulations were performed on two vertical axis turbines using the ANSYS CFX v13 software package to evaluate the influence of turbulence model and 2D and 3D domain modeling techniques on the predictive capacity of Unsteady Reynolds Averaged Navier-Stokes (URANS) based simulation models (ANSYS 2010a). These turbine models were

geometrically identical to EFD from literature to allow for verification and validation of all power output simulations (Rawlings 2008). The 2D and 3D CFD models developed used the k-ω SST and Baseline-Reynolds Stress Models (BSL-RSM) turbulence models with differing wall modeling approaches to appraise any wall modeling influences on simulation accuracy. Additionally, flow transition modeling was performed using the k-ω SST Gamma-Theta Transition (k-ω SST Transition) model to establish the influence of transition modeling on power output simulation accuracy.

2.2 Numerical Simulation

Numerical 2D and 3D CFD simulations were performed using the ANSYS CFX v13. software package (ANSYS 2010*a*), which solves the transient URANS equations using an element-based finite volume approach. Simulations of two geometrically different turbines were performed to evaluate the ability of the various turbulence and 2D and 3D domain models to accurately simulate power output when compared to EFD from literature (Rawlings 2008).

2.2.1 Turbine Geometry

Two straight-bladed vertical axis turbines models were developed as shown in Figure 2.2, labeled Turbines A and B respectively. These turbine designs were geometrically equivalent to EFD models from literature to allow validation of the numerical simulation approaches (Rawlings 2008). These models shared the same blade section, span, and number of blades as detailed in Table 2.1. However, the turbines differed in strut section and location, as Turbine A had NACA0012 strut sections located at the blade ends, while Turbine B had shaped bar struts located at the blade quarter span, both shown in Figure 2.2.

Table 2.1: Shared Geometry of Turbines A and B (Rawlings 2008)

Geometry	Dimensions
Number of blades	3
Number of struts	2 per blade
Blade section	NACA 634021
Blade chord	0.065m
Diameter (d)	0.915m
Turbine span (s)	0.686m

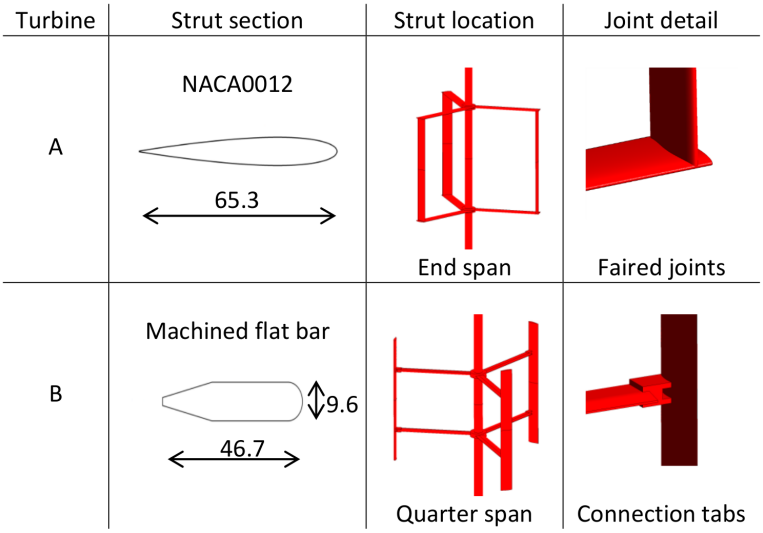

Figure 2.2: Turbine A and B strut section and location detail. Dimensions in mm (Rawlings 2008)

2.2.2 Key Performance Parameters

To evaluate turbine performance, the turbine power output is evaluated as the non-dimensionalised power coefficient C_p where,

$$C_p = \lambda \, C_m \tag{2.1}$$

where the tip speed ratio λ is defined as,

$$\lambda = r\omega/V \tag{2.2}$$

and ω is the turbine rotational rate, r is the turbine radius, V is the inflow velocity, and the turbine torque C_m is determined as,

$$C_m = T/(0.5\rho V^2 S r) \tag{2.3}$$

where ρ is the water density (set to 1000 $\frac{kg}{m^3}$ for all simulations), S is the turbine frontal area, and the torque T generated by the turbine was taken from the respective CFD or EFD results.

2.2.3 Turbulence and Boundary Layer Modeling

The influence of turbulence model selection on power output predictions was examined using three turbulence models; the k-ω SST, k-ω SST Transition and BSL-RSM models. Differing boundary layer modeling techniques were also introduced to evaluate the influence of boundary layer modeling techniques on simulation accuracy.

The influence of flow transition was modeled using the Gamma-Theta formulation of the k-ω SST transition model (ANSYS 2010a). The k-ω SST Transition model uses two additional transport equations when compared to the fully turbulent k-ω SST model to capture transitional effects: the intermittency equation, γ, and the transition onset momentum thickness Reynolds number, $Re - \theta$ (ANSYS 2010a). The k-ω SST Transition model does not model the physical fluid processes, but rather applies empirical correlations to the underlying k-ω SST model (ANSYS 2010a). For this study no modification of correlation coefficients was performed, as post priori modification of these coefficients would reduce the models utility for design investigations where performance data was unavailable. To ensure the accurate simulation of flow near all turbine surfaces, the boundary layers were fully resolved as recommended (ANSYS 2010a).

The k-ω SST turbulence model was also used in its fully turbulent formulation as it is commonly used to simulate turbine performance (Castelli et al. 2010, Dai & Lam 2009, Gretton 2009, Lain & Osorio 2010, Marsh et al. 2012, 2013, 2015a,b, Nobile et al. 2011) due to its ability to model both the boundary layer and the free stream regions. Research has shown that it can accurately predict flow separation and adverse pressure gradients as a result of the inclusion of transport effects into the formulation of the eddy-viscosity equations (ANSYS 2010a, Menter 1994). To evaluate the influence of boundary layer modeling two 3D k-ω SST meshes were developed. Flow modeling near the turbine surfaces was performed either by using prescribed wall functions based on log-wall laws or by fully resolving the boundary layer flow (ANSYS 2010a). This resulted in the two 3D k-ω SST meshes using differing inflation layer densities as shown in Figure 2.3 , which are referred to as the 3D k-ω SST Wall Function or 3D k-ω SST models respectively. Total boundary layer thickness was estimated as $0.37c/Re^{1/5}$ with the blade chord c used to determine Reynolds number, Re (Anderson Jr 1985). This estimated boundary layer thickness was doubled to ensure that the boundary layer was contained within the prescribed inflation layer region. Inflation layer mesh growth rates were limited to 1.2 as recommended (ANSYS 2010a). Boundary layer

mesh density independence was also evaluated by examining the influence on power output of the average height of the first cell from the turbine walls, known as the non-dimensional variable $y+$ (ANSYS 2010a).

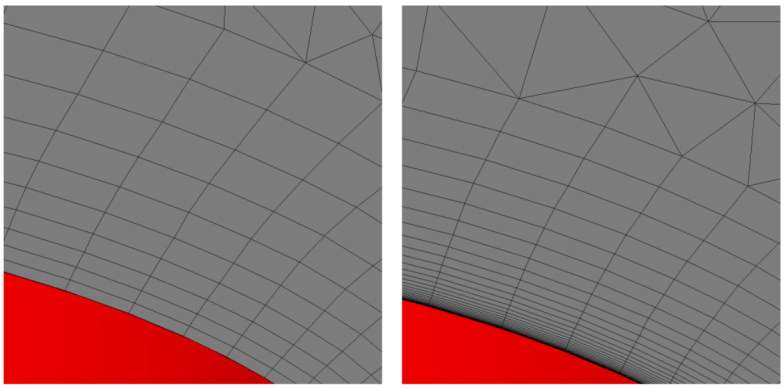

Figure 2.3: Blade surface inflation layer mesh density for: (a) k-ω SST Wall Function and (b) fully resolved 3D k-ω SST models showing differences in mesh density with 10 and 30 layers respectively

Along with the two k-ω SST-based turbulence models, power output simulations were performed using the BSM-RSM model, which closes the URANS equations by solving six transport equations for the Reynolds stresses, as well as an additional equation for dissipation rate (ANSYS 2010a). Due to these additional transport equations BSL-RSM is suggested to be better at modeling complex flows with high levels of streamline curvature, fluid rotation, and rotating reference frames (ANSYS 2010a), as occurs during vertical axis turbine operations. Again to ensure the accurate simulation of flow near all turbine surfaces, the boundary layers were fully resolved.

The influence of numerical discretization scheme on C_p prediction accuracy was investigated by performing simulations using low and high order numerical schemes, with results compared to EFD from literature for Turbine A (Rawlings 2008). The high order scheme used a bounded second order upwind biased advection and an unbounded second order backwards Euler transient scheme, whereas the lower order scheme used a first order upwind advection and first order backwards Euler transient scheme (ANSYS 2010a).

For all simulations the fluid was modeled as incompressible as all flow velocities were significantly less than Mach 0.3. An inlet turbulence setting of 5% was applied as no measurements

of turbulence intensity were provided from the EFD testing from literature (Rawlings 2008). Convergence was deemed achieved when solution residuals reduced to below 10^{-4} and reduced by more than three orders of magnitude. Additionally convergence was confirmed by ensuring that the final C_p determined was within 5% of the previous rotations results, required due to the periodic nature of C_p. An example of C_p convergence for Turbine A is shown in Figure 2.4, where C_p values converged after approximately 3600 time steps, corresponding to 9 rotations. To reduce overall simulation times all simulations were started using previous simulation results if available, reducing the initialization process and thus the overall computational requirements.

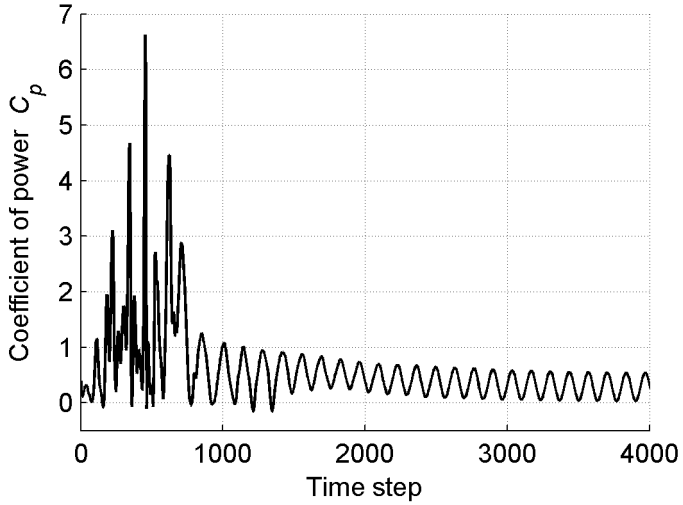

Figure 2.4: Example of C_p convergence for Turbine A at λ=2.75 at an inflow velocity of 1.5 ms^{-1}

2.2.4 Computational Fluid Dynamics (CFD) Models

To determine the influence of domain selection on simulation accuracy, both 2D and 3D domains were generated. All turbine models were meshed using ANSYS CFX 13.0 (ANSYS 2010*a*) using unstructured tetrahedral elements, an example of which is shown in Figure 2.5 for the 3D k-ω SST model. The 3D CFD models included all 3D geometrical features including all blades, struts, hubs, and shaft, with the k-ω SST and BSL-RSM models using the same mesh. The 2D models only included the blades and shaft due to the geometrical layout of vertical axis turbines. Turbine rotation was simulated by enclosing the turbine in an inner domain as shown in Figure 2.6. This domain was rotated using the CFX transient rotor-stator model (ANSYS 2010*a*), with a General Grid Interface (GGI) used to interpolate

flow values across the interface due to non-conformal mesh. To minimise any errors in the intersection algorithm, the GGI was placed at 1.5 times the turbine diameter measured from the rotational axis. Mesh density was also increased on this interface as shown in Figure 2.5 to further minimise any errors across the GGI interface. For all simulations the inner domain was rotated at the desired rotational rate corresponding to CFD or EFD testing rates. Mesh density was varied according to expected flow curvature rates, resulting in increased density in regions near the blades, struts, hubs, shaft, and wake. Mesh density was reduced away from the turbine surfaces such as near the computational domain boundaries to minimise computational effort.

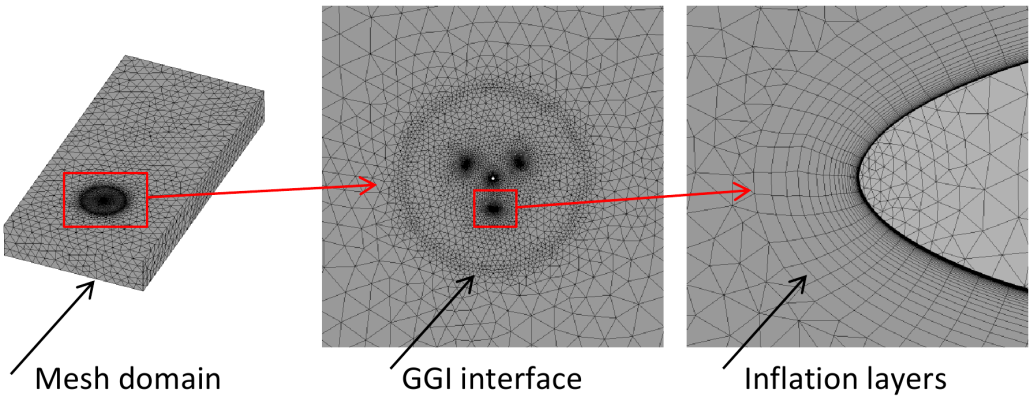

Figure 2.5: Mesh domain for 3D model showing overall mesh domain, GGI interface, and inflation layer detail on the blade surface for the 3D k-ω SST Turbine A model

The 3D computational domains were generated to isolate the turbine from any boundary effects; with all boundary conditions outlined in Figure 2.6 and Table 2.2, as determined by the systematic domain size independence studies. Both Turbines A and B were assumed to operate at sufficient depths to ignore free surface effects, allowing the use of symmetry to reduce domain size (Marsh et al. 2012, 2013, 2015*a*,*b*). Full and half domains were generated, with the half domain split along the horizontal mid plane. To ensure that this use of a half domain did not influence the accuracy of the power output predictions, simulations using a full 3D domain, also shown in Figure 2.6, were performed for comparison.

The 2D CFD model is shown in Figure 2.7, with the boundary details outlined in Table 2.2. In comparison to the 3D CFD model, shown in Figure 2.6, the 2D CFD model consisted only of the blade sections and shaft. This resulted in the same model being used for Turbines A and B, as the models differed only in strut location and section. The computation domain

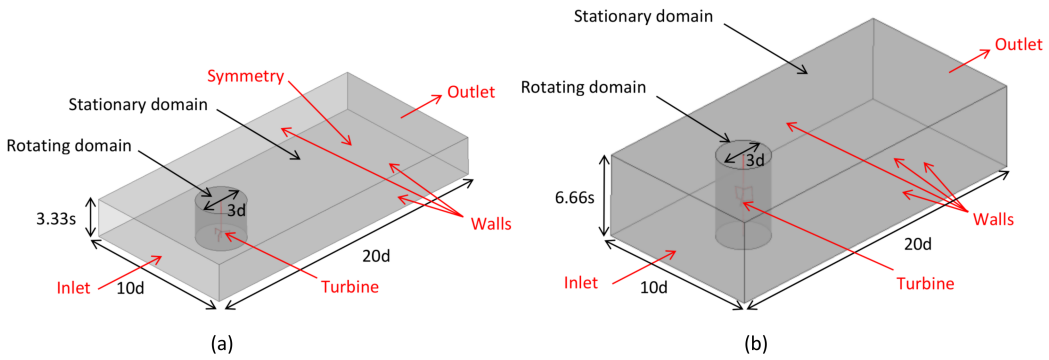

Figure 2.6: Domain nomenclature and sizing for the (a) half, and (b) full 3D CFD models. Dimensions in turbine diameter d and span s

Table 2.2: Domain Boundary Conditions for all CFD Models

Wall	Boundary condition
Inlet	Uniform flow perpendicular to inlet wall: 1.5 ms^{-1}
Outlet	Relative Pressure: 0 Pa
Walls	Free slip walls
Turbine	No slip walls
Symmetry	Symmetry walls

was constructed by cutting a 0.01m slice from the 3D model shown in Figure 2.6, as ANSYS CFX cannot natively model in 2D, with the domain thickness represented by a thin layer of tetrahedral cells.

2.2.5 Mesh Independence Studies

Systematic independence studies were performed to ensure domain size, domain boundary, mesh density, boundary layer modeling, and time step independence for both turbine designs. Independence was evaluated by investigating the impact on C_p of increases in these factors until variations between each successive refinement reduced to less than 5% using the method outlined in Tu (2013). Examples of the independence studies are only presented for Turbine A here for brevity, but were performed for both turbines with similar results found. The influence of numerical discretisation scheme on C_p was also evaluated.

Figure 2.8 illustrates mesh element count independence for Turbine A, which was achieved at 0.16, 9.1, 17.2, 17.2, and 27.2 million elements for the 2D k-ω SST, 3D k-ω SST Wall

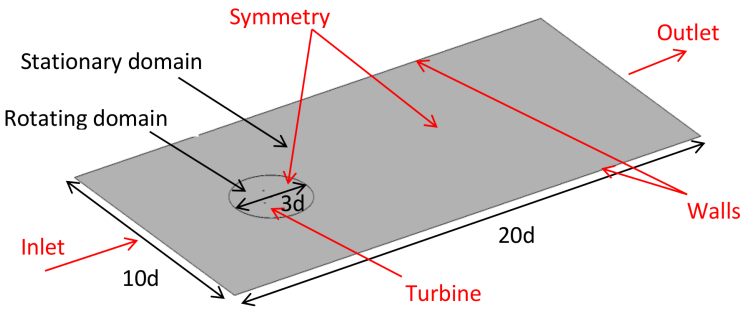

Figure 2.7: Domain boundary nomenclature and sizing for 2D domain. Total 2D domain thickness of 0.01m. Dimensions in turbine diameter d. Symmetry on both horizontal surfaces

Function, 3D BSL-RSM, 3D k-ω SST, and 3D k-ω SST Transition models respectively, with Turbine B CFD models exhibiting similar mesh element counts. The 2D model demonstrated low mesh element count independence at 0.16 million elements as a result of the significant reduction in domain size as seen when comparing Figures 2.6 and 2.7. The lower mesh count for the 3D k-ω SST Wall Function model was due to the significantly reduced inflation layer density shown in Figure 2.3 when compared to the fully resolved models. Compared to the 3D BSL-RSM and 3D k-ω SST models, the 3D k-ω SST Transition model required higher mesh density in the chord wise direction as recommended for transition region prediction (ANSYS 2010a).

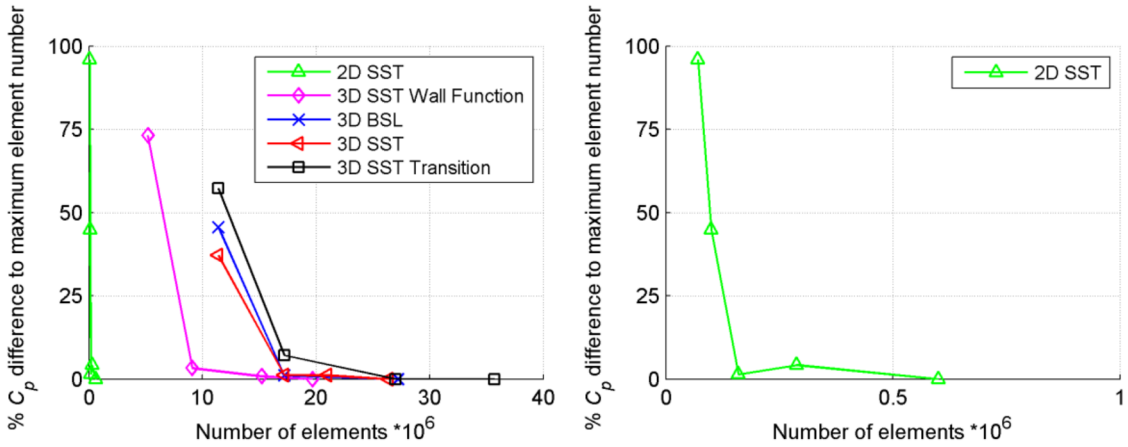

Figure 2.8: Mesh element count independence for Turbine A CFD models at λ=2.75 and an inflow velocity of 1.5 ms^{-1}. Results for 2D SST model shown on right for clarity

Simulations of 2D and 3D CFD models revealed significant differences in temporal independence as shown in Figure 2.9 for Turbine A. Temporal independence was demonstrated at

0.9° rotation per time step for all models except the 3D k-ω SST Wall Function model, which demonstrated temporal independence at 3.6° of rotation per time step. The increase in time step size for the 3D k-ω SST Wall Function model was caused by the reduction in boundary layer density. The 2D k-ω SST results were similar to the 3D k-ω SST as they used the same boundary layer mesh density. Small fluctuations in power output were noted for some simulations as time step reduced, as shown for the 3D k-ω SST model between 0.9° and 0.225°. This is prescribed to small differences in wake and dynamic stall modeling between the successive refinements. However as these fluctuations were lower than the independence criteria they were ignored, allowing the use of higher time steps to maximise computational efficiency.

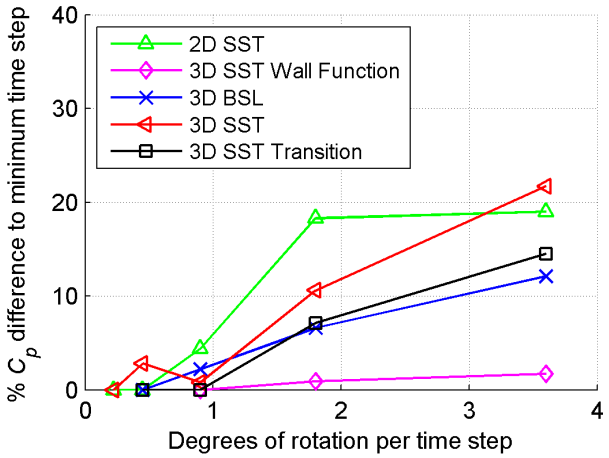

Figure 2.9: Time Independence for Turbine A CFD models at λ=2.75 and an inflow velocity of 1.5 ms^{-1}

Figure 2.10 shows the Turbine A $y+$ independence study, with independence demonstrated at an average $y+$<1 for the 2D, 3D k-ω SST, and 3D k-ω SST Transition models. Independence for the 3D k-ω SST Wall Function model was demonstrated at $y+$=29. These $y+$ ranges ensured the correct placement of the first mesh cell from the wall for the fully resolved and wall function boundary modeling techniques, and align well with recommended near wall resolution ranges for the turbulence models used (ANSYS 2010a). The higher $y+$ of the wall function model resulted in a large reduction in overall mesh element count when compared to the fully resolved model, due to reduction in boundary layer mesh density as shown in Figure 2.3. Due to dynamic nature of vertical axis turbine hydrodynamic small changes in $y+$ resulted in small differences in flow field resolution, resulting in small variations in low $y+$ C_p as shown in Figure 2.10. However, these fluctuations do not unduly

effect simulation results, as the systematic mesh independence studies used ensured than these fluctuations were less than 5% when compared to the optimal $y+$. The use of reduced $y+$ below $y+$=1 would not significantly increase simulation accuracy, but would unnecessarily increase overall simulation time. The $y+$ range used was also within that suggested by ANSYS (2010a). The small increase in $y+$ at values below $y+$=1 is a numerical effect introduced by the small cell sizing at very low $y+$ values.

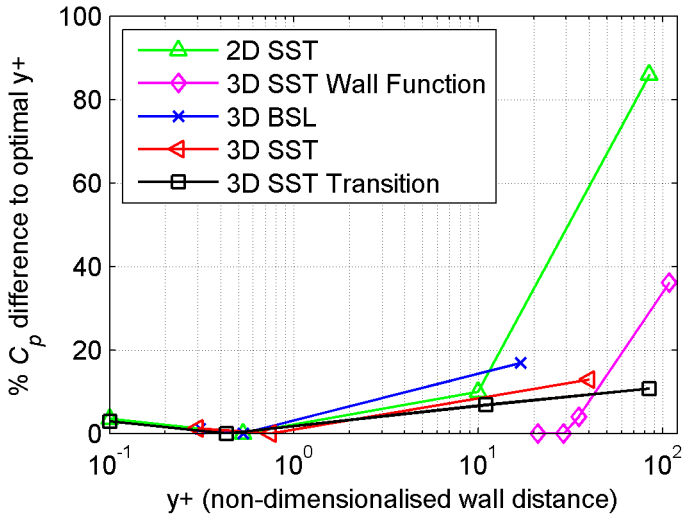

Figure 2.10: Non-dimensional first cell height ($y+$) independence study for Turbine A at λ=2.75 and an inflow velocity of 1.5 ms^{-1}. The optimal $y+$ was approximately $y+$=0.75, except for the 3D k-ω SST Wall Function model where optimal $y+$=29

Domain size studies were performed on Turbine A to ensure spatial solution independence. This was performed by examining the influence of variations of the length, width, and height of the domain on C_p whilst keeping all other variables fixed. Simulation results, as shown in Table 2.3, indicated that a domain length, width, and height of 20d, 10s, and 3.33s allowed for domain size independence. Symmetrical independence was confirmed by performing equivalent simulations on the full and half domains as shown in Figure 2.6. Total C_p differences of less than 0.4% were demonstrated between the two. This allowed the use of half domains to simulate turbine performance, reducing mesh count and thus total simulation time.

Comparisons were made between first and second order discretisation schemes for Turbine A at λ=2.75, as shown in Figure 2.11. The second order scheme resulted in significantly improved C_p accuracy when compared to EFD from literature, with the second order C_p

Table 2.3: Domain Size Independence Study for Turbine A for Half Domain 3D CFD Model Shown in Figure 6 at an Inflow Velocity of 1.5 ms^{-1} and λ=2.75

Length(d)	C_p	Change from 20d	Width(d)	C_p	%Change from 10d	Height (s)	C_p	%Change from 2.5s
5	0.285	11.3%	5	0.267	4.3%	1.25	0.276	7.8%
20	0.256	-	10	0.256	-	2.5	0.256	-
40	0.256	0.0%	20	0.251	2.0%	5	0.249	2.7%

results within the reported experimental error shown by the error bars on the EFD results in Figure 2.11 (Rawlings 2008). This occurred as the second order model was able to capture the highly transient nature of the turbine flow whilst minimizing any numerical diffusion. As a result all simulations were performed using the second order discretisation scheme.

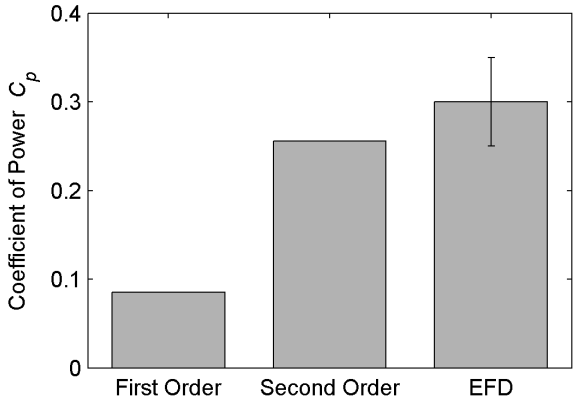

Figure 2.11: Comparison of first and second order numerical discretisation schemes with EFD C_p with error bars from literature for Turbine A at an inflow velocity of 1.5 ms^{-1} and λ=2.75 (Rawlings 2008)

2.3 Results and Discussion

Validation of both turbine models was performed against EFD results available in literature for the testing of two geometrically identical turbines conducted at the University of British Columbia's towing tank (Rawlings 2008). Power output was measured using a torque sensor and rotation rate encoder for varying rotational rates from λ=1.5 to λ=3.5 and inflow velocities from 1.5 to 2 ms^{-1}. Error bar estimates were only reported for Turbine A.

2.3.1 Computational Fluid Dynamics Simulations

The 2D and 3D CFD and EFD results for the power output characteristics for Turbines A and B, at an inflow velocity of 1.5 ms^{-1}, are shown in Figures 2.12 and 2.13 respectively.

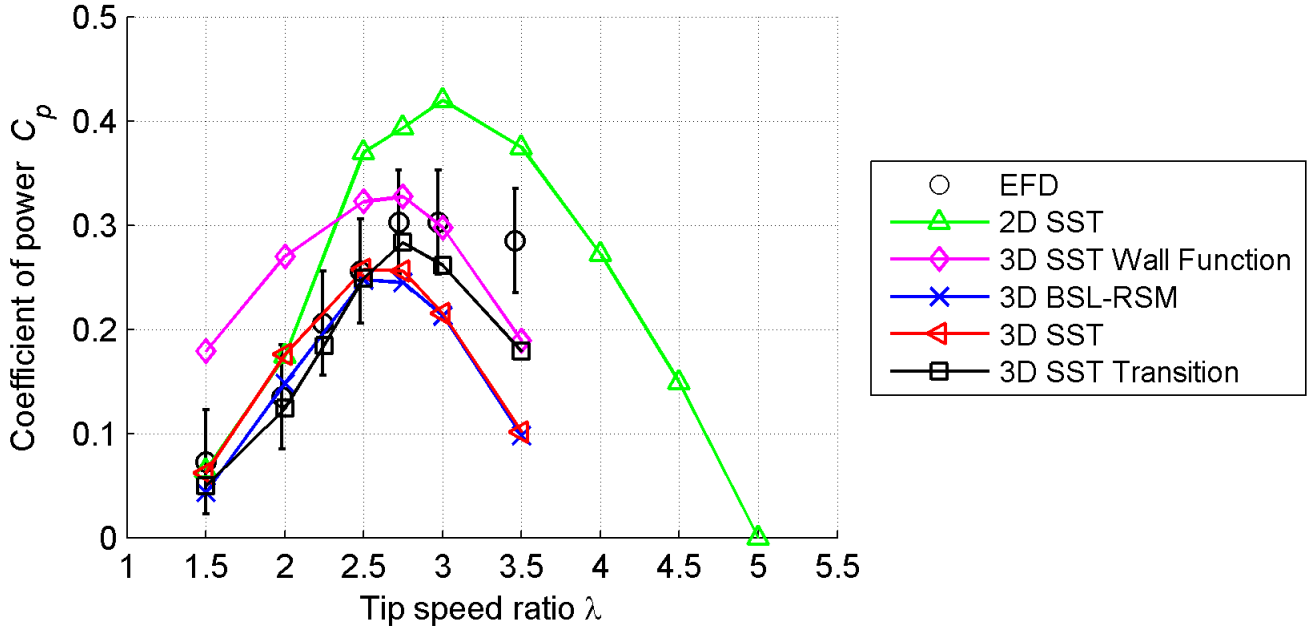

Figure 2.12: Comparison of $C_p - \lambda$ curves for Turbine A at an inflow velocity of 1.5 ms^{-1}. EFD results with error bars from literature (Rawlings 2008)

The 2D k-ω SST CFD models C_p prediction results revealed poor accuracy when compared to the 3D models and EFD from literature as shown in Figures 2.12 and 2.13. At λ=1.5 for Turbine A, C_p was predicted to within 11% of EFD, however predictions of C_p for Turbine B were 180% higher than EFD, as the 2D k-ω SST model did not account for the significant levels of strut drag on the latter turbine. As λ increased C_p diverged from the EFD results, with significant prediction errors found at high λ for both turbines. These prediction errors occurred as the resistive torque generated by the struts could not be modeled using 2D k-ω SST CFD models (Marsh et al. 2012, 2013). These simulation results indicate that 2D k-ω SST CFD models are unsuitable for the vertical axis turbine simulations, necessitating the use of full 3D simulation models.

Considering the results from the 3D k-ω SST Wall Function model against EFD C_p results obtained from literature shown in Figures 2.12 and 2.13, at low λ, C_p was over predicted

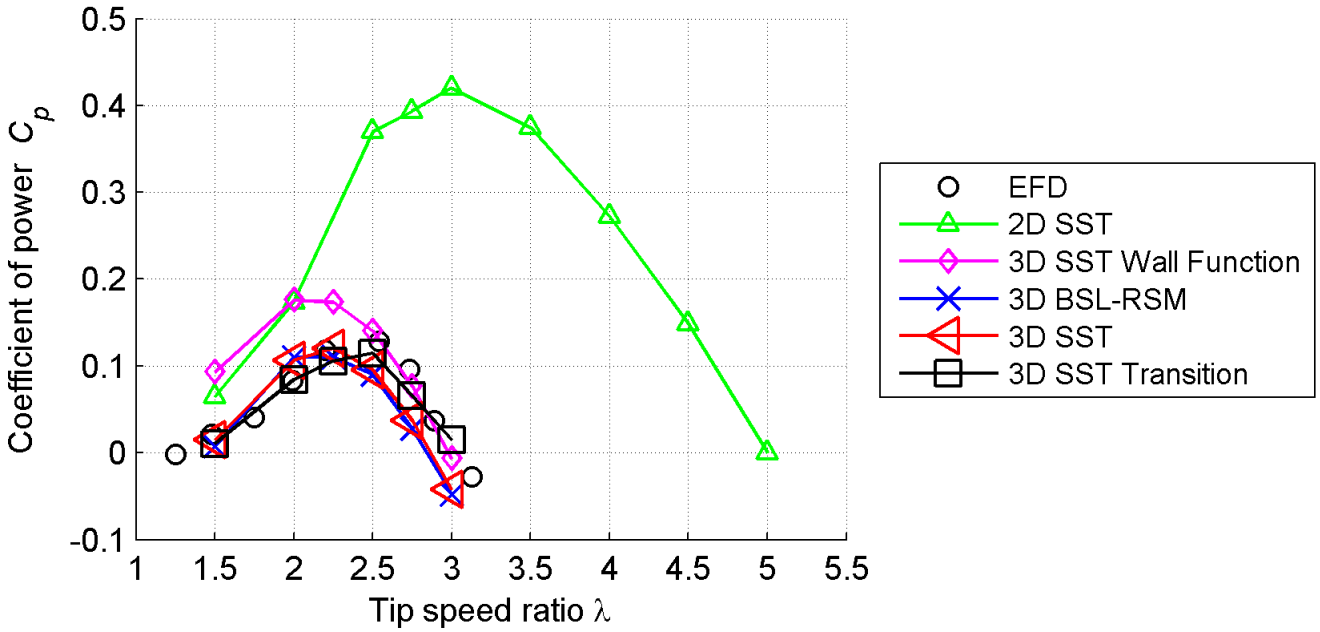

Figure 2.13: Comparison of $C_p - \lambda$ curves for Turbine B at an inflow velocity of 1.5 ms^{-1}. EFD results from literature (Rawlings 2008)

for both Turbine A and B (Rawlings 2008). Over predictions of C_p at λ=1.5 of 145% and 304% were found for Turbines A and B respectively. These occured as the wall function model does not resolve the boundary layer flow down to the sub-viscous layer, but rather applies a generalized log-wall approximation of its shape on the solution. Thus for separated flows, such as at low λ, the 3D k-ω SST Wall Function model cannot simulate the high levels of adverse pressure gradients and separation within the boundary layers. As λ increased C_p predictions appeared to slowly converge with the 3D k-ω SST model, as the increased rotational rate reduces the angle of attack range over the blades. This reduction in angle of attack reduced flow separation and adverse pressure gradients to levels that the 3D k-ω SST Wall Function model was able to accurately simulate. However, given the poor predictive ability at low to medium λ, 3D k-ω SST Wall Function models are a poor choice for vertical axis turbine simulation as they are unable to simulate operational conditions such as start-up and maximum power output accurately.

The highest correlation with EFD for all λ was found using the 3D k-ω SST Transition model, as it accounted for both 3D flow and laminar-to-turbulent flow transition effects. At low λ below the λ location of maximum C_p, all C_p results were within EFD error bars for Turbine A. For Turbine B at low λ, C_p predictions were close to EFD, with results for

example within 1.3% of EFD C_p at λ=2. The accuracy of the CFD models resulted from the accurate prediction of flow separation at the high angles of attack experienced at these low λ (Paraschivoiu 2002). The transition model also also simulated flow transition at low angles of attack that occur at high . The increased C_p simulation accuracy when compared to the fully turbulent models is due to better estimation of the wall shear and hence drag on the blades. This results in more accurate prediction of C_p at high , as shown in Figure 2.14.

Using the 3D k-ω SST Transition model maximum C_p was predicted to be within 6.6% and 10.2% of EFD results for Turbines A and B, as a result of incorporation of all geometric features in the 3D models. Although for Turbine A the C_p prediction accuracy at high λ above the λ location of maximum C_p was poor, the shape of the $C_p - \lambda$ curve for Turbine B was replicated accurately. This was due to the transition model being able to model the flow transition effects caused by the low operational Reynolds numbers of approximately 300,000, as determined using blade chord as the characteristic length .

The effect of flow transition on drag prediction can be seen in Figure 2.14. Reductions in wall shear stress are shown on the blades and struts when compared to the 3D k-ω SST fully turbulent solution. Reductions in wall shear and hence drag increase C_p at high λ as strut resistive torque is reduced. Reductions in wall shear would also improve blade lift to drag efficiency and hence increase C_p. The poor C_p prediction of Turbine A at high λ may be due to experimental inconsistencies at λ=3.5, as the C_p results of Turbine B at high λ were predicted with reasonable accuracy. Over prediction of EFD C_p at high λ may also occur as a result of blockage effects that were not accounted for in the EFD results, which can artificially increase C_p by more than 25% as shown in previous EFD studies (Bachant & Wosnik 2015). Prediction errors may also occur due to differences in the turbulence intensity levels between the CFD models and EFD testing, as high turbulence intensity levels can delay stall (Leu et al. 2012). This can lead to increases in C_p especially at high λ (Maganga et al. 2010). However no turbulence intensity measurements were recorded during EFD testing from literature to compare to CFD turbulence levels. Although the 3D k-ω SST Transition model demonstrated the highest correlation with EFD results for both turbine models it does have limitations; inherent in its current formulation is the inability to accurately predict cross-flow transition (ANSYS 2010*a*). Although this would not impact significantly on the accuracy of straight-bladed vertical axis turbine simulations, helical turbines may exhibit large degrees of cross-flow separation due to the inclination of the blades to the inflow, which the current ANSYS turbulence model may not accurately capture.

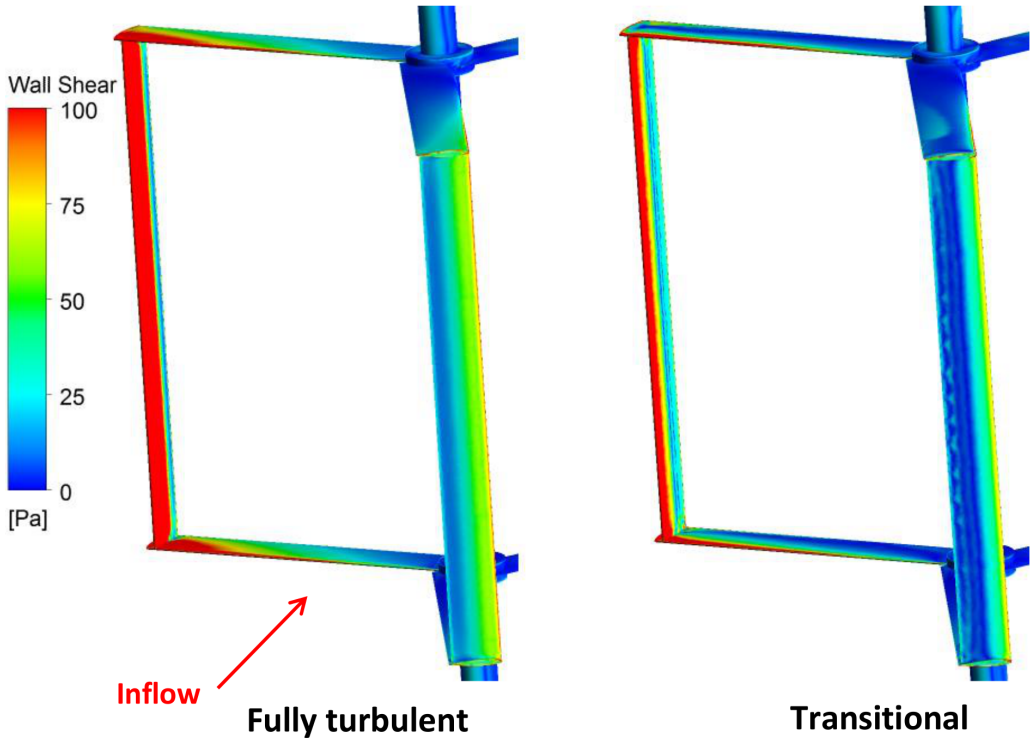

Figure 2.14: Comparison of the increase in wall shear stress simulated by the 3D k-ω SST fully turbulent model when compared to the 3D k-ω SST Transitional models, Turbine A at λ=3.5 at an inflow velocity of 1.5 ms^{-1}

Figures 2.12 and 2.13 also show C_p simulations of Turbines A and B determined using the 3D k-ω SST models. At low λ, good agreement was found between CFD and EFD results for both turbines, with all C_p results being within EFD error bars for Turbine A, and close to EFD results for Turbine B. Differences between CFD and EFD for Turbine A C_p results were 17.0% and 0.8% at λ=1.5 and λ=2.5 respectively, which although high were within reported EFD error bars. Turbine B prediction accuracy at low λ was similar, with differences in C_p prediction of 14.4% and 1.7% at λ=2 and λ=2.25 respectively.

Using the 3D k-ω SST model maximum C_p was simulated to within 14.3% and 6.3% of EFD results for Turbines A and B. This accuracy was a result of the inclusion of all geometry in the 3D models, with Turbine A results falling within reported EFD error bars from literature (Rawlings 2008). However, for both turbines C_p prediction accuracy reduced as λ increased past the location of maximum C_p, with the CFD C_p values tending to be lower than the equivalent EFD values. The authors suggest that this was due to over prediction

of turbine blade and strut airfoil drag due to the use of fully turbulent CFD models, which over estimated skin friction and hence airfoil drag at the low angles of attack experienced at high λ. This can be seen in Figure 2.14, where increased levels of wall shear stress were determined by the k-ω SST model when compared to the k-ω SST Transition model predictions.

The 3D BSL-RSM model provided reduced C_p prediction accuracy when compared to the 3D k-ω SST models for all λ as shown in Figures 2.12 and 2.13. Below λ=3, all results from Turbine A were within the EFD error bars, however C_p differences between the CFD and EFD results of 40.4% and 9.6% at λ=1.5 and λ=2 respectively were higher than those of the k-ω SST models. The prediction accuracy for Turbine B at low λ was also poor, with differences in C_p prediction being 64% and 32% at λ=1.5 and λ=2 respectively. Maximum C_p was predicted to within 18.2% and 14.1% of the EFD results for Turbines A and B respectively, notably with less accuracy than the 3D k-ω SST model. It is difficult to prescribe reasons as to this reduction in accuracy when compared to the k-ω SST models, however it appear that the BSL-RSM models may be simulating separation at a lower angle of attack than the k-ω SST models. The prediction accuracy of the BSL-RSM model reduced at high λ, which the authors ascribed to experimental inconsitincies, blockage effects, and transitional effects similar to that noted for the k-ω SST model simulations. Solutions using the BSL-RSM model, with its additional transport and dissipation equations, did not improve simulation accuracy when compared to the standard isotropic eddy-viscosity based models.

2.3.2 Computational Requirements and Numerical Simulation Recommendations

The computational efficiency of the turbulence model and 2D and 3D investigations were established by comparing simulation time and computer cluster core requirements to simulate one revolution as shown in Table 2.4 at λ=2.75. All simulations were performed on a distributed cluster comprising of Intel Xeon 5160 3.0GHz processors with 2GB memory per core.

Table 2.4: Simulation Time and Computational Requirements for One Turbine Revolution. Turbine A at λ=2.75 at an Inflow Velocity of 1.5 ms^{-1}

Turbulence Model	2D SST	3D SST Wall Function	3D BSL-RSM	3D SST	3D SST Transition
Time (minutes)	90	400	2700	1200	6200
Cores	4	16	24	24	24

2.3.3 Numerical Simulation Recommendations

Key conclusions were gained from evaluations of power output prediction accuracy when combined with the determination of computational resource requirements for each model, namely that:

- 2D k-ω SST models were computationally efficient due to reduction in mesh size when compared to the 3D models. However C_p prediction accuracy was very poor when compared to EFD, as strut and end influences were not simulated;
- 3D k-ω SST Wall Function models offered reduced simulation times than the fully resolved models, as a result of significant reductions in mesh size. However C_p prediction accuracy was poor when compared to fully resolved CFD models and also to EFD, as they were unable to model separation at low rotational rates accurately;
- 3D BSL-RSM models were computationally demanding due to the extra seven transport and dissipation equations solved. However C_p prediction accuracy was reduced when compared to 3D k-ω SST models and EFD due to separation prediction error;
- 3D k-ω SST Transition models were accurate but required excessive computation times due to large mesh element counts necessary for element count independence, as well as for the solution of the additional transition equations. Overall simulation time increased by a factor of more than five when compared to the 3D k-ω models;
- A suitable balance between computational requirements and C_p prediction accuracy was found using turbulent 3D k-ω SST models.

2.3.4 Geometrical Effects on Power Output

The influences of geometrical design on power output were captured by the 3D CFD models as shown in Figures 2.12 and 2.13. Using the 3D k-ω SST model, Turbine A power output was found to be 115% higher than Turbine B, as although the turbines shared the same blade section, they differed in strut section location, cross-section and mounting tab design. This result is consistent with the 136% increase in power output efficiency found by EFD from literature (Rawlings 2008). The use of 3D CFD models allows differences of power output caused by geometrical design to be quantified without the need for EFD. If investigation of the relative performance of blade section variations is desired it may be possible to use 2D CFD models, however they will poorly capture total power output and hence should not be used for determining overall power generation capacity.

2.3.5 Flow Visualisation

The use of CFD also allows for flow visualisation without the expense and difficulty of EFD methods such as Particle Image Velocimetry (PIV) (Ferreira 2009*a*). Visualisation of vortex shedding for the 2D and 3D k-ω SST models is shown in Figures 2.15 and 2.16. The 2D k-ω SST models were unable to capture any strut or blade tip losses due to the geometrical layout of vertical axis turbines, and can only simulate blade and shaft vortex shedding. As a result the 2D k-ω SST poorly predicts C_p as shown in Figures 2.12 and 2.13. Conversely, the 3D k-ω SST CFD models resolved all key hydrodynamic flow features including blade tip and strut vortex shedding as shown in Figure 2.16, due to the inclusion of all geometrical features.

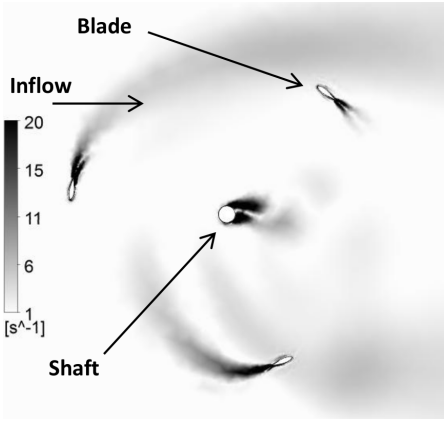

Figure 2.15: Vortex structure visualisation for Turbine A at λ=2.75 for the 2D k-ω SST model. Vorticity in stationary frame from 1 to 20 s^{-1} at an inflow velocity of 1.5 ms^{-1}

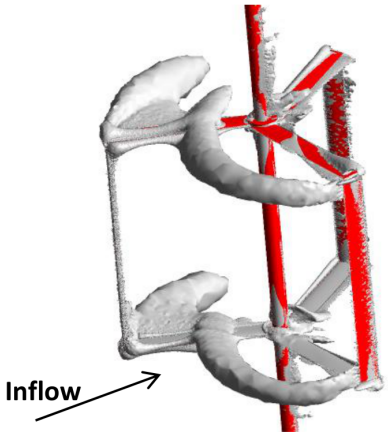

Figure 2.16: Vortex shedding visualisation for Turbine A at λ=2.75 for the 3D k-ω SST model. Vorticity of 16 s^{-1} at an inflow velocity of 1.5 ms^{-1} at λ=2.75

2.4 Conclusions

The power output of two vertical axis turbines was simulated using 2D and 3D CFD models with varying turbulence and boundary layer flow modeling techniques. Although the k-ω SST Transition model resulted in the highest correlation with experimental power output results, the authors suggest that the 3D k-ω SST model is better suited for vertical axis turbine simulation. It offers comparable accuracy to the k-ω SST Transition model at low to medium rotational rates, as well as similar accuracy for maximum power output predictions, without the additional meshing and excessive computational expense of the transition model.

The development of CFD flow transition models is ongoing which will hopefully reduce the computational requirements of transitional models, which were found to be excessive in this study, limiting their utility. The authors suggest that this study be revisited as transition models improve, as they show promising results especially at high rotational rates.

Future work is planned to investigate the structural loading characteristics of straight and helical-bladed turbines to determine any possible differences, and thus advantages, between the two turbine designs. This work has demonstrated that fully turbulent 3D k-ω SST CFD models with full resolved boundary layers must be used to accurately simulate turbine power output.

Chapter 3

Three-dimensional Numerical Simulations of Straight-Bladed Vertical Axis Tidal Turbines Investigating Power Output, Torque Ripple and Mounting Forces

This refereed journal paper was published in *Renewable Energy*. The citation for this journal paper is:

Marsh P., Ranmuthugala, D., Penesis, I., & Thomas, G. Three-dimensional Numerical Simulations of Straight-Bladed Vertical Axis Tidal Turbines Investigating Power Output, Torque Ripple and Mounting Forces, *Renewable Energy*, 83 (2015), pp.67-77.

Abstract

Three straight-bladed vertical axis turbine designs were simulated using Three-Dimensional (3D) transient Computational Fluid Dynamics (CFD) models, using a commercial Unsteady Reynolds Averaged Navier-Stokes (URANS) solver. The turbine designs differed in support strut section, blade-strut joint design and strut location to evaluate their effect on power output, torque fluctuation levels and mounting forces. Simulations of power output were performed and validated against Experimental Fluid Dynamics (EFD), with results capturing the impacts of geometrical changes on turbine power output. Strut section and blade-strut joint design were determined to significantly influence total power output between the three turbine designs, with strut location having a smaller but still significant effect. Maximum torque fluctuations were found to occur around the rotation speed corresponding to maximum power output and fluctuation levels increased with overall turbine efficiency. Turbine mounting forces were also simulated and successfully validated against EFD results. Mounting forces aligned with the inflow increased with rotational rates, but plateaued due to reductions in shaft drag caused by rotation and blockage effects. Mounting forces perpendicular to the inflow were found to be 75% less than forces aligned with the inflow. High loading force fluctuations were found, with maximum values 40% greater than average forces.

3.1 Introduction

A combination of social, environmental and economic interests is driving research into renewable energy, the production of which is a central facet of sustainable human development. The energy held within the ocean could be harnessed in a renewable, sustainable and economic manner, with over 200 devices proposed to extract this energy (Arvizu et al. 2011). However, of these devices only a few have been constructed or are near commercial feasibility (Osman et al. 2011). Vertical and horizontal axis turbines are among these devices being developed to transform the ocean's kinetic energy contained within tides and currents into usable energy forms (Osman et al. 2011).

Vertical axis turbines as shown in Figure 3.1 have two key advantages when compared to horizontal axis designs: they are flow-directional independent (Dai & Lam 2009); and all electrical components can be installed above the free surface of the water, thus simplifying installation and maintenance (Kirke 2011). With increased interest in vertical axis turbines,

driven in part by the plateauing of efficiency of horizontal axis designs (Scheurich et al. 2011), further research into the development of improved turbine designs is required. This has proven challenging due to the complexity of vertical axis turbine hydrodynamic flow fields which are notoriously difficult to predict (Scheurich et al. 2011).

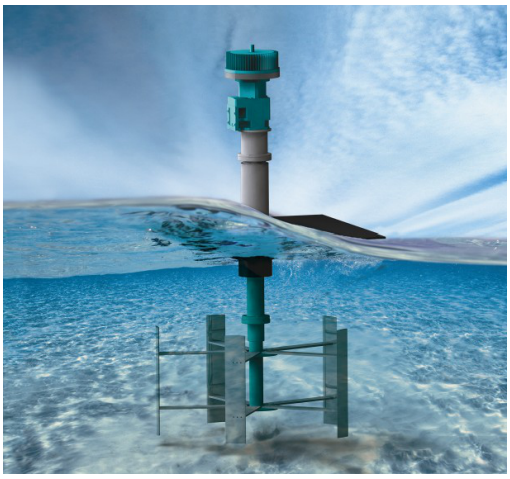

Figure 3.1: Vertical Axis turbine for tidal and current power generation (*New Energy Corporation* 2014)

The complexity of vertical axis turbine hydrodynamics is due to three distinct phenomena that generate high levels of unsteady flow and thus complex vortex shedding and flow diffusion effects:

- continually varying blade angles of attack;
- blade-wake interactions; and
- strut effects.

At low rotational rates the flow is dominated by high levels of static and dynamic stall as the blade angles of attack widely vary due to the low blade velocities relative to the inflow velocity (Paraschivoiu 2002). At higher rotational rates the flow field is dominated by wake interaction as the blades traverse through the disturbed wake and shed vortices of previous blades (Scheurich et al. 2011). Additionally, as rotational rates increase the influence of strut drag increases, reducing the overall torque generated (Marsh et al. 2013). These complex flow field phenomena and the resultant vortex shedding and flow diffusion effects must be accurately captured by the simulation models used in order to accurately simulate turbine hydrodynamics and thus turbine efficiency.

A wide variety of numerical models can be used to simulate vertical axis turbine performance and hydrodynamics, ranging from reduced order blade-element based models (Marsh et al. 2013, Paraschivoiu 2002, Templin 1974), vortex methods (Li & Çalişal 2010*a*, Li & Calisal 2010*b*), Two-Dimensional (2D) Computational Fluid Dynamics (CFD) models (Malipeddi & Chatterjee 2012), quasi 2D or 2.5D Large Eddy Scale (LES) simulations which treat the blades as possessing infinite length (Li et al. 2013), and Three-Dimensional (3D) CFD models (Castelli et al. 2010, Marsh et al. 2012), with increasing levels of simulation complexity and computational resource requirements. Commercial CFD software such as ANSYS Fluent and CFX are commonly used to simulate turbine power output and hydrodynamics (Dai & Lam 2009, Castelli et al. 2010, Li et al. 2013, Malipeddi & Chatterjee 2012, Marsh et al. 2012, 2013, Navabi 2008, Nobile et al. 2011, Rossetti & Pavesi 2013), with most CFD simulations performed in 2D as 3D models require lengthy simulation times (Li & Calisal 2010*b*, Li et al. 2013, Rossetti & Pavesi 2013). However, 2D (and by extension 2.5D) CFD simulations often unsatisfactorily estimate power output, as the losses due to strut drag and finite blade lengths are not simulated (Marsh et al. 2012, 2013). To accurately capture all hydrodynamic phenomena, CFD models should include all significant geometrical features, necessitating the use of full 3D simulation approaches. Although empirical corrections for 2D CFD and blade-element models are available (Li & Calisal 2010*b*, Marsh et al. 2013, Navabi 2008), in this work evaluations were conducted to determine whether recent advances in distributed computing now make 3D CFD simulation approaches feasible.

In this work simulations were performed using 3D CFD models to predict the power output, torque fluctuations and loading characteristics of three straight-bladed vertical axis turbines. These turbines used the same blade section but different strut sections, blade-strut joint designs and strut locations to evaluate the effect of geometrical changes on turbine performance. Power output curves were generated for all turbines, two of which were compared to Experimental Fluid Dynamics (EFD) results to validate the simulation models developed. The levels of torque fluctuations and total mounting forces were also characterised to determine their relationship with strut location, strut section and total power output. All CFD methods were verified using mesh independence criteria with results validated against EFD where possible.

3.2 Numerical Simulations

Transient time-accurate 3D CFD simulations were conducted in ANSYS CFX software utilising the URANS-based k-ω Shear Stress Transport (k-ω SST) turbulence model using an element-based finite volume approach (ANSYS 2010*a*). Ansys CFX was utilised as it is commonly used in industry and its formulation allows for efficient distribution on computing clusters to reduce total simulation time (ANSYS 2010*a*). Unsteady models were used due to the high levels of unsteady flow caused by the rotation of the turbine, with the fluid modelled as an incompressible fluid as all flow velocities were significantly less than Mach=0.3.

3.2.1 Turbine Geometry

Three straight-bladed vertical axis turbine designs were simulated, labelled Turbines A, B and C, with the overall geometrical dimensions and configurations as outlined in Table 3.1, which were based on the EFD turbines of Rawlings (Rawlings 2008). These turbines were simulated as they allowed for comparisons of power output for varying geometrical designs as well as validation of simulation results against EFD. All turbines had two struts per blade, with strut section, location and blade-strut joint design details outlined in Figure 3.2.

Table 3.1: Common Geometrical Features of the Three Turbine Configurations (Rawlings 2008)

Geometry	Dimensions
Number of blades	3
Number of struts	2 per blade
Blade section	NACA 634021
Blade chord	0.065m
Radius	0.457m
Blade span	0.686m

3.2.2 Key Performance Parameters

A number of performance parameters were investigated to enable the quantification of turbine efficiency and loading characteristics. Turbine power output was expressed as a non-dimensionalised power coefficient C_p, where,

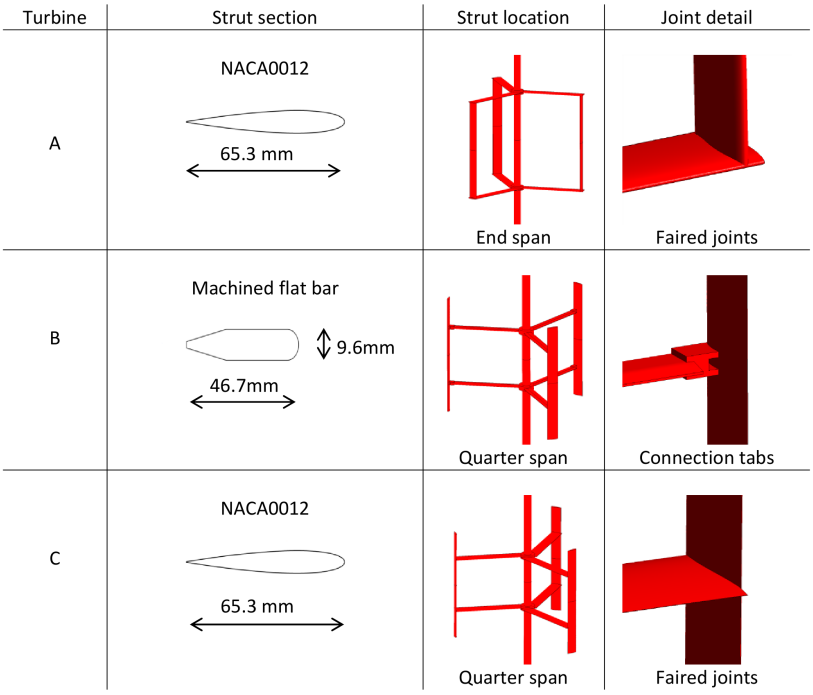

Figure 3.2: Turbines A, B, and C strut section, strut location and blade-strut joint detail (Rawlings 2008)

$$C_p = \lambda \, C_m \tag{3.1}$$

where tip speed ratio λ was defined as,

$$\lambda = \frac{r\omega}{V} \tag{3.2}$$

where ω was the turbine rotational rate, r was the turbine radius, and V was the inflow velocity. The turbine torque coefficient C_m was determined as,

$$C_m = \frac{T}{0.5\rho V^2 S r} \tag{3.3}$$

where ρ was the water density (set to 1000 $\frac{kg}{m^3}$ for all simulations), S was the turbine frontal area, and the moment, T generated by the turbine was taken from CFD or EFD results.

3.2.3 Computational Domain and Boundary Conditions

The boundary conditions used for all CFD studies are outlined in Table 3.2 for the boundaries shown in Figure 3.3. The boundary conditions simulated free stream conditions ensuring that the turbine was isolated from any boundary layer or blockage effects and allowed full wake development. Domain symmetry was used to reduce overall mesh size by splitting the domain along the horizontal centre plane, with the resultant half domain used for all simulations, as shown in Figure 3.3. No free surface effects were simulated, as the turbine was assumed to operate at sufficient depth to minimise any surface effects.

Table 3.2: Domain Boundary Conditions for CFD Models

Wall	Boundary condition
Inlet	Uniform flow: 1.5 ms^{-1}
Outlet	Relative Pressure: 0 Pa
Walls	Free slip walls
Turbine	No slip walls
Symmetry	Symmetry walls

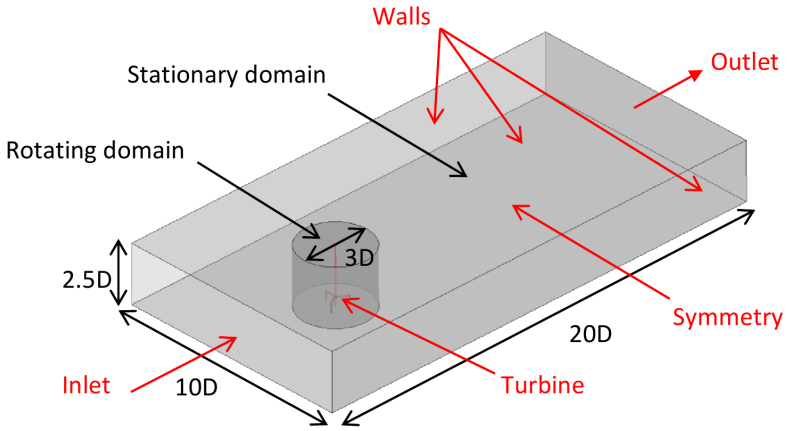

Figure 3.3: Domain boundary nomenclature and sizing, dimensions in turbine diameters D. Plane of symmetry on bottom surface

The CFX transient rotor-stator model was utilised to simulate rotation at each time step, with the rotation interface modelled using a General Grid Interface (GGI). The GGI method placed an interface between the stationary outside domain and the rotating inner domain, shown in Figures 3.3 and 3.4, allowing flow values to be calculated on either side of the boundary by an intersection algorithm (ANSYS 2010*a*). This GGI interface was set at a

distance of 1.5 times the turbine diameter, D, from the turbine rotation axis, and mesh density was increased on the interface to limit interpolation errors on C_p predictions. For all simulations the inner domain was rotated at the desired λ, and for validation purposes this corresponded with the relevant EFD rotational rates.

All CFD meshes were generated with ANSYS CFX 13.0 mesher (ANSYS 2010*b*) using unstructured tetrahedral elements. All 3D geometrical features, including all blades, hubs, shafts, struts and blade-strut joints were modelled, with the main mesh features shown in Figure 3.4. Mesh density was refined by specifying face sizing, cell curvature angle and expansions rates on areas of interest, such as on blades, struts, and the turbine wake to fully capture flow hydrodynamics. Inflation layers were utilised to control cell heights near all surfaces to resolve the boundary layer flow. Conversely, the density of the mesh was reduced in regions such as the boundary fields where a coarse mesh was found sufficient.

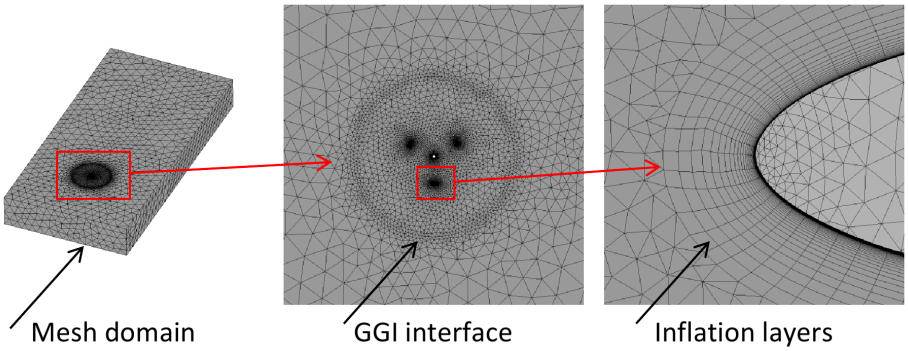

Figure 3.4: Mesh domain showing overall mesh domain, GGI interface, and inflation layer detail on the blade surface

3.2.4 Turbulence Model and Discretisation Schemes

The k-ω SST turbulence model was selected as it has previously been successfully used to simulate turbine performance (Castelli et al. 2010, Dai & Lam 2009, Gretton 2009, Lain & Osorio 2010, Marsh et al. 2013, Nobile et al. 2011) due to its ability to model both the boundary layer and the free stream regions, as well as offering improved prediction of flow separation and adverse pressure gradients by the inclusion of transport effects into the formulation of the eddy-viscosity (ANSYS 2010*a*, Menter 1994). The height of the first cell layer on all turbine surfaces was specified to ensure that it was within the viscous sub-layer, with resultant average $y+$ (the dimensionless distance from the wall) values less than 1. Simulations using reduced boundary layer inflation density and thus higher $y+$ values resulted

in reduced simulation accuracy, as the ANSYS-prescribed wall functions (ANSYS 2010*a*) were unable to resolve the flow near the walls due to high levels of separation and adverse pressure gradients. All simulations were performed using a high order advection and second order backwards Euler transient scheme.

To reduce simulation time, simulations were initialised using previous solutions and were deemed completed when the magnitude of torque fluctuations over each revolution reached a quasi-steady state, usually taking 2-3 revolutions. Convergence was achieved when residuals converged to within 10^{-4} for each time step and reduced by more than three orders of magnitude. An inlet turbulence intensity level of 5% was used for all simulations as commonly performed (Dai & Lam 2009, Marsh et al. 2012, 2013, Rossetti & Pavesi 2013), as EFD data was not available.

3.2.5 Grid Independence Studies

Studies of the influence of grid resolution factors, including mesh density, time step size, domain length, width, height and domain symmetry were conducted to ensure grid independence. These investigations were performed both quantitatively, by examining relationships between mesh grid resolution and C_p, as well as qualitatively, with graphical methods used to evaluate any changes between grid resolution factors. Quantitative independence was deemed satisfactory when changes in grid parameters resulted in C_p differences of less than 5%, resulting in a suitable balance between solution independence, speed and computational effort (Tu et al. 2013).

Mesh Density Independence

Mesh density independence was evaluated for five densities, shown in Figure 3.5. Independence was demonstrated for Turbine A at a minimum mesh density of 5x10^{-4} m, corresponding to 17.2 million elements, with a visual comparison of mesh density shown in Figure 3.6. Predictions of C_p were sensitive to changes in mesh density, with increased mesh resolution on blade surfaces needed to capture the complex flow structure. Using similar methods, mesh density independence for Turbines B and C was determined corresponding to 17.3 million and 16.6 million elements respectively.

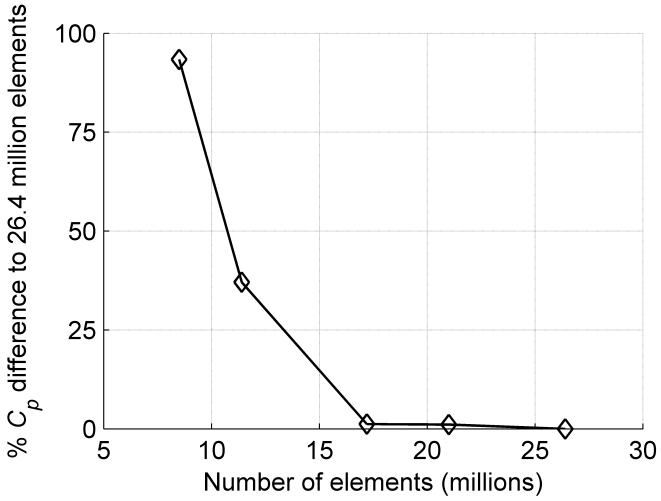

Figure 3.5: Mesh density independence study for Turbine A at an inflow velocity of 1.5 ms^{-1} and λ=2.75

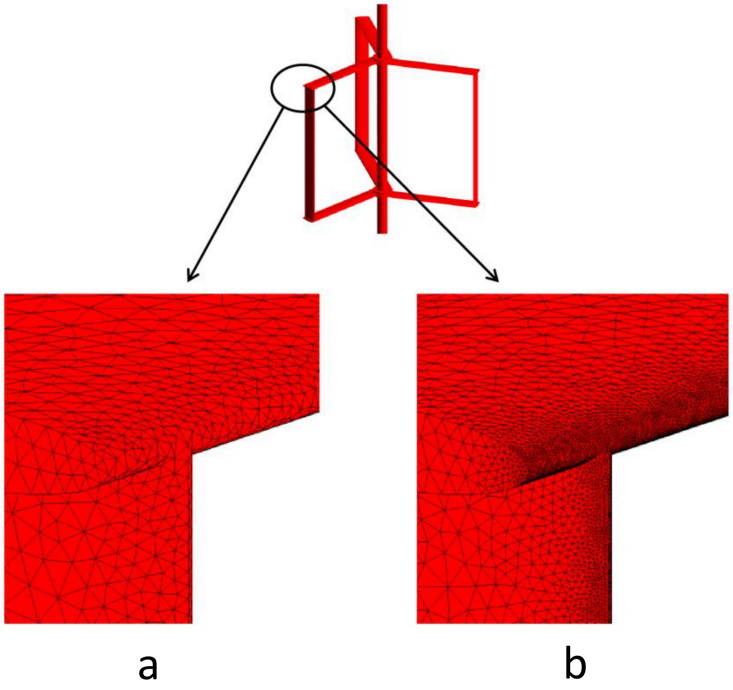

Figure 3.6: Comparison of mesh density on surfaces of blades and struts between (a) 8.5 million and (b) 27 million elements

Time Step Independence

Time step studies were performed to ensure temporal C_p independence, critical due to the highly transient nature of the flow. Simulations were performed for Turbine A using time steps from 0.225° to 3.6° of turbine rotation per step with 17.2 million elements. Independence was determined at a time step of 0.9° rotation per step as shown in Figure 3.7. Using similar methods time step independence for Turbines B and C was found at 0.9° rotation per step. Due to dynamic nature of vertical axis turbine hydrodynamic small changes in time step or other variables resulted in small differences in flow field resolution, resulting in small changes in C_p as shown in Figure 2.7. However, these fluctuations do not unduly effect simulation results, as systematic mesh independence studies used ensure than these fluctuations were less than 5%. The use of reduced time step would not significantly increase simulation accuracy, unnecessarily increasing overall simulation time.

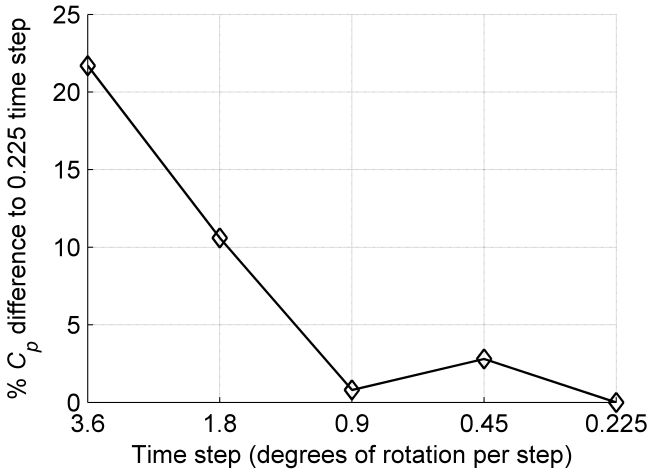

Figure 3.7: Time step independence study for Turbine A at an inflow velocity of 1.5 ms^{-1} and λ=2.75

Domain Size Independence

Domain size independence studies were performed to ensure that the turbine was isolated from any domain wall or blockage effects and to allow full wake development, with changes in simulation domain length, width, and height. Results for Turbine A, shown in Table 3.3, indicate that a domain length of 20D, width of 10D and height of 2.5D, with the turbine located 5D from the inlet, allowed full wake development whilst minimising domainwall and blockage effects. Qualitatively domain wall height effects are shown in Figure 3.8, where the proximity of the wall to the turbine due to the low domain height of 1.25D increased flow

Table 3.3: Domain Size Independence Study for Turbine A at 1.5 ms^{-1} and λ=2.75

Length(D)	C_p	Change from 20D	Width(D)	C_p	%Change from 10D	Height	C_p	%Change from 2.5D
5	0.285	11.3%	5	0.267	4.3%	1.25	0.276	7.8%
20	0.256	-	10	0.256	-	2.5	0.256	-
40	0.256	0.0%	20	0.251	2.0%	5	0.249	2.7%

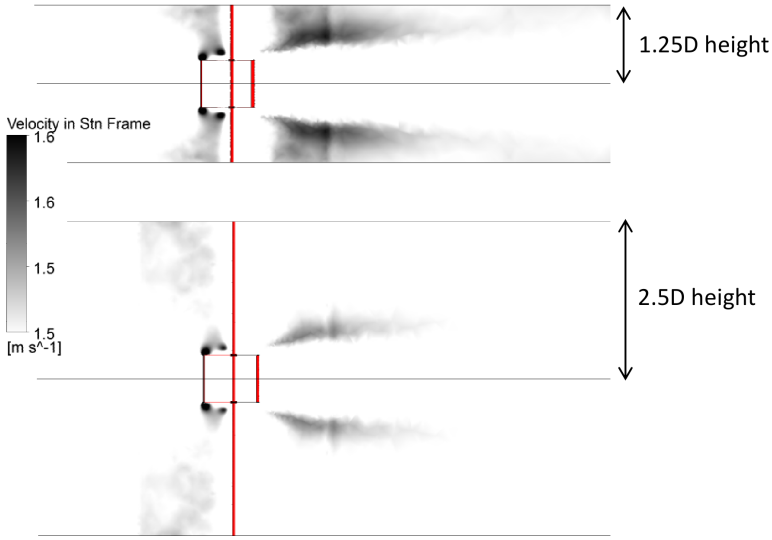

Figure 3.8: Comparison of flow velocity for domain heights of 1.25D and 2.5D showing increase in velocity due to flow constriction, Turbine A at an inflow velocity of 1.5 ms^{-1} and λ=2.75

velocity through the domain due to flow constriction, artificially increasing C_p. Although not studied here this constriction effect could be harnessed to increase C_p through the use of shaped ducts, walls, limited water depths, or by arranging turbines in a tidal fence (Malipeddi & Chatterjee 2012).

Domain Symmetry Validation

In order to validate the use of the half domain split along the horizontal mid plane, equivalent simulations were carried out on full and half domains. Results are shown in Table 3.4, with differences in C_p of less than 0.4% between the two domains. Velocity profiles for both the half and full domain, shown in Figure 3.9, reveal minimal difference in velocity distribution. This allowed the use of the half domain thereby reducing overall mesh size by two.

Table 3.4: Comparison of C_p for Symmetrical and Full Domains at an Inflow velocity of 1.5 ms^{-1} and λ=2.75

Domain	Symmetrical domain	Full domain
C_p	0.256	0.255
C_p change from symmetrical domain	-	0.4%

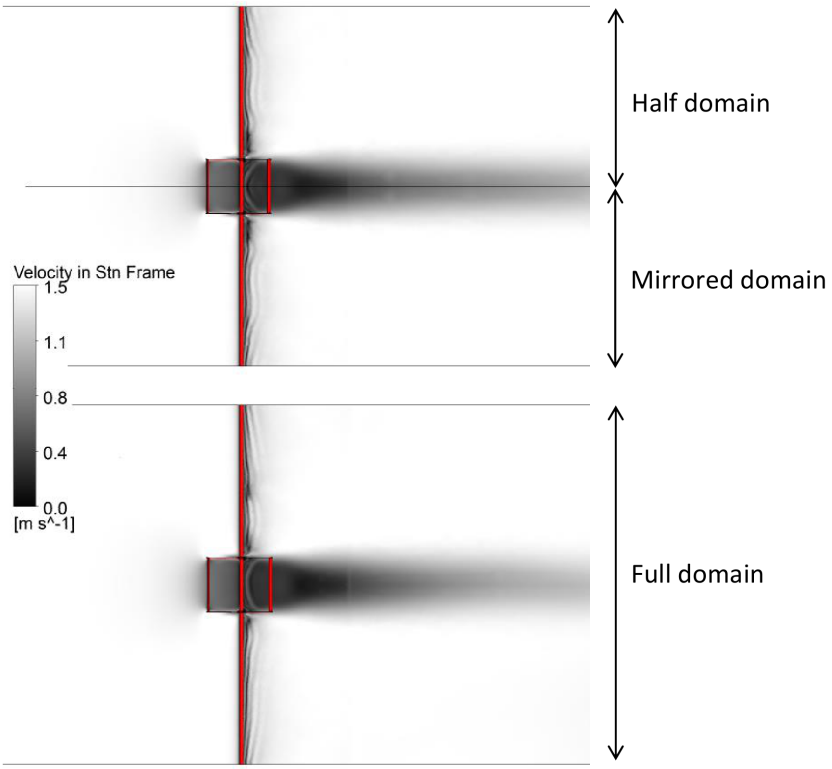

Figure 3.9: Velocity in stationary frame comparisons for half domain and full domain for Turbine A at an inflow velocity of 1.5 ms^{-1} and λ=2.75

3.2.6 Numerical Simulation Time

Numerous authors (Li & Çalişal 2010*a*, Li et al. 2013, Nobile et al. 2011) have suggested that 3D CFD models are not practical for turbine performance investigations due to their excessive simulation time and computational requirements. However full 3D simulations are now feasible due to increases in cluster power and the increased efficiency of distributed CFD solutions, with C_p simulations for one revolution at each λ taking 24 h on an 18 core cluster comprising of Intel Core 2 Quad Q9300 processors with 2 GB memory per core, allowing the simulation of vertical axis turbine performance in a timely and efficient manner. All simulations were performed using URANS models, which combined with free surface modelling assumptions minimised simulation time when compared to numerical methods such as LES.

3.3 Results and Discussion

Simulations of power output, torque fluctuations and mounting forces were obtained for Turbines A, B and C at an inflow velocity of 1.5 ms^{-1}. These simulations were performed at varying rotational rates using the simulation settings outlined in Table 3.5.

Table 3.5: Main CFD Simulation Settings

CFD	Setting
Turbulence model	k-ω SST
Time step	0.9° rotation per time step
Advection scheme	High order
Transient scheme	Second order backwards Euler
Domain length	20D
Domain width	10D
Domain height	2.5D

3.3.1 Validation of Numerical Simulations with Experimental Fluid Dynamics

Validation studies were performed against EFD tests at the University of British Columbia's towing tank, an approximately 60.1m long, 3.7m wide and 2.4m deep facility (Rawlings 2008). Using a torque sensor and rotation rate encoder, C_p for varying λ were obtained at a series of flow velocities from 0.75 ms^{-1} to 2.24 ms^{-1}, with λ varied using a motor drive unit through a 20:1 gearbox. Shaft force was measured using two load cells mounted to

the vertical shaft. The turbine models A and B simulated in this project were based on two of the EFD turbines tested by Rawlings (Rawlings 2008), enabling the equivalent CFD simulations to be validated.

Comparisons of CFD and EFD $C_p - \lambda$ curves for Turbines A and B are shown in Figure 3.10. At low λ, good agreement was found between CFD and EFD results for both turbines. Below λ=3 all Turbine A results were within EFD error bars, with C_p differences between CFD and EFD results of 17% and 0.8% at λ=1.5 and 2.5 respectively. Turbine B prediction accuracy at low λ was similar, with differences in C_p prediction of 29.2%, 14.4% and 1.7% at λ=1.5, 2 and 2.25 respectively. However, for both turbines C_p prediction accuracy reduced as λ increased past the location of maximum C_p, with CFD C_p values shifted lower. The authors suggest that this was due to over prediction of turbine blade drag due to the use of a fully turbulent CFD model. This model can overestimate skin friction and hence drag (Sørensen 2009) particularly at low angles of attack, reducing C_p at high λ where the blade angles of attack are low (Paraschivoiu 2002). Improvements of simulation accuracy at high λ may be possible using newly developed transitional turbulence models that can account for this laminar-to-turbulent transition behaviour (ANSYS 2010*a*). Over prediction of C_p at high λ may also occur as a result of blockage errors that were not accounted for in EFD results which could artificially increase EFD C_p (Bahaj et al. 2007). Over prediction may also occur due to differences in the turbulence intensity levels between the CFD models and EFD testing, as high turbulence intensity levels can delay stall (Leu et al. 2012). This can lead to increases in C_p especially at high λ (Maganga et al. 2010), however no turbulence intensity measurements were recorded during EFD testing to compare to CFD turbulence levels.

Significantly both CFD models were able to accurately capture the effect of geometrical changes on maximum C_p, which was simulated to within 14.3% and 6.3% of maximum C_p EFD results for Turbines A and B respectively. This prediction accuracy is much higher than previous vertical axis turbine CFD predictions, which exhibit maximum C_p prediction errors of more than 45% (Castelli et al. 2010, Danao 2012, Malipeddi & Chatterjee 2012, Matre et al. 2013, McLaren 2011), possibly due to the inclusion of the full turbine geometry in the present study. The use of 3D models also allows for the direct simulation of C_p without the need for empirical correction for 2D models as previous used (Li & Calisal 2010*b*, Navabi 2008, Marsh et al. 2013).

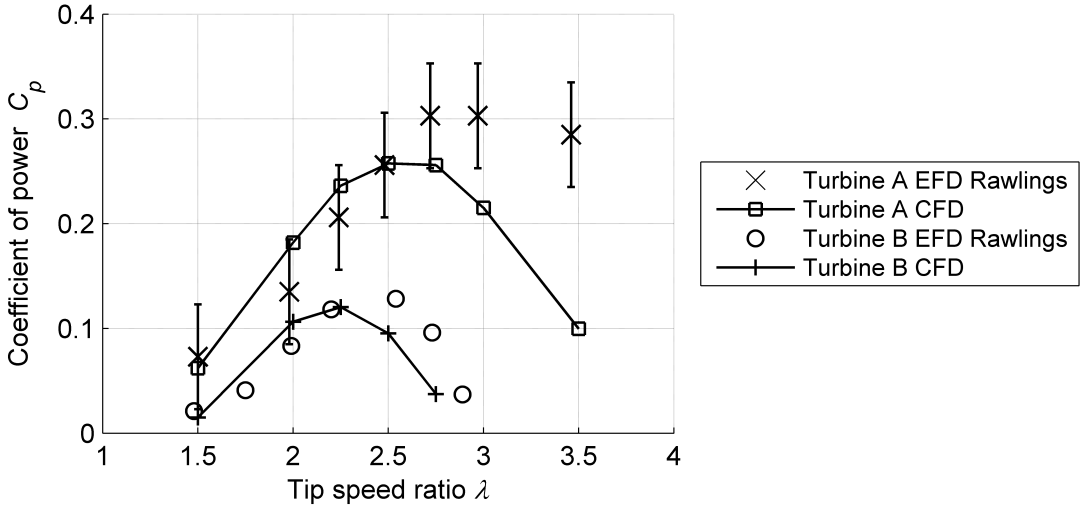

Figure 3.10: Comparison of CFD and EFD $C_p - \lambda$ curves for Turbines A and B at an inflow velocity of 1.5 ms^{-1}. Error bars only reported for EFD Turbine A (Rawlings 2008)

It has previously been suggested that URANS methods are unable to accurately predict vertical axis turbine blade vortex shedding and flow diffusion, requiring higher order CFD methods such as Large Eddy Simulation (LES) (Li et al. 2013). However, the authors believe that the accuracy of 3D CFD simulations when compared to EFD results, as demonstrated in Figure 3.10, suggests that reasonable estimates of performance coefficients such as C_p can be obtained by URANS methods, and that resolution of small-scale flow field detail by LES or Direct Numerical Simulation (DNS) methods may not be necessary. Previous URANS C_p prediction errors of more than 45% (Castelli et al. 2010, Danao 2012, Malipeddi & Chatterjee 2012, Matre et al. 2013, McLaren 2011) may be influenced more by their 2D nature than overall CFD approach, with the lack of strut and tip effects having a greater influence on C_p predictions than poor fine-scale vortex resolution. Comparisons of 3D CFD simulations with and without struts are included in Appendix B, whcih demonstate the influence of strut modelling on C_p prediction accuracy. Validation of this hypothesis could be performed by comparing flow field simulations with EFD using Particle Image Velocimetry (PIV) to establish the accuracy of the simulated vortex shedding and flow diffusion effects and their influence on turbine performance characteristics (Ferreira 2009*b*).

3.3.2 Numerical Simulation of Power Output

Using the validated CFD simulation methods $C_p - \lambda$ curves for Turbines A, B and C were determined, and are shown in Figure 3.11. Although the turbines were the same in overall

geometrical dimensions, there were significant C_p variations between the turbine designs for all λ as a result of the changes in strut section, blade-strut joint design and strut location.

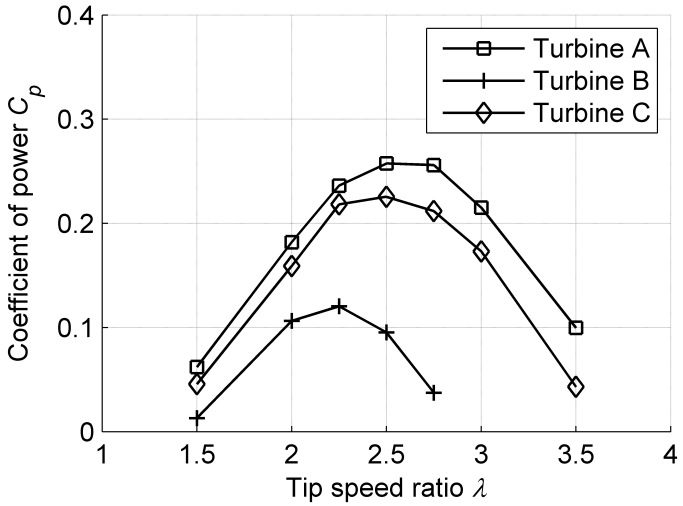

Figure 3.11: Comparisons of CFD $C_p - \lambda$ curves for Turbines A, B, and C at an inflow velocity of 1.5 ms^{-1}

3.3.3 Influence of Strut Section and Blade-Strut Joint Design

The influence of strut section and blade-strut joint design on C_p was found to be significant, as shown in Figure 3.11. The C_p for Turbine C was more than double that of Turbine B. This large increase in C_p was due to changes in strut section and blade-strut joint design, with all other geometry being identical for the two turbines. As shown in Figure 3.2, Turbine C has a NACA0012 section for the strut and faired joints with the blades, whereas the Turbine B struts have a machined flat bar section and small connection tabs for the blade-strut joints. The more streamlined hydrodynamic strut section of Turbine C provided lower levels of strut drag than the bluffer section used for Turbine B, resulting in reduced levels of resistive torque generated by the turbine struts. This influence can be seen in Figure 3.11 to increase as tip speed ratio increases. The mounting tabs located at the blade-strut joints used in Turbine B generated higher levels of parasitic drag when compared to the more streamlined design of Turbine C, thus contributing to the C_p reduction. Although it is difficult to isolate whether the strut section or the blade-strut joint design had the largest impact on C_p, combined their effect on turbine performance was significant.

These outcomes from the CFD study are supported by the EFD results, where significant

changes in C_p were found and attributed to strut drag and blade-strut joint changes between the two designs (Rawlings 2008). The results show that to maximise C_p the selection of strut section and blade-strut joint design is critical. If optimisation studies are performed solely on blade section, as would occur using 2D CFD models, the effects on C_p of strut section and blade-strut joint design would not be captured.

3.3.4 Influence of Strut Location

The location of the turbine struts was found to impact on C_p, with struts located at blade tips increasing the effective blade length and acting as end-plates, increasing maximum C_p by 12.4% as shown in Figure 3.11 when comparing Turbines A and C with strut locations at blade tips and quarter span respectively. Although the increase in C_p was less than that caused by strut section and blade-strut joint changes it was still considerable. This end plate effect was also found in EFD where similar C_p increases of up to 16% at 1.5 ms^{-1} were found for Turbine B using NACA shaped end plates and circular disks (Rawlings 2008, Rawlings et al. 2008).

Increases in C_p caused by increased effective blade length can be seen in the differences between the vortex structures shown in Figure 3.12. Turbine C generated vortex structures at both the blade ends and at the quarter span, whereas the location of Turbine A struts at the blade tips combined the tip and blade-strut joint vortex structures, minimising flow disturbance over the blade and thereby increasing total lift force and thus torque and C_p generated.

3.3.5 Vortex Shedding Visualisation

Comparisons of vortex shedding strength were performed at λ=1.5 and λ=2.75 for Turbine B, as shown in Figure 3.13. The influence of λ on vortex shedding as a result of the relationship between blade angles of attack and λ (Paraschivoiu 2002) can be seen. At λ=1.5, large vortices were shed from the blades, as they stalled in both the upstream and downstream turbine sections due to the high angles of attack experienced at low λ. Vortices shed from the blades traverse downstream with the water flow, impacting on the blades as they rotate, reducing blade efficiency and thus the torque generated. However, at λ=2.75 there was a marked reduction in vortex generation due to the high turbine rotational rate relative to the inflow velocity. This results in the blades fluctuating through lower angle of attack

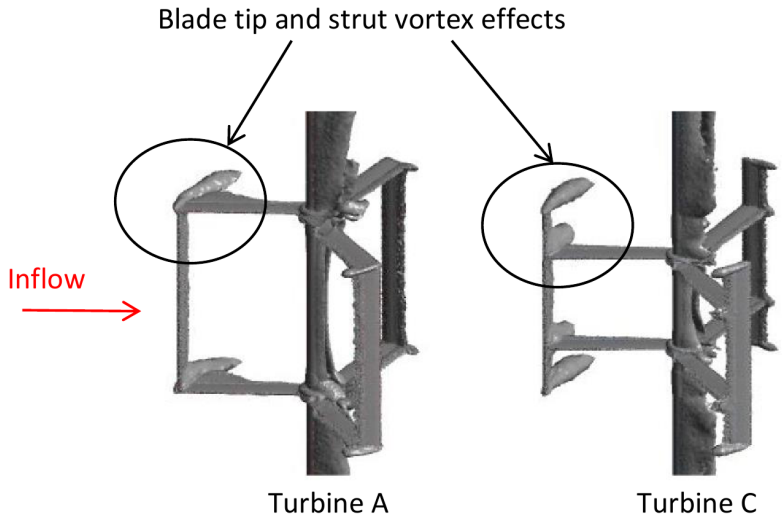

Figure 3.12: Blade tip and strut vortex structures for Turbine A and C, vorticity in stationary frame of 25 s^{-1} at an inflow velocity of 1.5 ms^{-1} and λ=2.75. Vortex strength of 25 s^{-1} chosen solely to illustrate differences between Turbines A and C

ranges (Paraschivoiu 2002), reducing flow separation and hence vortex generation, and thus increasing blade efficiency and torque generated. Shaft vortex shedding at λ=1.5 can also be seen to impact on the downstream blades, however at λ=2.75 again this effect was greatly reduced, as the increase in rotation speed of the cylindrical shaft reduces the intensity of vortex shedding (Mittal & Kumar 2003). Validation of these vortex shedding simulations was not possible as EFD results included no flow visualisation, although validation would be possible if EFD techniques such as PIV were performed.

3.3.6 Torque Ripple Simulations

The cyclic nature of the forces acting on the blades caused by the changing angles of attack resulted in fluctuations in torque generated. These time variations in torque are transmitted through the turbine drive train and can cause shaft and turbine vibrations, potentially damage turbine components (Reuter et al. 1980, Winchester & Quayle 2011). Various methods for quantifying torque fluctuations have previously been used (Li & Çalişal 2010*a*, Navabi 2008, Reuter et al. 1980, Shiono et al. 2002, Winchester & Quayle 2011); in this work torque ripple is determined as a Torque Ripple Factor (TRF), where,

$$TRF = C_{m_{Max}} - C_{m_{Min}} \tag{3.4}$$

where $C_{m_{Max}}$ and $C_{m_{Min}}$ are the maximum and minimum moment coefficients, as demon-

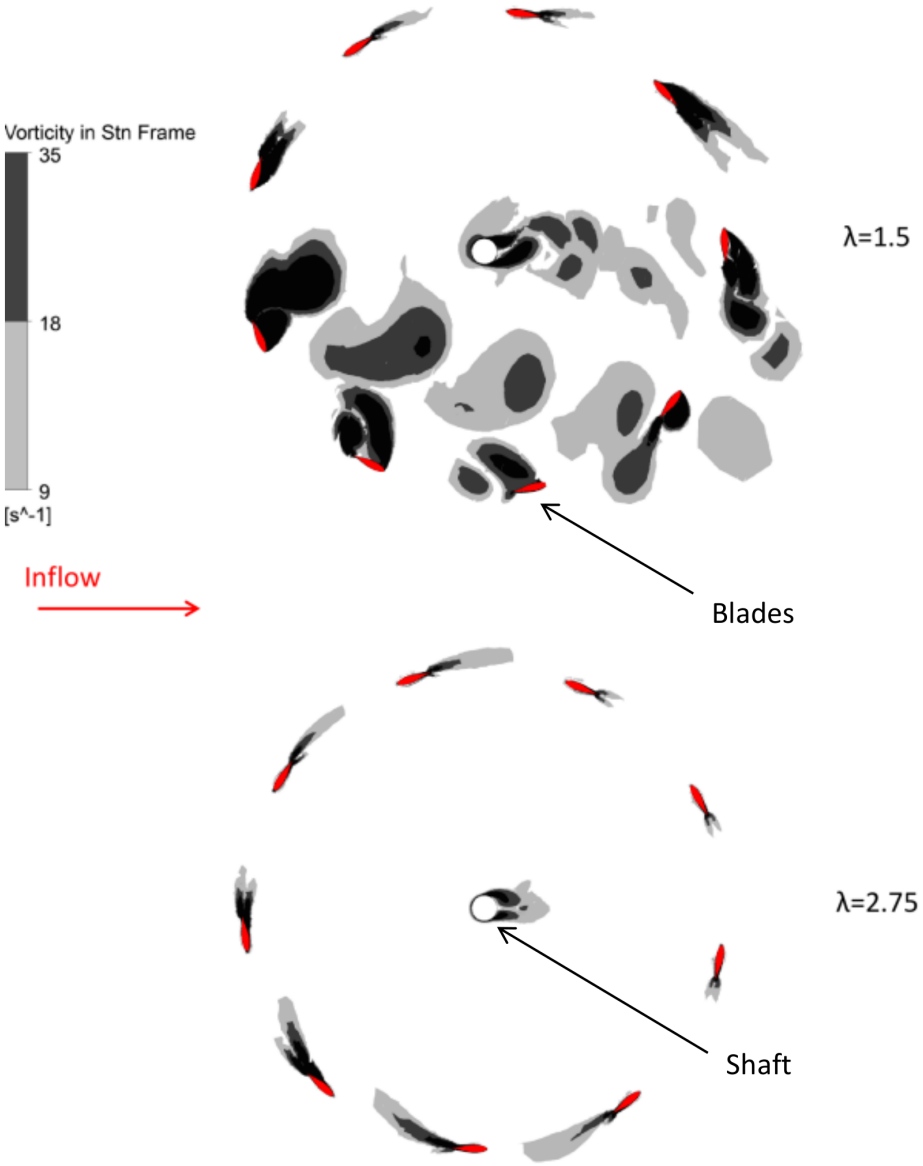

Figure 3.13: Vortex structure visualisation for Turbine B at λ=1.5 and λ=2.75 showing vortex generation. Time series of isosurfaces of vorticity in stationary frame from 9 to 35 s^{-1} at an inflow velocity of 1.5 ms^{-1} on plane 0.05m from horizontal symmetry

strated in Figure 3.14 for Turbine A at λ=2.75. This formulation allows for easy comparison of the range of torque variations experienced and is similar to that used by Winchester and Quayle (Winchester & Quayle 2011) and Shiono et al. (Shiono et al. 2002).

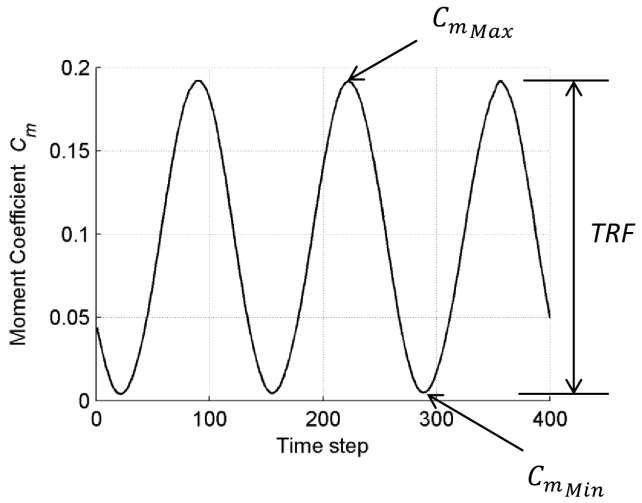

Figure 3.14: Torque Ripple Factor (TRF) determination for Turbine A at an inflow velocity of 1.5 ms^{-1} and λ=2.75

The maximum TRF for each of the three turbines occurred slightly below the λ location of maximum C_p, as shown in Figure 3.15, which for Turbines A, B, and C were located at λ=2, 2, and 2.25 respectively. This was due to the forces on the blades alternating between high positive and negative values of lift in the upstream and downstream areas of rotation due to the changing angles of attack over the blades as they rotate. Maximum TRF was found to increase with turbine efficiency, with Turbine A showing increases in TRF of 53.7% and 8.7% compared to Turbines B and C respectively, due to the increase in total lift forces. Both the location of maximum TRF and its relationship with C_p are unfortunate, as turbines designed to operate at maximum C_p will operate near maximum TRF. This can significantly shorten turbine life due to the large alternating loading forces which can cause fatigue (Reuter et al. 1980, Winchester & Quayle 2011). Reductions of TRF would be possible by using helical-bladed turbines, as the helical blade inclination angle reduces torque pulsation (Shiono et al. 2002).

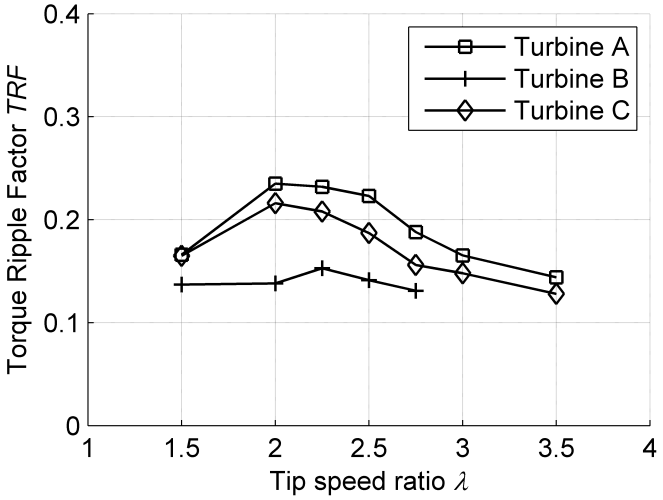

Figure 3.15: Comparison of CFD Torque Ripple Factor (TRF) for Turbines A, B, and C at an inflow velocity of 1.5 ms^{-1}

3.3.7 Turbine Mounting Force Simulations

Turbine loading forces in the inline (downstream), lateral (crosstream) and vertical (axial) direction shown in Figure 3.16 were simulated, with no force in the vertical direction found due to the horizontal symmetry of the turbine design. All forces were obtained using ANSYS CFX, which integrates the pressure and shear over the turbine surfaces. Both average and maximum forces were evaluated as the loading forces vary as the turbine rotates. The inline, lateral and maximum forces were non-dimensionalised as,

$$F_I = Inline\ Force/0.5V^2S \tag{3.5}$$

$$F_T = Lateral\ Force/0.5V^2S \tag{3.6}$$

$$F_{Max} = Maximum\ Force/0.5V^2S \tag{3.7}$$

3.3.8 Validation of Inline Forces with Experimental Fluid Dynamics

Average CFD and EFD (Rawlings 2008) inline force coefficients for Turbine B are shown in Figure 3.17. Good agreement between CFD and EFD was found across most λ, with

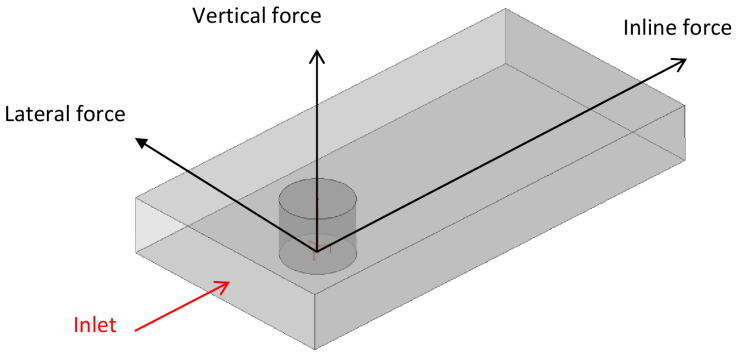

Figure 3.16: Definitions of lateral, inline and vertical forces

differences of 8.2% and 2.5% at λ=2 and 2.5 respectively. The inline force magnitude increased with λ due to increased flow velocity over the struts and hence increased strut drag. However the inline force plateaued with increasing λ, which the authors suggest was caused by reductions in cylindrical shaft drag coefficient as λ increased, as shown by EFD and CFD studies on cylindrical bodies (Elmiligui et al. 2004). This effect may also be caused by the turbine acting more like a solid body at high λ (Bachant 2011). Validation of lateral, vertical and maximum forces was not possible as EFD data was not available, however close correlation between EFD and CFD was demonstrated for inline force coefficients simulations.

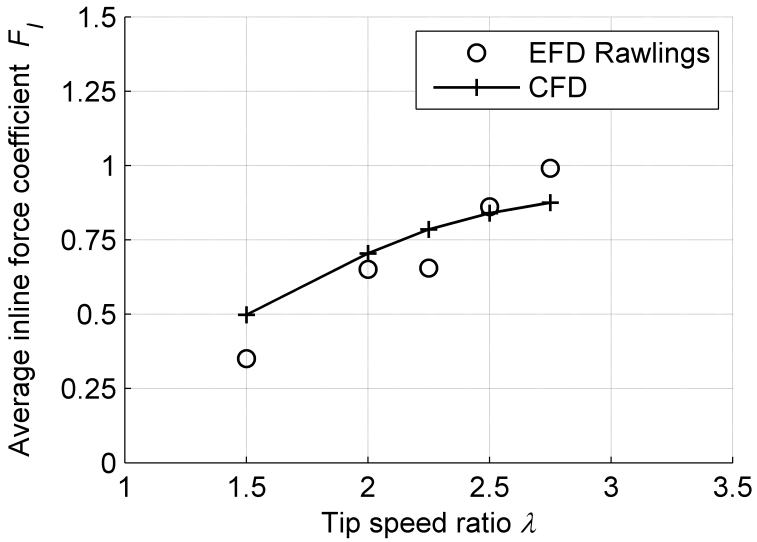

Figure 3.17: Comparison of average CFD and EFD inline force coefficients for Turbine B at an inflow velocity of 1.5 ms^{-1} (Rawlings 2008)

3.3.9 Inline and Lateral Force Simulations

Simulations of inline and lateral force coefficients for Turbines A, B, and C were obtained and are shown in Figure 3.18. Lateral forces were found to be approximately 75% lower than inline forces, and were found to remain relatively constant across the range. Inline force rose then plateaued as λ increased, due to reductions in shaft drag as rotation rates increased. Notably inline forces were not significantly influenced by strut section, blade-strut joint design or strut location, whereas the lateral forces were affected by changes in these parameters due to variations in blade efficiency and thus blade lift force between Turbines A, B and C. The maximum forces generated were found to be up to 40% higher than the average forces due to TRF, with the average loading forces slowly plateauing above λ=3 due to reductions in shaft drag and changes in blockage as λ increased. Below λ=3, maximum mounting forces at each λ increased with turbine efficiency due to lateral force increases, with variations in lift force driving the difference.

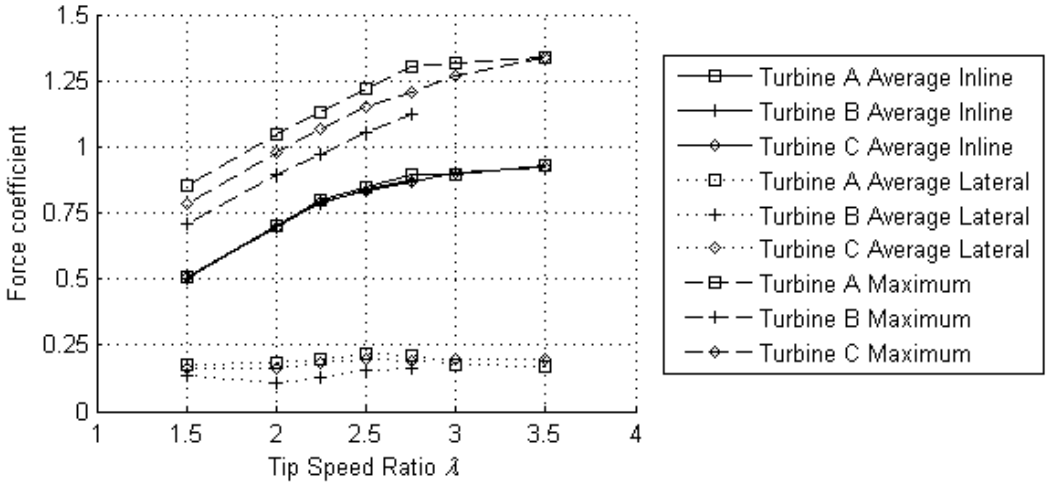

Figure 3.18: Comparisons of average inline, average lateral and maximum force coefficients for Turbines A, B, and C at an inflow velocity of 1.5 ms^{-1}

3.4 Conclusions

Three straight-bladed vertical axis tidal turbine configurations were simulated successfully by 3D CFD models using the k-ω SST turbulence model. Two turbine models were successfully validated against EFD results, with maximum power output predictions within 15% of EFD results. These results demonstrate that URANS models are an effective simulation

tool for predicting vertical axis turbine power output, and that they can accurately capture the effects of geometrical changes on power output between turbine designs.

The selection of strut section and blade-strut joint design was found to have a crucial impact on power output. Power output with low drag struts with streamlined blade-strut joints was found to be more than 50% higher than that of high drag struts with blade-strut connection tabs. The location of the strut attachment point to the blade was found to impact power output to a lesser but still significant degree, with struts located at the blade tips increasing maximum power output by 12% when compared to struts located at the quarter span.

The relationship between torque ripple and rotation rate was investigated, with maximum torque ripple occurring around the rotation rate where maximum power output was generated. As turbines are designed to operate at maximum power output they will experience large loading fluctuations, the effects of which need to be further investigated.

Investigation of mounting forces using CFD models determined new relationships between rotational rate and mounting forces. The average inline force magnitude was found to be significant, with average lateral forces exhibiting lower values. A direct relationship between turbine efficiency and inline, lateral and maximum forces was determined, with more efficient turbines exhibiting increased lateral forces while experiencing minimal changes in inline forces. Maximum forces were found to be more than 40% higher than the average forces.

This work has also shown that due to the continual increases of computing power available to CFD users, the use of full 3D CFD simulation models for vertical axis turbines is possible without the need for unrealistic computational resources or time requirements. When combined with the ability of the 3D models to capture the effects of geometrical changes on power output the optimisation of turbine design using 3D CFD models is now possible within reasonable timeframes.

The CFD simulation methods developed here will in future work be used to evaluate the performance of helical-bladed turbines to determine any differences, and thus possible advantages, between helical and straight-bladed designs.

Chapter 4

Comparisons Betwween DMS and CFD Blade Force Simulations of Straight-Bladed Vertical Axis Tidal Turbines

This chapter has been submitted for publication in the *Internation Journal of Marine Energy*, and at the time of writing is under review. The citation for the research article is:

Marsh P., Ranmuthugala, D., Penesis, I., & Thomas, G. Comparisons Betwween DMS and CFD Blade Force Simulations of Straight-Bladed Vertical Axis Tidal Turbines, [Under review, 2015].

Abstract

The forces on the blades of a one and a three-bladed vertical axis turbine were obtained using Double Multiple Streamtube (DMS) and Three-Dimensional (3D) Computational Fluid Dynamics (CFD) simulation models. The simulated blade force results were compared to Experimental Fluid Dynamics (EFD) to establish the accuracy of the numerical methods utilised. The DMS model incorporated the Gormont dynamic stall model to account for changing angles of attack on the blades due to turbine rotation, whilst the CFD model utilised the k-ω Shear Stress Transport (k-ω SST) turbulence model. For both turbine geometries the CFD model better predicted the maximum EFD forces normal to the blade chord than the DMS model, whilst the EFD tangential blade forces were accurately simulated by both numerical models. Differences were noted between the magnitudes of the force coefficients of the one and three-bladed turbines, as a result of the influence of flow blockage and wake vortex shedding effects, with the three-bladed turbine exhibiting reduced downstream normal and tangential force values when compared to the one-bladed turbine. The simulation models developed as part of this work will be used to characterise turbine blade loading using beam theory and Finite Element analysis techniques.

4.1 Introduction

To capture the kinetic energy held within oceans tidal and current flows horizontal and vertical axis turbines are proposed. Of the two, vertical axis turbines might be better suited for ocean installations as they exhibit two key advantages over horizontal axis designs: they are insensitive to inflow direction and all electrical components can be mounted above the water surface (Marsh et al. 2013). Although work has been carried out to simulate and investigate the power output of these turbines (Marsh et al. 2012, 2013), little is known of their blade loading characteristics. To ensure turbine longevity detailed understanding of blade loading must be established, either by Experimental Fluid Dynamics (EFD) or by numerical simulation using methods such as Fluid Structure Interaction (FSI) studies. These studies can use either Computational Fluid Dynamics (CFD) or momentum-based Double Multiple Streamtube (DMS) simulation models to determine the blade force magnitudes used as input for the structural analysis models. Thus, before the FSI simulations can be performed, the accuracy and efficiency of the CFD and DMS models must be established to ensure the accuracy of the FSI models.

Experimental measurements of turbine blade forces using EFD are rare, as research has predominately concentrated on maximising power output. However, during a series of experiments in the late 1970's and early 1980's, the blade forces of three vertical axis turbines that varied in blade number were measured using strain gauges (Strickland et al. 1979, Webster 1978). The blade forces were found to vary significantly with rotation angle and blade number, with dynamic stall and wake shedding effects dominant. Numerical simulations of the blade forces using vortex theory were performed, with reasonable agreement found (Strickland et al. 1979). However, for two of the three rotation rates simulated where dynamic stall effects were dominant, correlation coefficients were adjusted until results approximated EFD data. More recently, Duraisamy and Lakshminarayan (2014) modeled a 1.22m diameter one-bladed turbine using a Two-Dimensional (2D) CFD model, and compared results against EFD testing carried out in 1982. Blade normal forces were predicted accurately for the rotational rates studied when compared to EFD results. However, tangential force prediction accuracy was reduced, with the peaks in tangential force over predicted. The varying accuracy of the blade force predictions was ascribed to the assumption of two-dimensionality. Simulations for more than one blade, which would display a greater influence of the wake effects, were not performed.

In this current study, numerical simulations were performed to obtain the blade forces on one and three-bladed vertical axis turbines using DMS and Three-Dimensional (3D) CFD models. Comparisons between numerical simulation results and EFD data obtained from literature (Strickland et al. 1979, Webster 1978) were performed to examine the accuracy of the simulation methods utilised, and thus determine any possible advantages between the two numerical approaches. Examination of the influence of the number of blades on force predictions due to wake effects was also performed.

4.2 Numerical Simulation

Simulations using momentum-based DMS models were performed using code scripted in Matlab, with the method used based on the method developed by Paraschivoiu (Marsh et al. 2013, Paraschivoiu 2002). Numerical 3D CFD simulations were performed using the ANSYS CFX software package (ANSYS 2010*a*), which solved the transient Unsteady Reynolds Averaged Navier-Stokes (URANS) equations using an element-based finite volume approach. The water density in all simulations was set to 1000 kg/m^3.

4.2.1 Turbine Geometry

The geometrical details of the two straight-bladed vertical axis turbine models simulated are shown in Figure 4.1 and Table 4.1. The turbines differing only in blade number as shown in Table 4.1. Numerical simulations using DMS and CFD models were used to determine the normal and tangential forces on the blades relative to the blade chord, as shown in Figure 4.1, which were non-dimensionalised by the freestream dynamic pressure and the blade chord as F_n and F_t respectively. The struts that supported the blades of the EFD turbine above the freesurface were not modelled. This assumption was possible as the struts would not generate significant levels of resitive torque as they rotated in air, allowing the simplifciation of the numerical computational domain used.

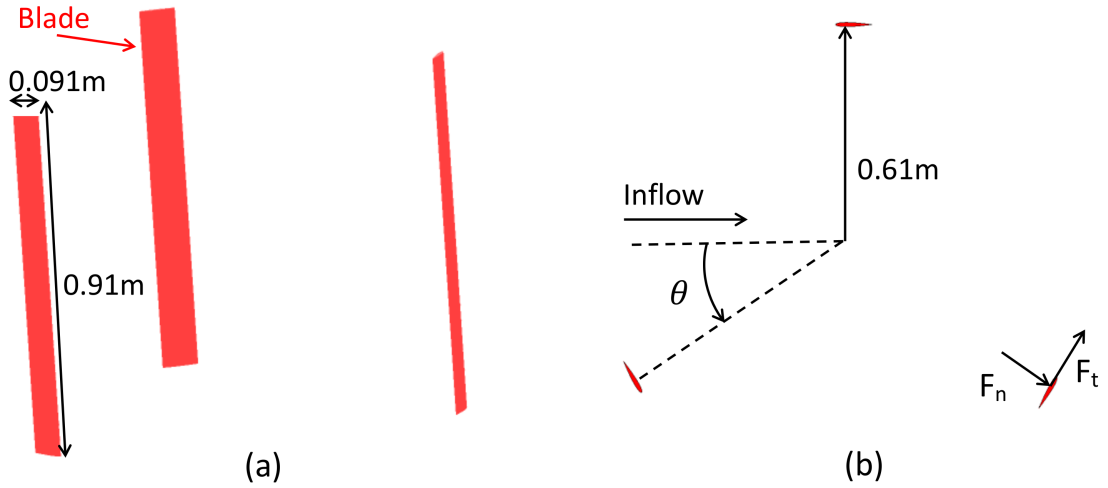

Figure 4.1: Three-bladed turbine (a) geometrical details and (b) force nomenclature showing normal (F_n) and tangential (F_t) force coefficient definitions. Dimensions in m (Strickland et al. 1979, Webster 1978)

Table 4.1: Turbine Geometry for CFD and EFD Models (Webster 1978)

Geometry	Dimensions
Number of blades	1 and 3
Blade section	NACA0012
Blade chord	0.091m
Diameter	1.22m
Turbine span	0.91m

4.2.2 Double Multiple Streamtube Model

A momentum based mathematical model using the DMS method (Marsh et al. 2013, Paraschivoiu 2002) was developed to determine F_n and F_t, with the influence of dynamic stall incorporated through the use of the Gormont method (Masson et al. 1998). The DMS method models the turbine using a double actuator disk method to account for reductions in flow velocity through the streamtube. Using iteration methods the upstream and downstream induction factors were calculated, from which blade angles of attack can be determined. From the blade angle of attack the blade forces were determined using NACA0012 lift and drag data obtained at a Reynolds number of 50,000, approximating the Reynolds number of the blade due to the rotation of the turbine. This lift and drag data was generated using the viscous airfoil analysis tool Xfoil (Drela 1989).

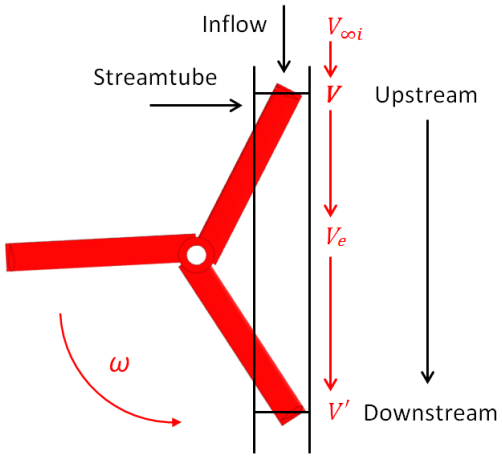

Figure 4.2: DMS Streamtube Model showing an example of the streamtube method for calculation of upstream and downstream flow values $V_{\infty i}$, V, V_e and V through one streamtube

The DMS model simulated the performance of a vertical axis turbine by modeling the reduction in flow velocity using two actuator disks. Using the interference factor u, the upstream velocity $V_{\infty i}$ shown in Figure 4.2 is reduced as it passed through the actuator disk, and the local velocity V shown in Figure 4.2 is given by,

$$V = uV_{\infty i} \tag{4.1}$$

The equilibrium velocity V_e shown in Figure 4.2 is determined as,

$$V_e = (2u - 1)V_{\infty i} \tag{4.2}$$

The downstream induced velocity V' shown in Figure 4.2 is determined using V_e as,

$$V' = u'(2u - 1)V_{\infty i} \tag{4.3}$$

where u' is the second interference factor for the downstream actuator disk. For the upstream and downstream turbine sections, the local relative velocity W and the angle of attack θ are determined geometrically using,

$$W^2 = V^2[(\lambda - \sin\theta)^2 + cos^2\theta] \tag{4.4}$$

and

$$\alpha = sin^{-1}\left(\frac{cos\theta}{\sqrt{(\theta - \sin\theta)^2 + \cos^2\theta}}\right) \tag{4.5}$$

where θ is the azimuth angle.

The upstream function f_{up} was determined as:

$$f_{up} = \frac{Nc}{8\pi r}\int_{\frac{-\pi}{2}}^{\frac{\pi}{2}}\left(C_n\frac{\cos\theta}{|\cos\theta|} - C_t\frac{\sin\theta}{|\cos\theta|}\left(\frac{W}{V}\right)^2 d\theta\right) \tag{4.6}$$

where N is the number of blades, c is the blade chord, and C_n and C_t, the normal and tangential force coefficients, were respectively defined as:

$$C_n = C_l\cos\alpha + C_d\sin\alpha \tag{4.7}$$

and

$$C_t = C_l\sin\alpha - C_d\cos\alpha \tag{4.8}$$

Values of C_l and C_d were determined using lift and drag tables at the local blade Reynolds number R_e where:

$$R_e = \frac{r\omega c}{\nu} \tag{4.9}$$

with ν being the kinematic viscosity of water.

The DMS model splits the turbine into streamtubes for each azimuth angle θ, which are further divided into upstream and downstream sections as shown in Figure 4.2. Solutions

for the upstream sections are calculated first for each azimuth section by iteration, using the method outlined in Figure 4.2. Once the upstream solutions are obtained, the iteration process is repeated for each downstream azimuth section, using V_e determined from Equation 4.2 and u found from the upstream solution as input for the downstream iteration process. During this iteration process updated values of u are found using,

$$u_{new} = \frac{\pi}{f_{up} - \pi} \tag{4.10}$$

where f_{up} is calculated using Equation 4.6.

Once completed the upstream turbine blade torque $T_{up}(\theta)$ is determined over the span H of the blades where:

$$T_{up}(\theta) = 0.5\rho c r H C_t W^2 \tag{4.11}$$

The average upstream half cycle torque coefficient $\overline{T_{up}}$ is calculated as

$$\overline{T_{up}} = \frac{N}{2\pi} \int_{\frac{-\pi}{2}}^{\frac{\pi}{2}} \left(\overline{T_{up}(\theta)} d\theta \right) \tag{4.12}$$

Thus, the upstream half-cycle torque coefficient $\overline{C_{Q_1}}$ and upstream power coefficient C_{p_1} are calculated as:

$$\overline{C_{Q_1}} = \frac{\overline{T_{up}}}{0.5\rho V_{\infty i}^2 S r} \tag{4.13}$$

and

$$C_p = C_{Q_1} \lambda \tag{4.14}$$

This method is repeated for the downwind section to find the downstream C_{p_2}, and thus the total turbine power coefficient C_p is calculated as:

$$C_p = C_{p_1} + C_{p_2} \tag{4.15}$$

The DMS model estimates the blade dynamic characteristics from static coefficient data tables to capture the effect of the rapidly changing angles of attack on the turbine blades as

they rotate (Paraschivoiu 2002). For all simulations the dynamic stall correlation coefficients were not modified, so as to evaluate the accuracy of the DMS model without any post-priori correlation modifications using EFD results. The Gormont model simulates dynamic stall by defining a reference angle of attack where the 2D coefficient data is considered (Masson et al. 1998), given by,

$$\alpha_{ref} = \alpha - K_1 \delta\alpha \tag{4.16}$$

where;

$$K_1 = \begin{cases} 1 \text{ if } \dot{\alpha} \geq 0 \\ -0.5 \text{ if } \dot{\alpha} < 0 \end{cases} \tag{4.17}$$

and

$$\delta\alpha = \begin{cases} \gamma_1 S \text{ when } S \leq S_c \\ \gamma_1 S_c + \gamma_2 (S - S_c) \text{ when } S > S_c \end{cases} \tag{4.18}$$

and

$$S = sqrt \frac{c\dot{\alpha}}{2W} \tag{4.19}$$

and

$$S_c = 0.06 + 1.5(0.06 - (t/c)) \tag{4.20}$$

$$\gamma_1 = \begin{cases} \gamma_2/2 \text{ for lift} \\ 0 \text{ for drag} \end{cases} \tag{4.21}$$

where

$$\gamma_2 = \gamma_{mx} \max\left(0, \min\left[1, \frac{M - M_2}{M_1 - M_2}\right]\right) \tag{4.22}$$

where M is the Mach number, $\dot{\alpha}$ is the time derivative of α, and t/c is the relative thickness of the turbine blade section. The values for the Gormont coefficients M_1,M_2 and γ_{mx} are given in Table 4.2.

Using this model the dynamic lift and drag coefficients are determined by,

Table 4.2: Determination of Gormont Coefficients M_1, M_2, and γ_{mx}

Lift Characteristic	Drag Characteristic	
M_1	0.4 + 5.0 (0.06 (t/c))	0.2
M_2	0.9 + 2.5 (0.06 (t/c))	0.7 + 2.5 (0.06 (t/c))
γ_{mx}	1.4 6.0 (0.06 (t/c))	1.0 - 2.5 (0.06 (t/c))

$$C_L^{Dyn} = C_l(\alpha_0) + m(\alpha - \alpha_0) \tag{4.23}$$

and

$$C_D^{Dyn} = C_D(\alpha_{ref}) \tag{4.24}$$

where

$$m = min\left[\frac{C_L(\alpha_{ref} - C_L(\alpha_0))}{\alpha_{ref} - \alpha_0}, \frac{C_L(\alpha_{SS}) - C_L(\alpha_0)}{\alpha_{SS} - \alpha_0}\right] \tag{4.25}$$

where α_0 is the zero lift angle of attack, and α_{SS} is the static stall angle of attack. A flow chart of the DMS model is shown in Figure 4.3, where the iteration process for each streamtube and the dynamic stall coefficient corrections are shown.

4.2.3 Computational Fluid Dynamics Models

The blade forces of the one and three-bladed turbines were simulated using two 3D CFD models that were meshed using ANSYS CFX 13.0 using unstructured tetrahedral elements (ANSYS 2010*a*). These models included all blades and were geometrically equivalent to the EFD turbines to allow validation of the numerical simulation approaches utilized against the published experimental results (Strickland et al. 1979, Webster 1978). The density of the mesh was varied according to expected flow curvature rates with increased density in regions near the wake and blade regions. Alternatively, mesh density was reduced away from the turbine surfaces to minimise computational effort, such as near the computational domain boundaries. The boundary layers near the turbine surfaces were fully resolved using 30 layers, with the total boundary layer thickness estimated using turbulent boundary layer theory (Marsh et al. 2015*a*,*b*). This estimated thickness was doubled to ensure that the boundary layer was contained within the prescribed inflation layer region. Inflation layer mesh growth rates were limited to 1.2 as recommended (ANSYS 2010*a*). Due to the proximity of the tips of the blades to the bottom tank wall, mesh refinement was also performed in this region.

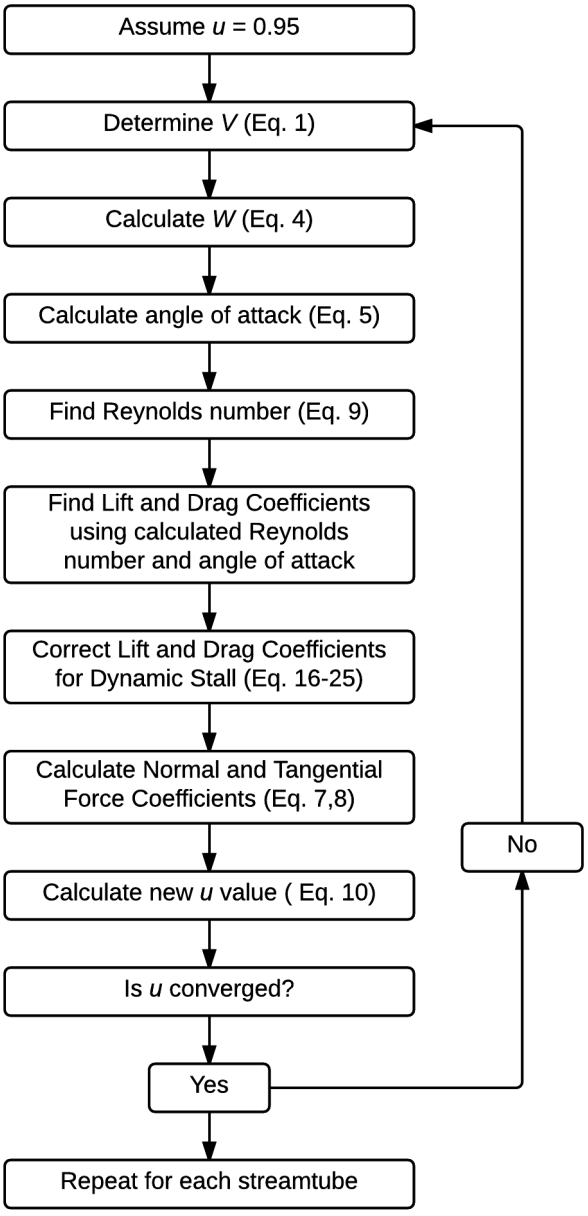

Figure 4.3: Flowchart of DMS iteration process

Turbine rotation was simulated by enclosing the turbine in an inner domain as shown in Figure 4.4. This domain was rotated at 0.746 rads^{-1} ($\lambda = 5$) corresponding to the EFD rotational rate (Strickland et al. 1979, Webster 1978) using the CFX transient rotor-stator model (ANSYS 2010*a*). This model uses a General Grid Interface (GGI) to interpolate flow values across the interface due to non-conformal mesh. To minimise any errors in the intersection algorithm, the GGI was placed at 1.5 times the turbine diameter measured from the rotational axis (Marsh et al. 2013).

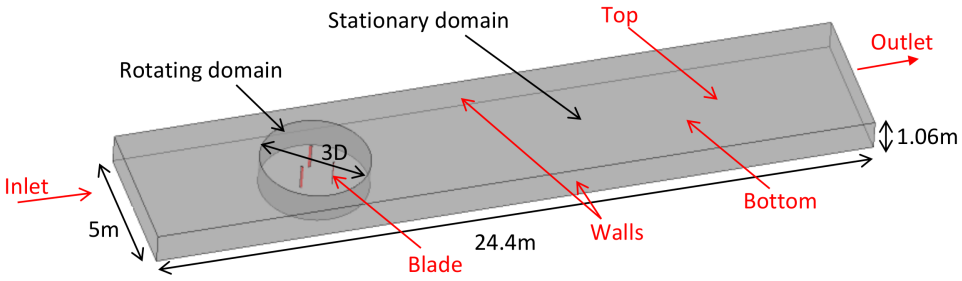

Figure 4.4: Domain boundary nomenclature and sizing. Dimensions in meters (m) and turbine diameters (D)

The CFD domain dimensions are shown in Figure 4.4, with the associated boundary conditions outlined in Table 4.3. The width and depth of the computational domain were set to that of the EFD towing tank to account for any blockage effects. However, the domain length was determined by doubling the domain length until variations in F_n and F_t reduced to less than 5% between successive length refinements, thus allowing full wake development. Simulations were performed to investigate the influence of domain size and boundary conditions on blade loading parameters. Results indicated that free slip walls could be used instead of no slip walls on the domain sidewalls, reducing the wall mesh density and thus increasing computational efficiency. To reduce computational effort the waters surface was modeled using a free slip wall, which simulated the surface pressure effects whilst simplifying computational requirements when compared to a full multiphase approach. Examination of simulation results against EFD from literature was performed to ensure the validity of this free surface modeling assumption. The bottom tank wall modeled using a no slip boundary condition to capture any boundary layer effects due to the proximity of the blades to the bottom wall.

The $k-\omega$ SST turbulence model was utilised due to its ability to accurately model both the free stream and boundary layer regions, as well as offering improved prediction of flow

Table 4.3: Domain Boundary Conditions for the CFD model (Strickland et al. 1979, Webster 1978)

Boundary	Condition
Inlet	Uniform flow: 0.091 ms^{-1}
Outlet	Relative pressure: 0 Pa
Walls	Free slip walls
Blade	No slip walls
Bottom	No slip wall
Top	Free slip wall

separation and adverse pressure gradients by the inclusion of transport effects into the formulation of the eddy-viscosity (ANSYS 2010*a*). This model has also demonstrated high simulation accuracy for turbine power output simulations when compared against EFD results (Dai & Lam 2009, Lain & Osorio 2010, Marsh et al. 2012, 2013, 2015*a*,*b*, Nobile et al. 2011). The fluid was modeled as incompressible as all flow velocities were significantly less than Mach 0.3. Fluid flow was assumed to be fully turbulent, with no laminar-to-turbulent transitional effects considered to simplify computational effort. High order advection and second order backward Euler transient terms were used to ensure numerical accuracy, as previous simulations of vertical axis turbines found that low order schemes were unable to accurately resolve turbine performance parameters (Marsh et al. 2015*a*). An inlet turbulence setting of 5% was applied as no measurements of turbulence intensity were performed during EFD testing (Strickland et al. 1979, Webster 1978). Convergence was achieved when solution residuals reduced to below 10^{-4} and reduced by more than three orders of magnitude, similar to previous works (Marsh et al. 2015*a*,*b*). To minimise convergence times and hence solution time, all simulations were started from previous solutions, thus reducing overall computational requirements.

Mesh Independence Studies

Systematic independence studies were performed for the one and three-bladed turbine simulation models to ensure spatial, temporal, domain length, and boundary layer mesh independence, similar to that performed previously (Marsh et al. 2012, 2013, 2015*a*,*b*). Independence was achieved when doubling of these factors resulted in variations in F_n and F_t trending to less than 5% between successive refinements, with an example of the trends shown in Figure 4.5. Mesh element count independence was determined for F_n and F_t at 7.4 x 10^6 and 14.2 x 10^6 mesh elements for the one bladed and three-bladed turbines respectively. The values for F_t were highly influenced by mesh element count, as drag predictions are highly dependent upon the mesh density in the chordwise direction and on the leading edges of the blades.

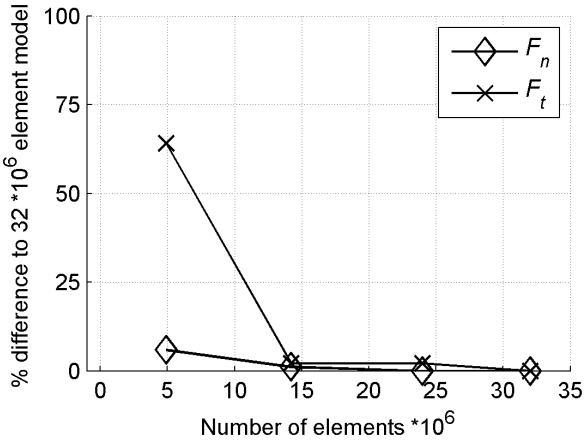

Figure 4.5: Mesh element count independence for three-bladed turbine at a rotational rate of 0.746 rads^{-1} and an inflow velocity of 0.091 ms^{-1}

Time step studies were performed for the one and three-bladed turbine models to ensure temporal independence, critical due to the highly transient nature of the flow. Temporal independence was demonstrated at 0.9° of rotation per iteration step for F_n and F_t for both turbine models, with an example shown in Figure 4.6 for the three-bladed turbine. Again the values for F_t were highly influenced by mesh element count, as drag predictions are highly dependent upon the mesh density in the chordwise direction and on the leading edges. The time step size was low due to the high mesh density of the fully-resolved boundary layers.

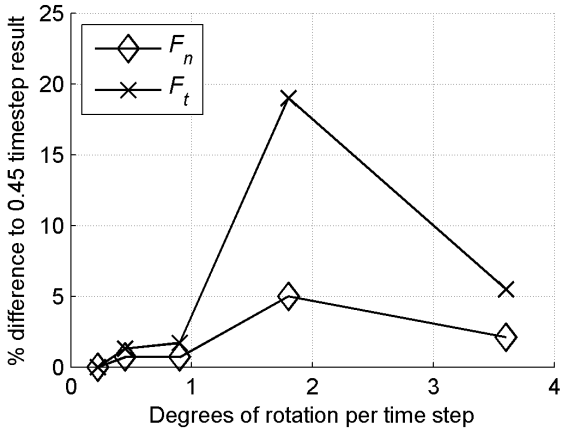

Figure 4.6: Time independence for the three-bladed turbine at a rotational rate of 0.746 rads^{-1} and an inflow velocity of 0.091 ms^{-1}

Additional independence studies were performed for domain length and boundary layer mesh density. Domain length independence was determined at 24.4m for both turbine models, which allowed for full wake development. Given that the EFD tank length was limited, EFD force data was obtained on the fourth revolution of the turbine to minimise any startup transient effects. Comparisons of CFD results with EFD were performed to determine whether modeling the full wake replicated the blade forces with sufficient accuracy when compared to EFD results. For both turbine models boundary layer mesh density independence was evaluated by examining the influence on F_n and F_t of the average height of the first cell from the turbine walls, known as the non-dimensional variable $y+$ (Paraschivoiu 2002). Independence was demonstrated at an average $y+$=0.1 using methods similar to those outlined in (Marsh et al. 2015*a*,*b*).

4.3 Results

Validation of the DMS and CFD numerical models was performed against EFD results available in literature of the testing of a one and three-bladed turbine conducted in a 10m long, 5m wide and 1.25m deep towing tank (Strickland et al. 1979, Webster 1978). During these experiments the blade rotation angle was measured using a transducer, with normal and tangential forces measured using strain gauges mounted on one of the turbine blades. Measurements of all forces were performed during the fourth turbine revolution to minimise the effect of any start-up transient results (Strickland et al. 1979, Webster 1978).

Comparisons of the DMS and CFD predictions with EFD for F_n and F_t for the one-bladed turbine are shown in Figure 4.7. The DMS and CFD models were able to model the variations in EFD blade forces for most rotational angles, with simulations revealing that F_n was approximately 10 times than of F_t due to the high lift to drag ratio of the blade sections used and dynamic stall effects (Paraschivoiu 2002). The blade loading was not symmetrical between the upstream (-90° to 90°) and downstream (90° to 270°) regions, as a result of the reduction in flow velocity through the turbine. Peaks in both F_n and F_t were found located between -45° and 0°, corresponding to the rotational location of maximum lift and dynamic stall. The CFD model predicted the peak F_n to within 9.0% of EFD (Strickland et al. 1979, Webster 1978); however the DMS model results were within 36.8%. During EFD severe dynamic stall effects were noted, as the ratio of blade chord to radius was high. This lead to high levels of dynamic stall that the Gormont model was unable to capture. Improvements in modeling F_n peaks using the DMS model may be possible using more

advanced dynamic stall modeling techniques such as the Beddoes-Leishman model (Masson et al. 1998), however this would reduce the model's simplicity.

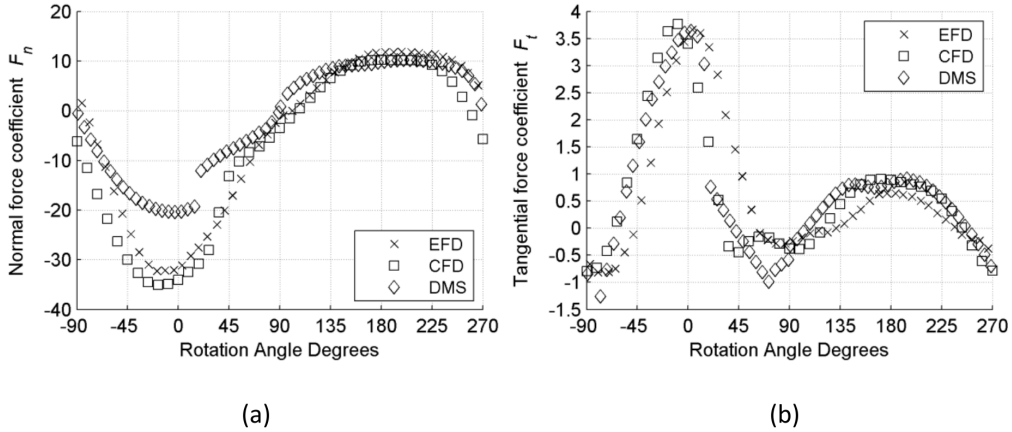

Figure 4.7: Normal (a) and tangential (b) force coefficients for the one-bladed turbine compared to EFD results (Strickland et al. 1979, Webster 1978) at a rotational rate of 0.746 rads^{-1} and an inflow velocity of 0.091 ms^{-1}

Close agreement between the CFD and DMS simulations with EFD F_t was found as shown in Figure 4.7. The DMS and CFD model replicated the EFD F_t peaks to within 0.6% and 3.8% respectively (Strickland et al. 1979, Webster 1978). In the downstream region F_t was predicted with similar accuracy by both models. The close agreement was due to the simulation of the reduction in flow velocity as the flow passes through the turbine. This reduction is modeled directly by the CFD model as vortex shedding and blockage effects, and by the DMS model using induction factors.

Comparisons of CFD and EFD predictions of F_n and F_t with EFD results for the three-bladed turbine are shown in Figure 4.8. Maximum F_n was predicted by the CFD model to within 10.1% of EFD, as the CFD model was able to capture the F_n peak caused by dynamic stall. Similar to that found for the one-bladed turbine DMS simulations, the F_n prediction accuracy of the DMS model was reduced when compared to EFD from literature (Strickland et al. 1979, Webster 1978). This reduction was ascribed to the high levels of dynamic stall, which the DMS model was unable to simulate. In the downstream region, the DMS and CFD F_n prediction results were similar, with large reductions in F_n magnitudes when compared to the upstream peaks. These reductions in force resulted as the flow velocity was reduced as it passed though the turbine. Similar to that found for the one-bladed turbine F_t prediction, the shape of the F_t-rotation angle curves and F_t peaks were predicted accurately by both the CFD and DMS models, with results within 3.2% and 2.4% of EFD respectively.

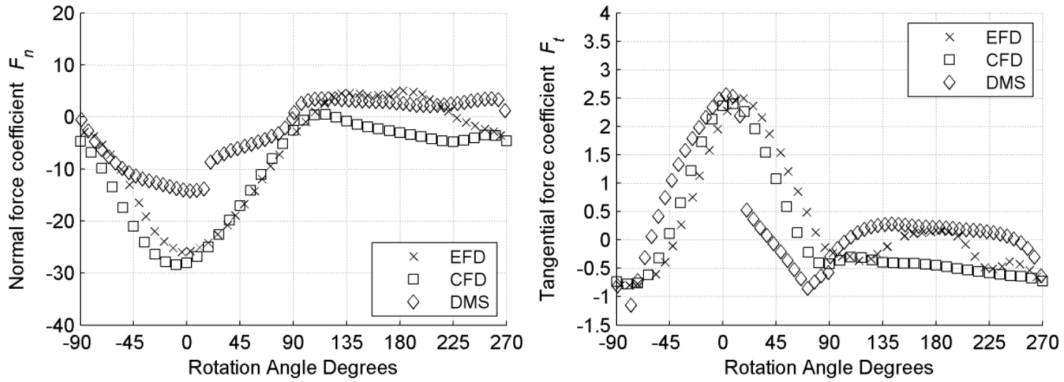

(a) (b)

Figure 4.8: Normal (a) and tangential (b) force coefficients for the three-bladed turbine compared to EFD results (Strickland et al. 1979, Webster 1978) at a rotational rate of 0.746 rads^{-1} and an inflow velocity of 0.091 ms^{-1}

Two key assumptions were made to simplify the CFD model; namely that the wake was fully developed, and that the free surface could be modeled as a free slip wall. The influence of these assumptions can be evaluated by comparing the CFD results against EFD as shown in Figures 4.7 and 4.8. The close agreement of the CFD F_n and F_t predictions with EFD from literature indicates that these assumptions are valid. Due to the low rotational and inflow velocities, the turbine would generate minimum wake disturbances and hence wave making, allowing the use of a free slip wall to model the water's surface. Additionally, modeling the full turbine wake did not reduce simulation accuracy when compared to EFD results from literature, again due to the low rotational and inflow velocities (Strickland et al. 1979, Webster 1978). Simulations that model turbine startup are computationally demanding, and would require the modeling of additional variables such as turbine moment of inertia and gearbox design that were not specified in the literature (Strickland et al. 1979, Webster 1978). Given the accuracy of the CFD model found in this work, modeling of the turbine startup process is not required for accurate replication of EFD forces for the example simulated here.

4.3.1 Flow Visualisation

The wake of the blades generates turbulent flow, which can be visualized as vorticity as shown in Figure 4.9 for the one and three-bladed turbines respectively. Unlike the one-bladed turbine blade, the blades of the three-bladed turbine shown traversed through the disturbed wake of the preceding blades. The influence of blade wake on blade forces can be

seen when comparing Figures 4.7 and 4.8, where the increase in blade number has reduced the downstream F_n by more than half. The increase in flow turbulence not only reduces downstream values, but also upstream force coefficients, due to flow reductions caused by the increased blockage generated by the additional blades. The accuracy of both numerical methods is due in part to the capture of the reduction in flow velocity through the turbine. This reduction is simulated by the DMS model using the double actuator disk method and by the CFD model by the direct simulation of vortex shedding and blockage effects.

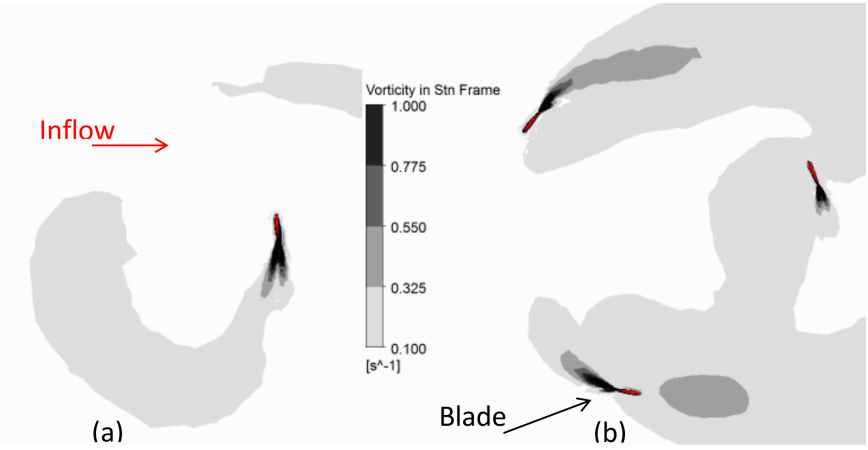

Figure 4.9: Vortex shedding comparisons between (a) one and (b) three-bladed turbines at a rotational rate of 0.746 rads^{-1} and an inflow velocity of 0.091 ms^{-1}

The use of 3D CFD models has resolved the tip vortices shed by the blade as they rotate, as shown in Figure 4.10. Large tip vortices were shed from the bottom of the blade, which slowly traversed downstream. Two-dimensional CFD models would be unable to replicate these tip vortices due the geometrical layout of vertical axis turbines, resulting in reduced simulation accuracy when compared to 3D CFD models (Marsh et al. 2012, 2013, 2015*a*,*b*). Near the top wall no tip vortices were shed from the blade as shown in Figure 4.10, as the flow was constrained by the free slip boundary wall. This simplification of the free surface reduced computational requirements without significantly reducing force simulation accuracy as shown in Figures 4.7 and 4.8.

4.3.2 Computational Requirements

All simulations were performed on a distributed cluster comprising of Intel i7 860 2.8 GHz based machines with 2GB memory per core. The DMS model took less than 1 minute on 1 core for the one and three-bladed turbines, whereas the CFD model took 20 hours on 32

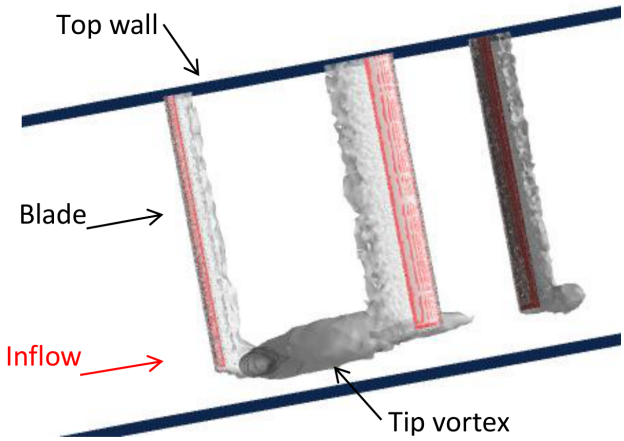

Figure 4.10: Influence of boundary walls on tip vortex generation of three-bladed turbine at a rotational rate of 0.746 rads^{-1} and an inflow velocity of 0.091 ms^{-1}. Isosurfaces of vorticity of 0.5 s^{-1}

cores for the one-bladed turbine and 26 hours on 32 cores for the three-bladed turbine. The DMS model was found to be highly computationally efficient when compared to the CFD model, making it ideal for initial design studies.

4.4 Conclusions

The blade loading of two experimental vertical axis turbines was simulated using DMS and CFD models. Blade force prediction for the turbines aligned with the experimental results with differing accuracy, dependent on whether normal or tangential blade forces were examined. The CFD model resulted in the closest replication of EFD normal force measurements, with the normal force peaks accurately simulated. The DMS model normal force prediction accuracy was reduced when compared to the CFD and EFD results, as the DMS model was unable to accurately capture the peaks in normal blade forces caused by dynamic stall. However, both the CFD and DMS models were able to accurately simulate tangential blade forces. The influence of the blade wake was also captured by the DMS and CFD models, with increasing blade number shown to reduce blade force values.

Future work is planned using both the DMS and CFD models to evaluate turbine blade loading to gain further knowledge of operational turbine characteristics. Using these models as input for FSI models, evaluations of blade stress and deformation levels will be performed using beam theory and Finite Element Analysis techniques.

Chapter 5

Numerical Simulation of Straight-Bladed Vertical Axis Tidal Turbines

This conference paper was presented at the 2nd Annual Asian Wave and Tidal Energy Conference in Toyko, Japan. The citation for this journal paper is:

Marsh P., Ranmuthugala, D., Penesis, I., & Thomas, G., Numerical Simulation of Straight-Bladed Vertical Axis Tidal Turbines, *2nd Annual Asian Wave and Tidal Energy Conference*, Tokyo, Japan, 2014.

Chapter 6

Numerical Investigation of the Influence of Blade Helicity on the Performance Characteristics of Vertical Axis Tidal Turbines

This refereed journal paper was published in *Renewable Energy*. The citation for this journal paper is:

Marsh P., Ranmuthugala, D., Penesis, I., & Thomas, G. Numerical Investigation of the Influence of Blade Helicity on the Performance Characteristics of Vertical Axis Tidal Turbines, *Renewable Energy*, 81 (2015), pp.926-935.

Abstract

Previous research has shown that helical vertical axis turbines exhibit lower torque fluctuation levels than straight-bladed turbines; however little is known of the impact of blade helicity on turbine performance characteristics. To investigate these relationships the hydrodynamic characteristics of straight and helical-bladed vertical axis turbines were investigated using Three-Dimensional (3D) Computational Fluid Dynamics (CFD) models using a commercial Unsteady Reynolds Averaged Navier-Stokes (URANS) solver. Simulations of power output, torque oscillations, and mounting forces were performed for turbines with overlap angles from 0° to 120° and section inclination angles from -15° to 45°. Results indicated that straight-bladed turbines with 0° blade overlap generated the highest power output. Helical turbines were found to generate decreasing power outputs as blade overlap angle increased due to the resultant blade inclination to the inflow. Blade section inclination to the inflow was also found to influence power output. Some benefits of helical-bladed turbines over their straight-bladed counterparts were established; helical turbine torque oscillation levels and mounting forces were reduced when compared to straight-bladed turbines. For both straight and helical-bladed turbines maximum mounting force levels were found to exceed the average force levels by more than 40%, with large cyclical loading forces identified.

6.1 Introduction

Straight-bladed vertical axis turbines, as proposed for tidal power generation, experience significant torque oscillations as a result of changing angles of attack on the blades as they rotate (Malipeddi & Chatterjee 2012, Paraschivoiu 2002, Winchester & Quayle 2011). These oscillations generate alternating loading forces on the turbine structure that can lead to premature failure through fatigue if not adequately accounted for (Gorlov 1998, Scheurich et al. 2011). Research using Experimental Fluid Dynamics (EFD) has demonstrated that the use of helical bladed turbines can reduce torque oscillation levels (Gorlov 1998, Niblick 2012, Shiono et al. 2002), as the flow does not concurrently stall along the full blade length due to the blade distribution around the rotational axis (Kirke 2011). However helical blade overlap, ϕ, shown in Figure 6.1, may influence power generation due to the inclination of the helical blades to the inflow. To investigate any relationships between these factors two approaches can be utilised: EFD or numerical simulation using methods such as Computational Fluid Dynamics (CFD).

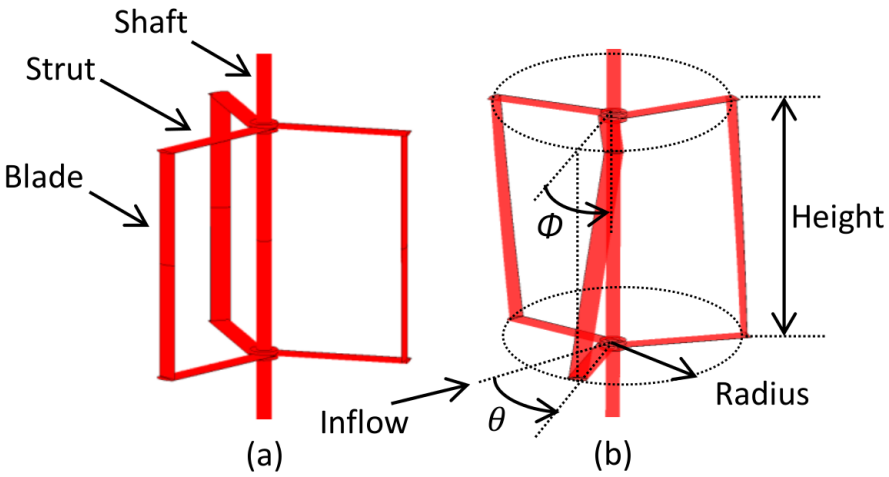

Figure 6.1: Straight (a) and helical (b) bladed vertical axis turbines, including the definition of the helical blade overlap angle, ϕ

Although EFD testing results concur that helical-bladed turbines exhibit reduced torque oscillation levels (Gorlov 1998, Niblick 2012, Shiono et al. 2002), there is general disagreement about the effects of helicity on power output. Shiono et al. (Shiono et al. 2002) tested a series of straight and helical-bladed turbines with NACA633018 blade sections of the same overlap angle but differing turbine spans. They demonstrated that helicity decreased power output, and concluded that it was more appropriate to use straight rather than helical-bladed turbines to maximise power output. Niblick (Niblick 2012) performed EFD testing on two helical turbines with three and four NACA0018 blades of differing helicity. Results indicated that power output reduced as helicity increased, as the helicity reduced total lift and hence torque. However, Gorlov (Gorlov 2002) compared the power outputs of a straight and 60° helical-bladed turbine of the same radius and height, determining that the helical turbine demonstrated increased power output over the straight-bladed design, in excess of 50% at some rotational rates. Gorlov also noted improvements of up to 95% greater power and 50% higher speed in comparison with a straight-bladed turbine of identical overall dimensions during EFD testing of 20 small 0.09 m diameter models (Gorlov 1998). The reasons that Gorlov found power output to increase with blade overlap yet Shiono et al. and Niblick found power output to decrease are unknown, and were a key driver for this research.

Numerical CFD studies of helical vertical axis turbines are limited as Two-Dimensional (2D) models cannot be utilised due to the curved blade geometry, resulting in computationally demanding simulations due to the resultant large mesh element counts associated with Three-

Dimensional (3D) simulations. Castelli and Benini (Castelli & Benini 2012) performed 3D CFD studies on a series of 1.03 m span single blades with overlap angles of 0°, 30°, 60°, 90° and 120°. Using the Unsteady Reynolds-Averaged Navier-Stokes (URANS) equations and the k-ω Shear Stress Transport (k-ω SST) turbulence model they found that power output reduced as blade overlap angle increased. Hall (Hall 2012) simulated the power output of two single and four bladed helical turbines and compared results with EFD (Niblick 2012) using the URANS k-ω SST turbulence model. Power output was obtained at three rotational rates but was found to over predict the measured results by more than 30%. This simulation error was prescribed to the poor modelling of dynamic stall over the blades by the k-ω SST turbulence model. Studies of the effects of helicity on power output are limited with no comprehensive examinations found in literature.

The influence of blade helicity on power output, torque oscillations, and mounting loading forces were predicted using time-accurate 3D CFD models to allow the establishment of relationships between turbine blade shape and performance characteristics. To ensure numerical simulation accuracy, validation studies were performed on three turbine models to ensure that the CFD models accurately captured the influence of blade geometry on turbine performance characteristics.

6.2 Turbine Geometry

Eight 3D CFD models were developed to investigate the influence of helical blade overlap and section inclination on turbine performance characteristics. The baseline 0° (straight-bladed) turbine design was geometrically identical to a previously tested EFD turbine (Rawlings 2008) to permit validation of the modelling techniques utilised. The turbines were designed with ascending blade overlap angles of 0° (straight-bladed), 15°, 30°, 60° and 120° as shown in Tables 6.1 and 6.2, allowing the direct characterisation of blade overlap with power output, torque fluctuation levels, and mounting forces. The same blade profile was used for all overlap turbines in this series. However, to investigate the influence of blade section inclination, five 15° blade overlap models with blade sections inclined by -15°, 0°, +15°, +30°, and +45° from the horizontal rotation plane were also developed as shown in Figure 6.2.

To ensure the accuracy of the numerical methods utilised, validation studies were performed for two straight and one helical-bladed turbines, with all geometrical details shown in Tables

Table 6.1: Turbine Design Parameters

Blade overlap (Ø) and section inclination if not 0°	3D view	Overlap view
0°		
15°+0°		
15°-15°		
15°+15°		
15°+30°		
15°+45°		
30°		
60°		
120°		

Table 6.2: Turbine Geometrical Parameters

Nomenclature	0° (Rawlings 2008)	0°A (Rawlings 2008)	Lucid (Bachant 2011)
Number of blades	3	3	3
Blade section	NACA634021	NACA634021	NACA0020
Blade chord	0.0653	0.0653	0.14
Radius	0.4572m	0.4572m	0.5m
Blade span	0.6858m	0.6858m	1.32
Strut section	NACA0012	Shaped Bar	NACA0012
Strut chord	0.0653m	0.0467m	0.14m
Number of struts per blade	2	2	2
Shaft diameter	0.0483m	0.0483m	0.03175m

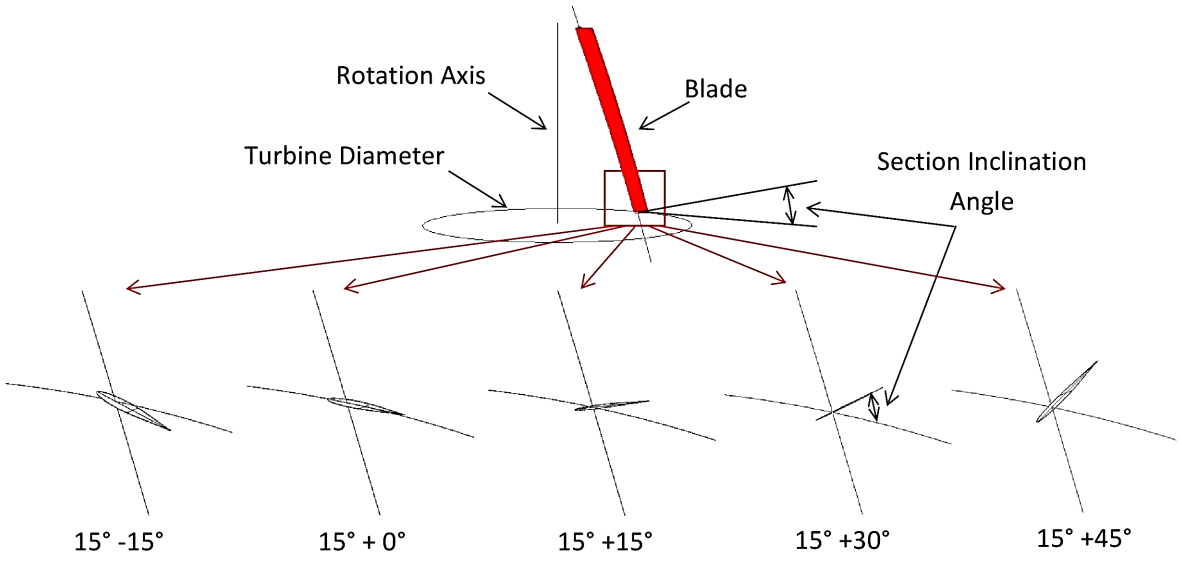

Figure 6.2: Definition of section inclination angle of the NACA634021 blade section to the horizontal rotation plane

6.2 and 6.3 (Bachant 2011, Bachant & Wosnik 2015, Rawlings 2008). All validation studies were performed at full-scale to ensure that the results were influenced by neither scaling nor Reynolds number effects. The 0° and 0°A turbines differed in strut section and strut location, allowing validation of geometrical changes against EFD results (Rawlings 2008).

Table 6.3: Validation Turbine Geometrical Design Parameters (Bachant 2011, Rawlings 2008)

Name	Blade overlap	Section inclination	3D view	Overlap view	Strut Connection
Lucid	60°	22°			
0°	0°	0°			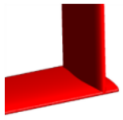
0°A	0°	0°			

6.3 Numerical Simulation Methodology

Turbine power output, torque fluctuation levels, and mounting loading were simulated using transient time-accurate 3D CFD models using ANSYS CFX (ANSYS 2010*a*), which solved the incompressible fully turbulent URANS equations using an element-based finite volume method. Several performance parameters were investigated to enable the quantification of turbine efficiency and loading characteristics. Turbine power output was evaluated as the power coefficient, C_p, given by,

$$C_p = \lambda \, C_m \tag{6.1}$$

where tip speed ratio, λ, was defined as,

$$\lambda = r\omega/V \tag{6.2}$$

where ω was the turbine rotational rate, r was the turbine radius, and V was the inflow velocity. The turbine torque coefficient, C_m, was determined as,

$$C_m = T/(0.5\rho V^2 Sr) \tag{6.3}$$

where ρ was the water density (set to 1000 $\frac{kg}{m^3}$ for all simulations), S was the turbine frontal area, and the torque T generated by the turbine was taken from the respective CFD or EFD results.

The k-ω SST turbulence model was utilised due to its ability to accurately model both free stream and boundary layer regions as well as offering improved prediction of flow separation and adverse pressure gradients by the inclusion of transport effects into the formulation of the eddy-viscosity (Menter 1994), with the k-ω SST CFD turbulence model commonly used for vertical axis turbine simulations (Castelli & Benini 2012, Dai & Lam 2009, Gretton 2009, Lain & Osorio 2010, Malipeddi & Chatterjee 2012, Marsh et al. 2012, 2013). To ensure numerical accuracy and stability, all simulations were performed using a bounded second order upwind-biased high order advection scheme along with an unbounded second order backwards Euler transient scheme (ANSYS 2010*a*). Simulations using a first order upwind advection and first order backwards Euler transient scheme resulted in extremely poor resolution of C_p. Convergence was deemed achieved when solution residuals reduced to below 10^{-4} and reduced by more than three orders of magnitude. Additionally convergence was confirmed by ensuring that the final C_p determined was within 5% of the previous rotations results, required due to the periodic nature of C_p. An example of C_p convergence for the 0° turbine is shown in Figure 6.3, where C_p values converged after approximately 3600 time steps, corresponding to 9 rotations. To reduce overall simulation times all simulations were started using previous results if available.

All turbine models were meshed using unstructured tetrahedral elements using ANSYS CFX 13.0 (ANSYS 2010*a*) and included all blades, struts, hubs, and the shaft. Mesh resolution was set by specifying the mesh size and growth rates to allow for local refinement of mesh zones. Mesh density was varied according to expected flow curvature rates resulting in increased mesh density in regions near the blades, struts, hubs, shaft, and turbine wake region. Mesh density near the leading and trailing edges of the blades and strut sections was increased compared to density in the central sections to capture the expected flow velocity gradients using the ANSYS curvature function (ANSYS 2010*a*). Mesh density was reduced away from the surfaces to minimise computational effort such as on the domain boundary fields. Inflation layers were used on all surfaces to fully resolve the boundary layer flow. Total boundary layer thickness was estimated as $0.37c/Re^{1/5}$ with the blade chord c used to determine Reynolds

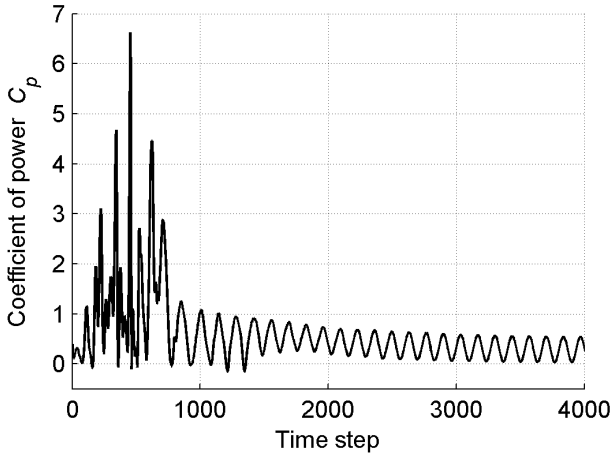

Figure 6.3: Example of C_p convergence for the 0° turbine at λ=2.75 at an inflow velocity of 1.5 ms^1

number, Re (Anderson, 1985). The estimated thickness was doubled to ensure the boundary layer was contained within the prescribed inflation layer region, with a total of 30 layers used to capture the boundary layer flow. Inflation layer mesh growth rates were limited to 1.2, with lower growth rates resulting in excess boundary layer mesh with no beneficial increase in power output simulation accuracy. Boundary layer mesh density independence was evaluated by examining the influence on power output of the average height of the first cell from the turbine walls, known as the non-dimensional variable $y+$. The resultant $y+$ values for all 3D models was approximately $y+$=0.75, which aligned well with recommended near wall resolution ranges for the k-ω SST turbulence model (ANSYS 2010a). Simulations using reduced boundary layer inflation density and thus higher $y+$ values resulted in reduced simulation accuracy as the ANSYS-prescribed wall functions (ANSYS 2010a) were unable to resolve the flow near the walls due to high levels of separation and adverse pressure gradients.

Turbine rotation was simulated by enclosing the turbine in an inner domain as shown in Figure 6.4 that was rotated using the CFX transient rotor-stator model at the desired λ corresponding to the relevant CFD or EFD rotational rates. The interface between the stationary and rotating domains was modelled using a General Grid Interface (GGI) over which flow values were calculated using an intersection algorithm (ANSYS 2010a). The GGI interface was placed at 1.5 times turbine diameter from the rotational axis to limit any interpolation errors on power output predictions by increasing clearance between the blades and the interface.

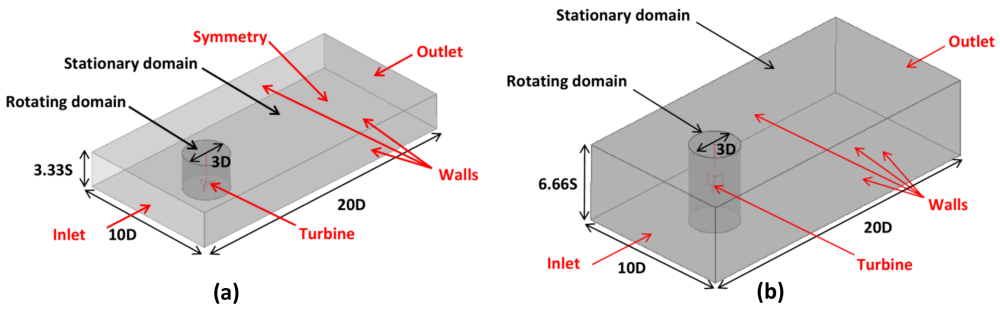

Figure 6.4: Domain boundary nomenclature and sizing for (a) symmetrically reduced and (b) full domain. Dimensions in relation to turbine diameter, D, and span, S

The computational domains shown in Figure 6.4 were generated to simulate free stream conditions with all corresponding boundary conditions outlined in Table 6.4. To ensure that the turbines were isolated from any domain wall effects and to allow for full wake development, systematic domain size studies were performed. These studies ensured that the domain walls did not influence C_p results, allowing the use of blockage-corrected EFD data where available. All turbines were assumed to operate at sufficient depth to minimise any free surface interaction effects. A reduced domain was used for the 0° and 0°A turbines due to symmetry about the horizontal axis as shown in Figure 6.4. To ensure that this use of domain symmetry did not affect simulation accuracy, equivalent simulations were carried out on full and half domains. The differences in C_p for the two domains were less than 0.4%, justifying the employment of the half domain thus reducing the overall mesh size by a factor of two. Symmetry could not be used to reduce the size and hence mesh element counts of the helical turbine models as they were not symmetric about the horizontal axis.

Table 6.4: Boundary Conditions for all Turbines

Domain Wall	Boundary Condition
Inlet	Uniform flow: 1.5 ms^{-1} for helical study 1 ms^{-1} for Lucid study
Inlet turbulence level	5% turbulence
Outlet	Relative Pressure - 0Pa
Walls	Free slip walls
Turbine	No slip wall

Studies of the influence of factors including mesh density, time step size, $y+$, domain length, width, height, and domain symmetry were conducted. Independence was deemed satisfactory when changes in these parameters resulted in C_p differences between successive refinements

trending to less than 5%, resulting in a suitable balance between solution accuracy and computational effort (Tu et al. 2013). Whilst examples of this method are shown in Figure 6.5 for the 0° and 15° overlap turbines, spatial and temporal independence was determined for all turbine models with most simulations exhibiting monotonic convergence characteristics. The resultant mesh element counts and time step sizes are outlined in Table 6.5.

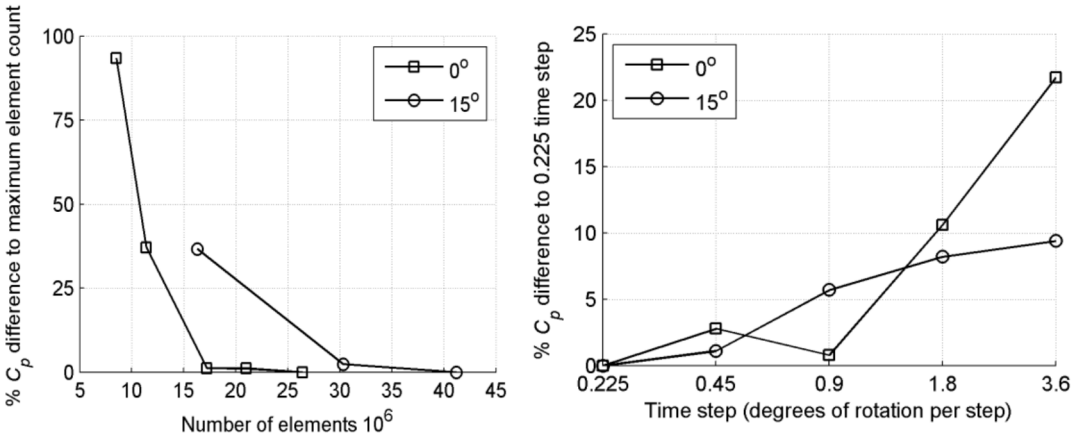

Figure 6.5: Example of spatial and temporal independence for the 0° and 15° blade overlap turbines at λ=2.75 at an inflow velocity of 1.5 ms^1

Table 6.5: Spatial and Temporal Independence Results

Turbine	0°A	0°B	Lucid	15°-15°	15°+0°	15°+15°	15°+30°	15°+45°	30°	60°	120°
Mesh size 10^6	17.2	17.3	37.2	31.9	30.3	30.9	30.0	29.8	31.7	37.0	54.0
Rotation / timestep	0.9°	0.9°	0.9°	0.45°	0.45°	0.45°	0.45°	0.45°	0.45°	0.45°	0.45°

6.4 Validation Studies

Validation studies of the Lucid model were conducted against EFD testing available from literature of a geometrically identical turbine at the University of New Hampshire Tow and-Wave Tank at the Chase Ocean Engineering Laboratory, a 36.6m long, by 3.66m wide and 2.13m deep testing tank (Bachant 2011, Bachant & Wosnik 2015). Measurements of torque generated at inflow velocities ranging from 0.6 ms^{-1} to 1.3 ms^{-1} were obtained at varying rotational rates using a torque transducer and a hydraulic disk brake arrangement. Comparisons of CFD and EFD $C_p - \lambda$ performance curves for the Lucid turbine are shown in Figure 6.6. There was good agreement between the CFD and EFD results, with both the

shape of the $C_p - \lambda$ curve and maximum C_p magnitudes correlating well, with for example the CFD C_p of 0.236 was within 4.8% of the EFD C_p of 0.248 at λ =2. The $C_p - \lambda$ curve was shifted minimally to lower C_p values at λ increased. The under prediction of C_p may result from over prediction of blade and strut drag as a consequence of the use of a fully turbulent CFD model, as they often overestimate skin friction and hence drag particularly at low angles of attack that occur at high λ (Sørensen 2009). Fully turbulent models will also not capture any laminar-to-turbulent flow transition effects which may occur due to flow Reynolds numbers which were less than 500,000. Given the replication of the shape of the $C_p - \lambda$ curve and the accurate prediction of maximum C_p the additional computational expense (ANSYS 2010*a*) of laminar-to-turbulent transitional models was not deemed necessary.

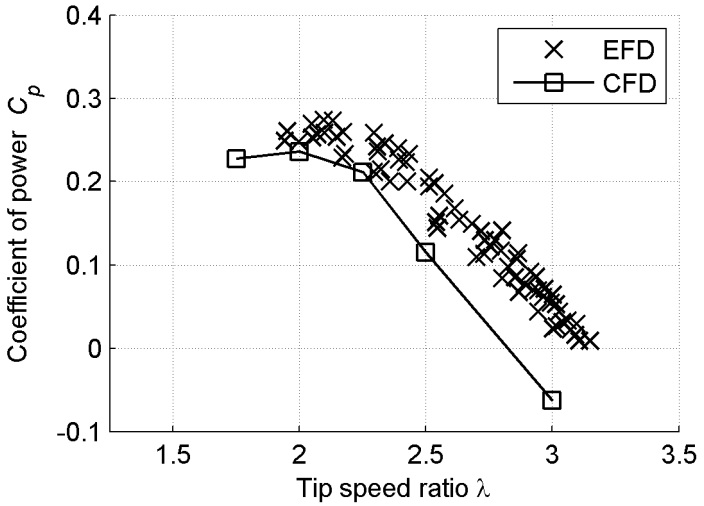

Figure 6.6: Comparison of CFD and EFD $C_p - \lambda$ curves for Lucid turbine at an inflow velocity of 1 ms^1 (Bachant 2011, Bachant & Wosnik 2015)

Validation of the 0° and 0°A CFD models shown in Table 6.3 was performed against EFD results available in the literature for two geometrically identical turbines conducted at the University of British Columbia's towing tank, a 60.1m long, 3.7m wide and 2.4m deep facility (Rawlings 2008). Using a torque sensor and rotation rate encoder, power output was measured for varying rotational rates from λ =1.5 to 3.5 at an inflow velocity of 1.5 ms^{-1}. Figure 6.7 shows the comparisons of CFD and EFD $C_p - \lambda$ curves for the 0° and 0°A turbines shown in Table 6.3 at 1.5 ms^{-1}. At low λ (less than 2.5) good agreement was found between the CFD and EFD results for both turbines, with differences in C_p between CFD and EFD results for turbine 0° of 17% and 0.8% at λ =1.5 and 2.5 respectively. Turbine 0°A prediction accuracy at low λ was similar with differences in C_p prediction of 14.4%, and 1.7% at

λ =2 and 2.25 respectively. However, C_p prediction accuracy reduced as λ increased past the location of maximum C_p with CFD C_p values shifted lower. The authors suggest that the reasons for increased error at high λ are threefold: lack of blockage corrections, the use of a fully turbulent CFD model, and possible experimental inconsistencies at higher rotational rates. The EFD results did not account for the tank blockage of 8% by the turbine, which may reduce C_p magnitudes and shift the $C_p - \lambda$ curve to lower λ values as shown in Lucid EFD, where C_p was reduced on average by 25% (Bachant 2011, Bachant & Wosnik 2015). The under prediction of C_p at high λ may also result from over prediction of blade and strut drag as a result of the use of a fully turbulent CFD model, which often overestimate skin friction and hence drag (Sørensen 2009). Fully turbulent models will also not capture any laminar-to-turbulent flow transition effects which may occur due to the low blade and strut Reynolds numbers of less than 500,000. Additionally the $C_p - \lambda$ curve for the 0° turbine appears to plateau whereas all other EFD from the same testing regime (Rawlings 2008) revealed rapid decreases in C_p at high λ, suggesting possible experimental error at λ =3.5.

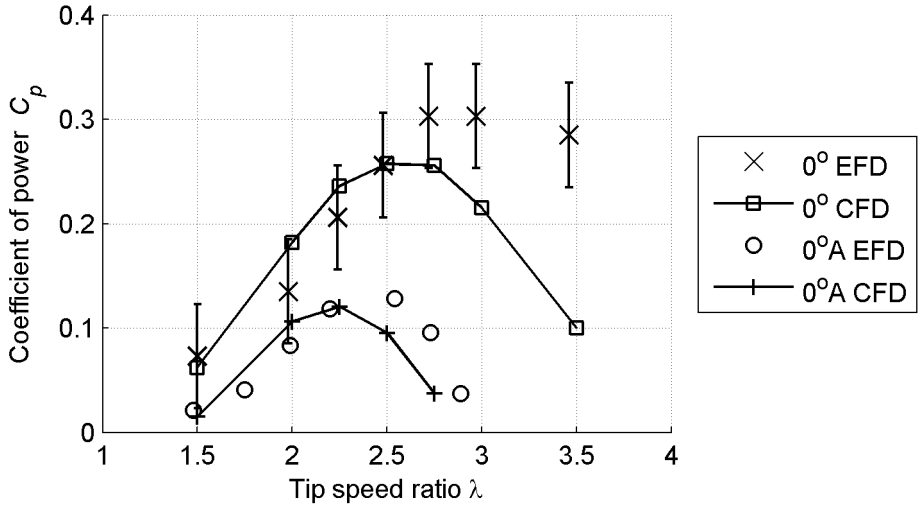

Figure 6.7: Comparison of CFD and EFD $C_p\lambda$ curves for the 0° and 0°A turbines at an inflow velocity of 1.5 ms^{-1}. Error bars only reported for Turbine 0° (Rawlings 2008)

The CFD models accurately captured the effect of geometrical changes on maximum C_p with results correlating to within 4.8%, 14.3% and 6.3% of the EFD results for the Lucid, 0° and 0°A turbines respectively. This prediction accuracy is higher than previous CFD predictions available in the literature, which exhibited maximum C_p prediction errors of more than 45% (Castelli et al. 2010, Danao 2012, Hall 2012, Malipeddi & Chatterjee 2012, Matre et al. 2013, McLaren 2011).

6.5 Computational Requirements

Total simulation time was found to vary significantly as mesh element counts increased with blade overlap angle as shown in Table 6.5. Simulations for one revolution of the 0° overlap turbine model took 24 h on an 18 core cluster comprising of Intel Core 2 Quad Q9300 processors with 2 GB memory per core. However simulations for the 120° overlap turbine took in excess of 72 h for one revolution on 50 cores of the same cluster as a result of the increase in mesh element counts. Due to the continual increases of computing power available to CFD users, the use of full 3D CFD simulation models for vertical axis turbines is now possible without the need for unrealistic computational resources or time requirements.

6.6 Results and Discussion

The influence of overlap angle and section inclination angle on power output, torque oscillation levels and mounting forces was determined using 3D CFD models at an inflow velocity of 1.5 ms^{-1}. The 3D CFD models utilised varied in blade overlap angles from 0° (straight-bladed) to 120° and section inclination angles from -15° to 45° to determine any relationships between turbine geometrical design and performance.

6.6.1 Influence of helicity on power output

Figure 6.8 shows comparisons of CFD simulation results of power output for varying blade overlap angles. Power output was found to be directly proportional to blade overlap. The highest C_p=0.258 was found for the 0° blade overlap turbine. As helicity increased maximum C_p reduced, eventually becoming negative at all λ for the 120° overlap turbine. These results signify that turbines with 0° blade overlap, known as straight-bladed turbines, will develop the highest C_p. As blade overlap increased, the $C_p - \lambda$ curves shifted to lower C_p values for all λ as the reductions in the blade inclination angle to the inflow increased the magnitude of spanwise flow over the blades. The $C_p - \lambda$ coefficient curves for all helical turbines were shifted to higher λ by λ=0.25 when compared to the 0° overlap turbine, as the spanwise flow deformation reduced the effective blade chord and thus turbine solidity.

Differences in flow deformation are shown in Figure 6.9 for the 0°, 60° and 120° overlap turbines. Flow over the 0° overlap turbine was perpendicular to the blade section due to

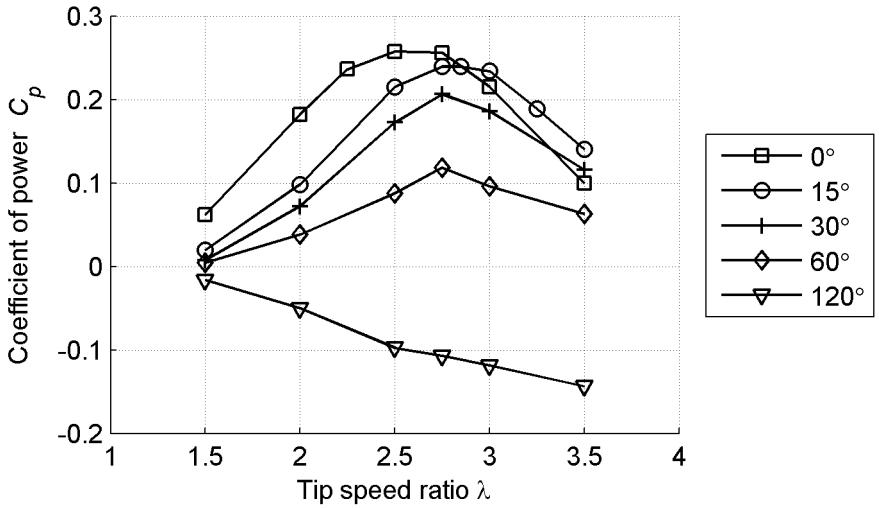

Figure 6.8: Comparison of CFD $C_p - \lambda$ curves for blade overlap angles from 0° to 120° at an inflow velocity of 1.5 ms^{-1}

the blade inclination angle of 90°, resulting in optimal hydrodynamic section alignment and thus maximum power output. However, the flow over the blades of the 60° overlap turbine was deformed in a spanwise direction, reducing the hydrodynamic efficiency of the NACA sections. Correspondingly at 120° overlap the blade sections were poorly aligned with the flow, resulting in negative power outputs for all λ. This flow deformation was found by Castelli and Benini (Castelli & Benini 2012), who also found a corresponding increase in C_p as helicity reduced.

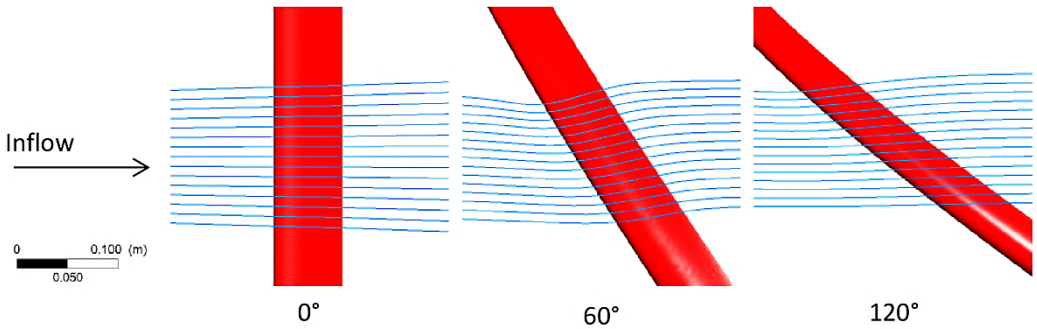

Figure 6.9: Comparison of inclination of flow for 0°, 60°, and 120° overlap angle turbines at an inflow velocity of 1.5 ms^{-1}, λ=2.75

The derived relationship between helicity and C_p is supported by EFD and CFD research from literature where C_p was demonstrated to increase as helicity reduced (Castelli & Benini

2012, Niblick 2012, Shiono et al. 2002). However, Gorlov found during EFD that helical turbines demonstrated C_p increases of up to 95% when compared to straight-bladed turbines (Gorlov 1998, 2002). The majority of the published EFD and CFD works however agree that increased helicity results in reduced power output, with straight-bladed turbines generating the highest C_p for any given turbine frontal area.

Comparisons of helicity are shown in Figure 6.10 for the 60° and 0° overlap angle turbines. Large levels of flow disruption over the 60° overlap turbine's blades can be seen, which occurred as a result of the spanwise flow caused by the inclination of the turbines blades. This spanwise flow may reduce hydrodynamic performance as the shed vortices traverse down the helical blades. In comparison significant reductions in flow disruption over the blade and strut sections of the 0° overlap turbine are shown when compared to the 60° overlap turbine. Differences in tip vortex magnitudes can also be seen that were generated by differences in pressure variations over the lifting blade surfaces between the two designs.

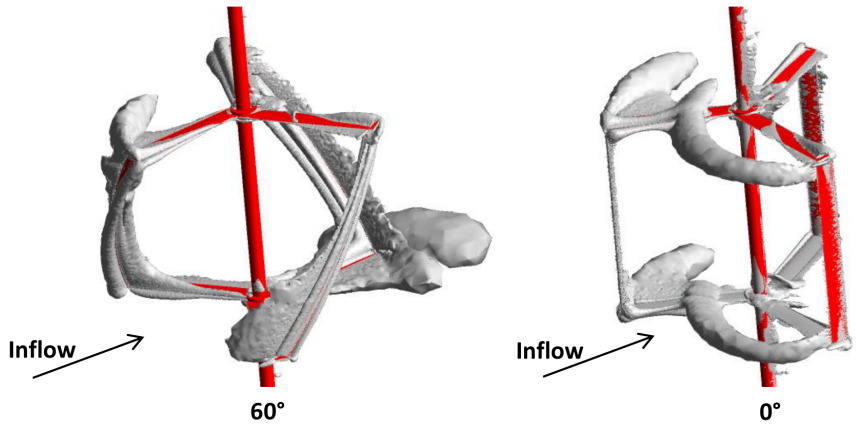

Figure 6.10: Vortex shedding comparisons between the 60° and 0° overlap angle turbines, vorticity of 16 s^{-1} at an inflow velocity of 1.5 ms^{-1} at λ=2.75

6.6.2 Influence of blade section inclination on power output

To examine the influence of blade section inclination CFD simulations were performed for five turbines with differing section inclination angles as shown in Figure 6.11. For section inclination angles of 0°, 15°, and 30° minimal changes in C_p were found as the hydrodynamic profile of the blade section perpendicular to the flow did not vary significantly. However the +45° and -15° blade sections were at increasingly tangential angles to the flow reducing

their efficiency. These results indicate that blade section inclination is not critical for helical vertical axis turbines as long as the blade sections are approximately perpendicular to the leading edge.

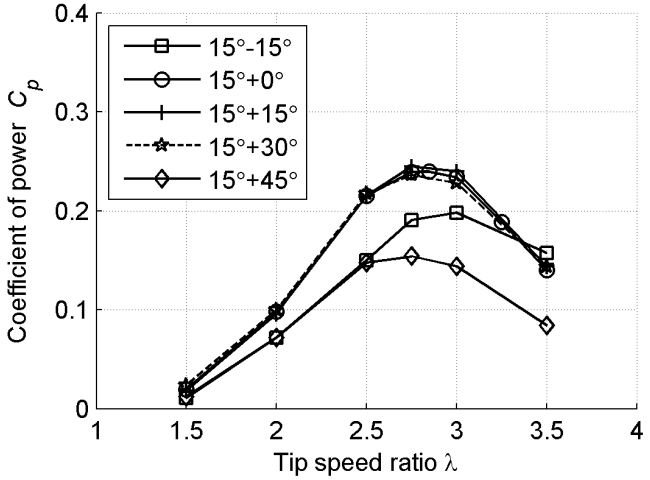

Figure 6.11: Section inclination effects on the $C_p - \lambda$ curves of the 15° overlap angle turbines with section inclination angles of -15°, 0°, +15°, +30° and +45° at an inflow velocity of 1.5 ms^{-1}

6.6.3 Influence of helicity on torque oscillation levels

Straight-bladed vertical axis turbines experience significant cyclic torque oscillations as a result of variations in blade angles of attack over each revolution (Malipeddi & Chatterjee 2012, Paraschivoiu 2002, Winchester & Quayle 2011). These oscillations generate alternating loading forces on the turbine structure that can lead to premature failure through fatigue (Gorlov 1998, Scheurich et al. 2011). Helical turbines have been shown to reduce levels of toque oscillations due to their blade distribution around the rotational axis (Gorlov 1998, 2002, Kirke 2011, Niblick 2012, Shiono et al. 2002). This distribution ensures that the flow does not stall along the full blade length simultaneously, reducing peaks in tangential force levels and thus moment coefficients. An example of this effect is shown in Figure 6.12. Three distinct peaks in torque coefficients for each turbine occur as each of the three blades generates peaks in tangential force in the upstream section of the turbine (Paraschivoiu 2002). However, peak helical torque coefficients are reduced by 57.3% for the 60° overlap turbine in comparison to the 0° overlap turbine as a result of the helical blade distribution. Visually the effect of this distribution is shown in Figure 6.13. The flow angle of attack over the 60° overlap turbine varies with blade span as a result of the blade distribution, reducing peak

tangential forces and thus moment coefficients. In contrast since the flow angle of attack of the 0° overlap turbine does not vary with blade span, it generates large instantaneous peaks in tangential force and thus moment coefficient peaks.

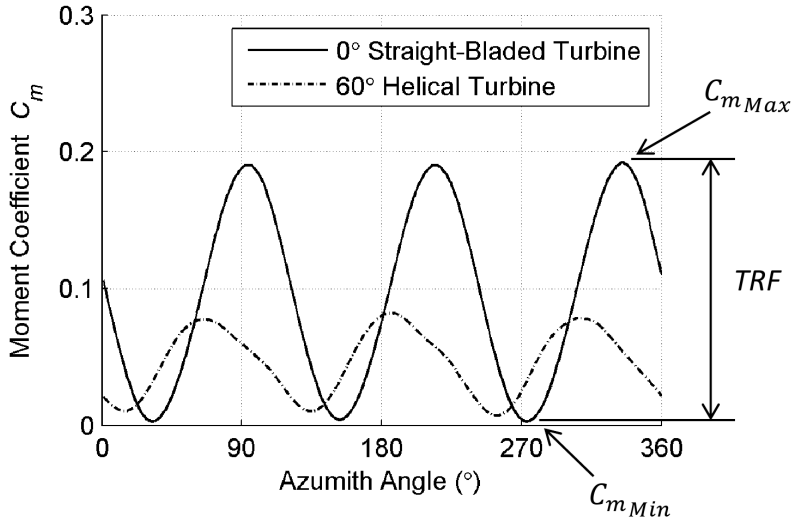

Figure 6.12: Variations in C_m for one revolution for the 0° and 60° overlap angle turbines at an inflow velocity of 1.5 ms^{-1} at λ=2.75

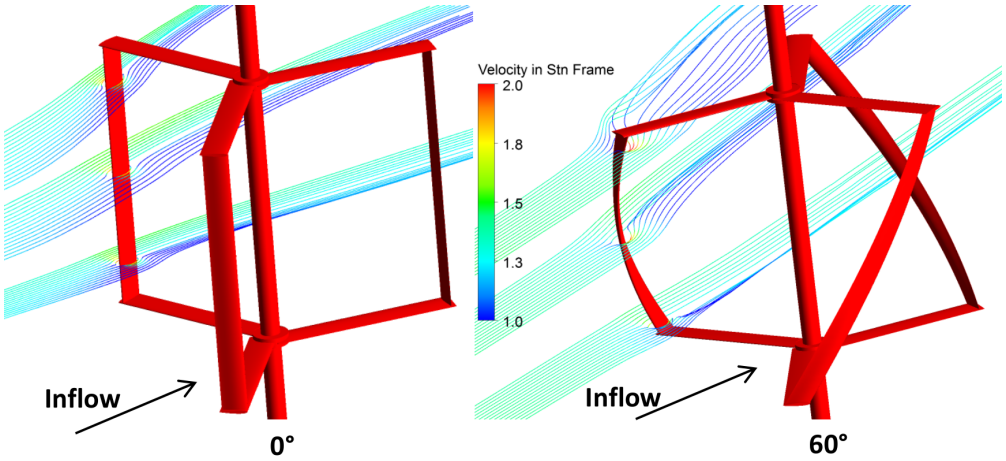

Figure 6.13: Angle of attack variations with span for the 0° and 60° overlap angle turbines at an inflow velocity of 1.5 ms^{-1} at λ=2.75

To quantify relationships between blade overlap angle and torque oscillation levels, a series of turbines with blade overlap angles ranging from 0° to 120° were simulated. Various methods for quantifying torque fluctuations have previously been used (Navabi 2008, Shiono et al. 2002, Winchester & Quayle 2011); in this work torque oscillations were quantified as Torque

Ripple Factor (TRF), defined as,

$$TRF = C_{m_{Max}} - C_{m_{Min}} \tag{6.4}$$

where $C_{m_{Max}}$ and $C_{m_{Min}}$ were the maximum and minimum moment coefficients as illustrated in Figure 6.12 for the 0° overlap turbine at λ =2.75. This formulation allows for easy comparison of the range of torque variations experienced and is similar to that used by Winchester and Quayle (Winchester & Quayle 2011) and Shiono et al. (Shiono et al. 2002).

Comparisons of TRF are shown in Figure 6.14 for blade overlap angles of 0°,15°, 30°, 60°, and 120°. All $TRF - \lambda$ curves prescribe the same form with locations of peak TRF found around the λ location of maximum C_p, reflecting the large variations of tangential forces found at these λ. Significant reductions of up to 71.7% in TRF levels at λ =2 were found when comparing the 0° and 120° overlap turbine's as the overlap reduces peaks in tangential forces. These results are supported by EFD of helical turbines in literature (Gorlov 1998, 2002, Kirke 2011, Niblick 2012, Shiono et al. 2002) where TRF levels were found to be significantly reduced when compared to straight-bladed designs. Maximum C_p and TRF levels were found to decrease at comparable rates with increasing helicity. Thus, if reductions in TRF are desired, helicity could be increased, although this will also reduce the maximum C_p.

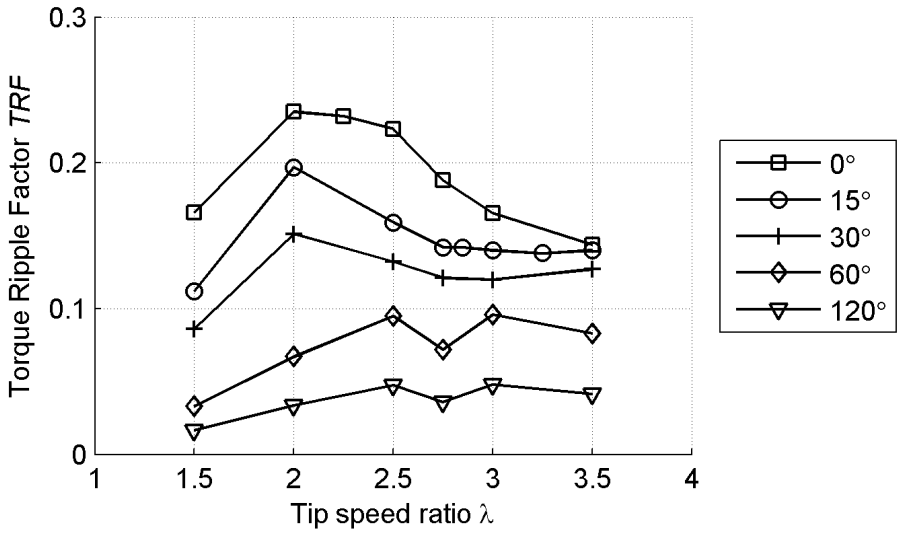

Figure 6.14: Comparisons of $TRF - \lambda$ for varying overlap angles turbines from 0° to 120° at an inflow velocity of 1.5 ms^{-1}

The effects of blade section inclination angle on TRF are shown in Figure 6.15. In a similar manner to Figure 6.14, all curves followed a similar $TRF - \lambda$ shape, with the peaks located around the λ for maximum C_p, reflecting the large variations of tangential forces found at these λ. The 15°+0°, 15+15°, and 15°+30° section inclination turbines exhibited similar TRF magnitudes as the blades were approximately aligned with the inflow, resulting in similar power output magnitudes. However, the 15°-15° and 15°+45° section inclination turbines exhibited reduced TRF as the inclination of the blade sections resulted in reductions in the magnitudes of the alternating forces on the blades. Although beneficial, these reductions in TRF were accompanied with reductions in power output.

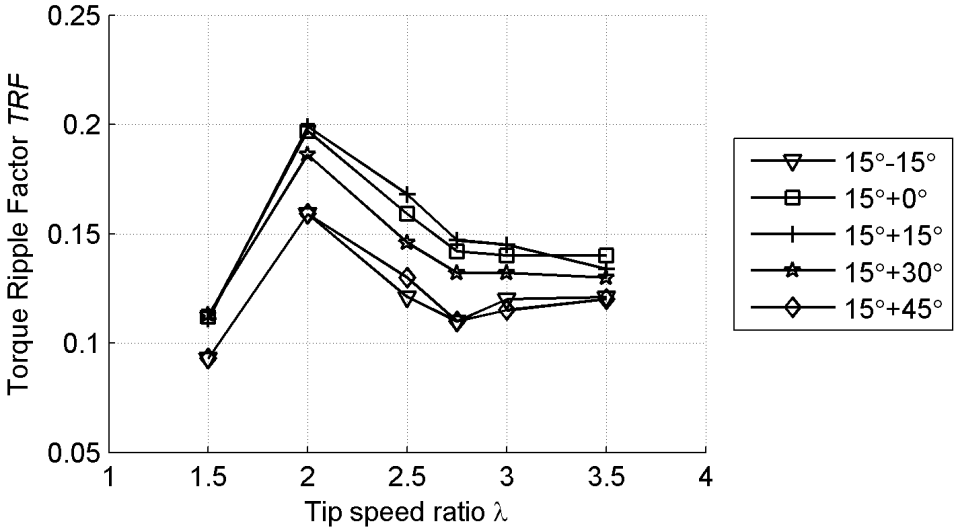

Figure 6.15: Comparisons of TRF- for 15° overlap angle helical turbines with section inclination angles from 15° to 45° at an inflow velocity of 1.5 ms^{-1}

6.6.4 Influence of helicity on turbine mounting forces

Inline, lateral, and vertical forces shown in Figure 6.16 were determined for turbines with blade overlap angles of 0° and 15°, as increasing overlap above 15° resulted in significant reductions in C_p as shown in Figure 6.8. Inline, lateral, vertical and maximum forces were non-dimensionalised by $1/2\rho V^2 S$ to form the force coefficients C_{FX}, C_{FY} , C_{FZ} and C_{FMax} respectively. To ensure CFD simulation accuracy, validation studies were performed against measurements of inline drag obtained from EFD studies available within the literature for the 0° and Lucid turbines (Bachant 2011, Bachant & Wosnik 2015, Rawlings 2008).

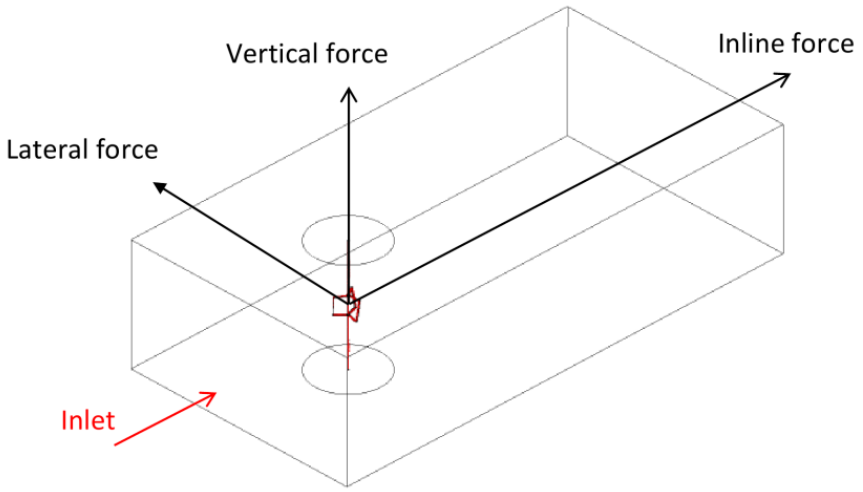

Figure 6.16: Definitions of lateral, inline, and vertical force vectors for the 3D CFD domains

Comparisons of average CFD and EFD (Rawlings 2008) inline force coefficients (C_{FX}) for the 0° overlap turbine are shown in Figure 6.17. Reasonable agreement between CFD and EFD was found across most λ with differences of 8.2% and 2.5% at λ =2 and λ =2.5 respectively. Reductions in the slope of the CFD curve when compared to EFD may be due to blockage effects which were not accounted for in the CFD studies. Additionally the EFD results do not closely follow any trend with possible experimental error in C_{FX} results at λ =2.25. The inline force magnitude increased with λ due to increased flow turbulence levels over the struts, which increased strut drag and thus the resistive torque generated (Marsh et al. 2012, 2013). Increases in inline drag force also occurred as the turbine acts more like a solid body at high λ rates (Bachant & Wosnik 2015). Inline force coefficients were also derived for the Lucid turbine as shown in Figure 6.17 and compared against EFD results (Bachant 2011, Bachant & Wosnik 2015). Good agreement between CFD and EFD was found, with all CFD results falling within the reported error bars. Inline force coefficients were approximately constant with λ showing similarities with the 0° overlap turbine in Figure 6.17, where the inline force coefficients appear to plateau at high λ values.

Simulation results for all force coefficients are shown in Figure 6.18 for the 0° and 15° overlap turbines. The average lateral forces, C_{FY}, for both turbines remained relatively constant across λ and were approximately 75% lower than inline force coefficients, C_{FX}. Average C_{FX} for both turbines rose then appeared to plateau around the λ location where maximum C_p was found as shown in Figure 6.8 as the turbines act more like solid bodies at high λ rates (Bachant & Wosnik 2015). Reductions in C_{FX} for the 15° blade overlap turbine of

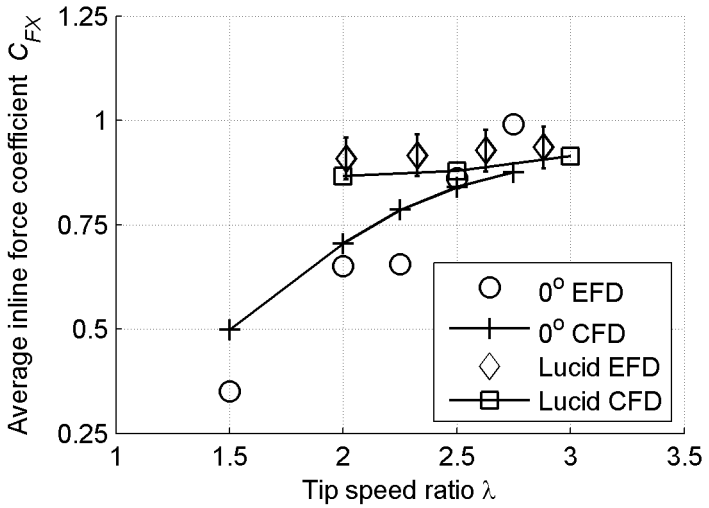

Figure 6.17: Comparison of average CFD and EFD inline force coefficient, C_{FX}, for the 0° blade overlap (Rawlings 2008) and Lucid (Bachant 2011, Bachant & Wosnik 2015) turbine at an inflow velocity of 1.5 ms^{-1}. Lucid error bars reported in EFD (Bachant & Wosnik 2015), no error bars reported in EFD for 0° blade overlap turbine (Rawlings 2008)

approximately 20% were found when compared to the 0° overlap turbine, as the flow in the downstream direction was not impacting on the full 0° blade overlap turbine rectangular blade area, but rather on a reduced frontal blade area caused by the helicity of the blades. This inline surface area effect is reduced as λ increases as the turbine blades act more like a solid body, with results converging for both turbines (Bachant & Wosnik 2015). Vertical forces, C_{FZ}, were also calculated for the 15° overlap turbine as shown in Figure 6.18, resulting from the spanwise flow deformation illustrated in Figure 6.9. These can lead to axial loadings on shaft bearings, however the force magnitudes were small compared with C_{FX} and C_{FY} . Conversely, 0° overlap turbines in uniform flow exhibit no vertical forces due to their horizontal symmetry. Predicted maximum mounting force coefficients, C_{FMax}, for the 0° and 15° overlap angle turbines were found to be up to 40% higher than the average forces due to TRF, with the average loading forces slowly plateauing above λ =3 due to reductions in shaft drag and changes in blockage as λ increased. The helical distribution of the blades of the 15° blade overlap angle turbine around the rotational axis resulted in reductions of C_{FMax} when compared to the 0° overlap turbine; however as λ increases the results appear to converge due to blockage effects at high λ.

The fluctuating forces in the inline and lateral directions generated cyclical loading as shown in Figure 6.19. This cyclical loading may induce structural resonance depending on the nat-

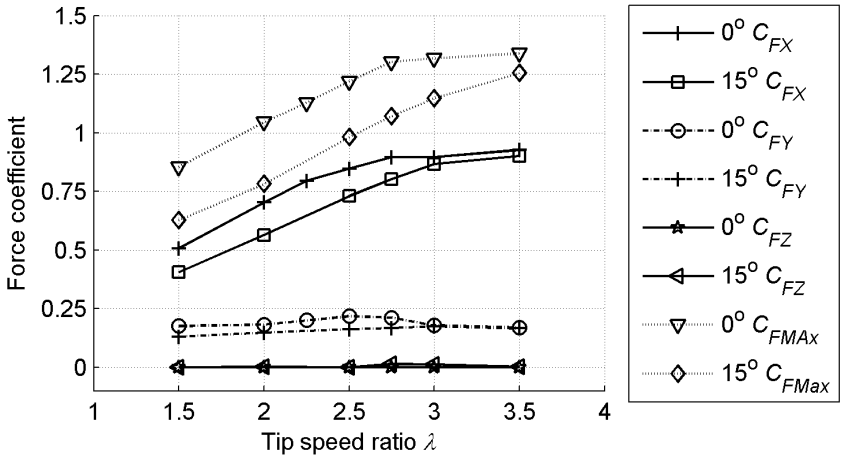

Figure 6.18: Comparison of average inline, C_{FX}, lateral, C_{FY}, vertical, C_{FZ}, and maximum, force coefficients, C_{FMax} for the 0° and 15° overlap angle helical turbines at 1.5 ms^{-1}

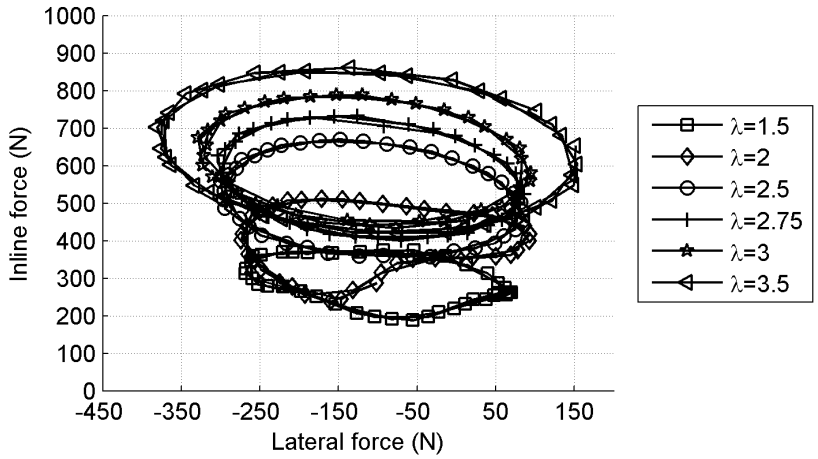

Figure 6.19: Cyclical mounting forces loading for the 15° blade overlap angle turbine for one revolution at an inflow velocity of 1.5 ms^{-1}

ural frequency response of the turbine structure. Using 3D CFD simulations, cyclic force levels over each revolution as well as their frequency can be obtained, which when combined with natural frequency calculations may allow for the alleviation of any unwanted structural resonance effects.

6.7 Conclusions

The hydrodynamic performance of straight and helical-bladed vertical axis turbines was investigated using validated 3D URANS CFD simulation models. Helicity was found to generate significant spanwise flow, reducing lift and increasing drag on the turbine blades. Thus straight-bladed turbines, which by definition have a blade overlap of 0° and thus no blade helicity, will generate the highest power output when compared to helical turbines of the same frontal area. The significance of this cannot be underestimated; straight-bladed turbines exhibit higher power output when compared to helical-bladed designs.

Although helical turbines exhibit lower power output than straight-bladed turbines they offer some advantages. The curvature of the blades around the rotational axis was found to reduce torque oscillation and unsteady force loading levels. Differences in mounting forces were also determined between straight and helical-bladed turbines, with reductions in force coefficients found for the helical-bladed turbine as a result of the blade distribution around the rotational axis. The 15° overlap helical turbine also generated vertical forces unlike the 0° straight-bladed counterpart, again due to differences in blade distribution, although all vertical axis forces were not significant. For both turbines, the maximum forces were found to be more than 40% higher than the average forces.

This study reveals three key conclusions:

- Straight-bladed turbines generate higher power output than helical turbines;
- Helical turbines are better at reducing torque oscillation levels and mounting forces, although maximum power output will be reduced; and
- Blade section alignment to the inflow is not critical as long as the blade section is approximately perpendicular to the blade leading edge.

The 3D CFD models developed in this paper will be used to further investigate the blade

loading of helical and straight-bladed vertical axis turbines. As a result of the relationships between blade helicity and power output shown here only turbines with low blade overlaps will be investigated to maximise power generation capacity.

Chapter 7

Numerical Simulation of the Loading Characteristics of Straight and Helical-Bladed Vertical Axis Tidal Turbines

This chapter has been submitted for publication in the Journal *Renewable Energy* and at the time of writing is under review. The citation for the research article is:

Marsh P., Ranmuthugala, D., Penesis, I., & Thomas, G. Numerical Investigation of the Influence of Blade Helicity on the Performance Characteristics of Vertical Axis Tidal Turbines, [Under review, 2015].

Abstract

The stress and deflection of straight and helical-bladed vertical axis turbines was investigated using hydrodynamic and structural analysis models. Using Double Multiple Streamtube (DMS) and Computational Fluid Dynamics (CFD) models, the hydrodynamic forces and pressures on the turbines were modeled for three rotational rates from startup to over speed conditions. The results from these hydrodynamic models were used to determine stress and total deflection levels using beam theory and Finite Element Analysis (FEA) methods. Maximum stress and deflection levels were found when the blades were aligned with the inflow in the upstream region, with the highest stresses found at the blade-strut joints. The helical turbine exhibited on average 13% lower maximum stress levels than the straight-bladed turbine, due to the helical distribution of the blades around the rotational axis. All simulation models offered similar accuracy when predicting maximum blade stress and deflection levels; however for detailed analysis of the blade-strut joints the more computationally demanding CFD-FEA models were required. Straight-bladed, rather than helical turbines, are suggested to be more suited for tidal installations, as for the turbines studied in this work they produced 8% higher power output with only 13% greater structural stress loading.

7.1 Introduction

Existing studies of vertical axis turbines used for ocean power generation have concentrated primarily on hydrodynamics rather than structural analysis, as researchers have sought to maximise power output. To ensure longevity in marine environments however, detailed knowledge of turbine structural loading characteristics must be established. Although possible using strain gauges, Experimental Fluid Dynamics (EFD) studies to obtain loading are rarely performed. This fact, when combined with a general lack of turbine development over the last 15 years, has limited turbine usage (Sutherland et al. 2012). However, knowledge of turbine hydrodynamics and structural characteristics can be obtained by numerical simulation using methods such as coupled Computational Fluid Dynamics (CFD) and Finite Element Analysis (FEA) codes. Additional research into both hydrodynamics and structural characteristics using numerical techniques will further understanding of turbine operational characteristics.

Both straight and helical-bladed designs, as shown in Figure 7.1, are proposed by various

researchers to generate power from the oceans kinetic energy (Hameed & Afaq 2013, Li et al. 2014, Marsh et al. 2015*a*, Paraschivoiu et al. 2012). The designs differ in blade helicity, defined by the blade overlap angle ϕ shown in Figure 7.1. Straight-bladed turbine have 0° blade overlap, whereas helical turbines use blades that are distributed around the rotational axis at a defined overlap angle of ϕ. Previous research by the authors indicated that straight-bladed designs generated higher power output when compared to helical turbines of the same frontal area and blade section as a result of the inclination of the helical turbines blades to the inflow (Marsh et al. 2015*a*). Conversely, helical turbine torque oscillation levels and mounting forces were reduced when compared to straight-bladed turbines, due to the distribution of the turbine blades around the rotational axis (Marsh et al. 2015*a*). Comparisons of the influence of these factors on the structural loading characteristics of the two designs is currently unknown, as previous research into loading characteristics has concentrated primarily on straight-bladed turbine designs.

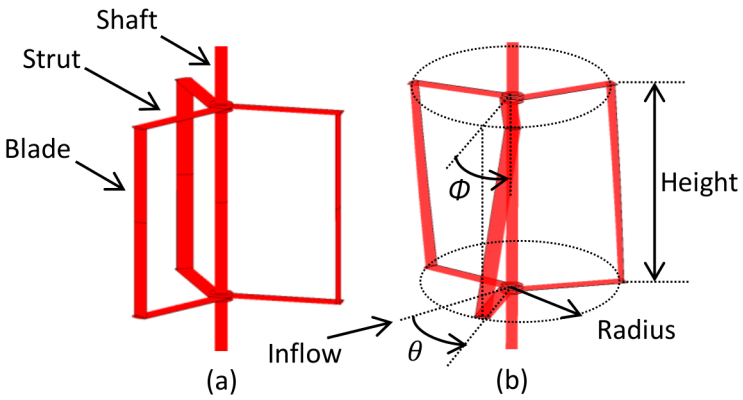

Figure 7.1: Straight (a) and helical-bladed (b) vertical axis turbines, showing definitions of azimuth rotational angle θ, and blade overlap angle ϕ

Characterization of vertical axis turbine loading characteristics can be performed numerically by coupling Double Multiple Streamtube and CFD models with beam theory or FEA analysis methods (Hameed & Afaq 2013, Li et al. 2014, Paraschivoiu et al. 2012, Tsai & Chen 2014). However, considerable knowledge gaps exist in the characterisation of structural loading. Previous numerical studies have often been limited to either helical or straight-bladed designs (Hameed & Afaq 2013, Li et al. 2014, Paraschivoiu et al. 2012, Tsai & Chen 2014), with no comparison between loading characteristics of the two designs performed. These works have often concentrated on blade loading, with no determination of the loading of the struts and blade-strut joints performed (Hameed & Afaq 2013, Paraschivoiu et al. 2012, Tsai

& Chen 2014). Additionally, previous simulations have concentrated on evaluating loading characteristics at a single rotational rate (Hameed & Afaq 2013, Li et al. 2014, Paraschivoiu et al. 2012, Tsai & Chen 2014). Research extending numerical simulation models to investigate straight and helical-bladed turbines using models with all geometrical features including struts at multiple rotation rates will give greater insight into turbine characteristics, and allow for the evaluation of any advantages between the differing geometrical layouts.

In this current study, the blade loading of a straight and helical-bladed vertical axis turbine was determined to characterise blade and strut loading. The hydrodynamic inputs were generated using DMS and CFD models, which were combined with the application of centrifugal and gravitational forces to form structural analysis models using beam theory and FEA. Characterization of maximum stresses and deflection levels and their relationships with blade azimuth angle were performed. This work also sought to determine whether straight or helical-bladed turbines are more suited to generate ocean power from both hydrodynamics and structural perspectives.

7.2 Turbine Geometry

Two vertical axis turbine designs were simulated to evaluate the influence of variations of blade helicity on turbine structural loading characteristics. These models differed only in blade helicity as shown in Figure 7.1, with all common geometrical dimensions outlined in Table 7.1. Only two designs were considered: a straight-bladed turbine and a helical turbine with 15° of blade overlap. These were chosen as previous studies demonstrated that power output reduced significantly as blade overlap increased above 15° (Marsh et al. 2015*a*), reducing turbine utility for power generation. The geometrical layout of the straight-bladed turbine was based on an EFD turbine from literature to allow for validation of the numerical simulation techniques utilised (Marsh et al. 2015*a*, Rawlings 2008). The helical turbine used the same frontal area, strut geometry, blade chord, and blade section to allow comparisons between the two designs. Both turbines had two struts per blade located at the blade tips.

Table 7.1: Shared Geometry of the Straight and Helical Turbines

Geometry	Dimensions
Number of blades	3
Turbine height	0.6858m
Blade section	NACA634021
Blade chord	0.065m
Blade overlap	0°
Radius	0.457m
Strut section	NACA0012
Strut chord	0.065m
Number of struts per blade	2
Shaft diameter	0.048m

7.3 Numerical Simulation Methods

Three loading simulation models were developed allowing for comparisons of the respective benefits of each numerical simulation technique. The simulation models were performed in two steps, first the hydrodynamics followed by the structural simulations. The models developed were the:

- DMS-Beam, DMS blade forces combined with a beam theory model;
- CFD-Beam, CFD blade forces combined with a beam theory model; and
- CFD-FEA, CFD model coupled to the FEA model using pressure mapping techniques.

7.3.1 Hydrodynamic Simulations

Numerical simulations of the hydrodynamic forces were performed using DMS and CFD simulation models. For both models, force coefficients normal to the blade chord were determined, with the forces non-dimensionalised by dynamic pressure and blade chord. The CFD model was also used to output surface pressure data for use with the coupled CFD-FEA model.

Double Multiple Streamtube (DMS) Model

The normal blade force coefficients were modeled using a DMS model previously developed by the authors based on the methods outlined by Paraschivoiu (Marsh et al. 2013, Paraschivoiu 2002) and in Chpater 4. The turbine was modeled using a double actuator

disk method to account for reductions in flow velocity through the streamtube from V_1 to V_2 as shown in Figure 7.2. Using iterative methods upstream and downstream, induction factors were calculated from which blade angles of attack were determined. Once the latter were known, the forces normal to the blade chord were determined using lift and drag data obtained using the viscous airfoil analysis tool Xfoil (Drela 1989). As NACA634021 data was not readily available, NACA634221 data was used as it was similar in profile. The DMS model included dynamic stall modeling using the Gormont method to simulate the influence of the variations in blade angles of attack generated by the rotation of the blades (Masson et al. 1998). Currently the DMS model developed by the authors cannot model helical turbines, as the hydrodynamic influence of the blade inclination has not been adequately accounted for.

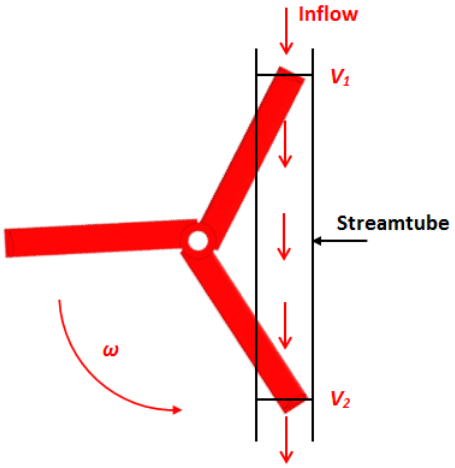

Figure 7.2: DMS model showing an example of the streamtube method for calculation of upstream and downstream flow velocity values V_1 and V_2

The DMS model developed was previously validated with EFD testing from literature for a one and three-bladed turbine configuration in Chapter 4 and (Strickland et al. 1979, Webster 1978). The azimuth angle of the maximum normal force was predicted accurately; however its value was under predicted on average by 40% as a result of severe dynamic stall effects that the Gormont model was unable to satisfactorily capture as shown in Chapter 4. This may be exacerbated due to severe dynamic stall caused by the thin blade section used. It is expected that the application of the Gormont model to the NACA634021 section modeled here will result in increased maximum force prediction accuracy, due to the reduction in the severity of dynamic stall demonstrated by thick blade sections (Choudhry et al. 2014).

Computational Fluid Dynamics (CFD) Models

Turbine blade forces were simulated using transient time-accurate 3D CFD models using ANSYS CFX (ANSYS 2010*a*, Marsh et al. 2015*b*), which solved the incompressible fully turbulent URANS equations using an element-based finite volume method. All turbine models were meshed using unstructured tetrahedral elements using ANSYS CFX 13.0 (ANSYS 2010*a*, Marsh et al. 2015*b*). Mesh resolution was set by specifying the mesh size and growth rates to allow for local refinement of mesh zones, with inflation layers used on all surfaces to fully resolve the surface boundary layer flow (ANSYS 2010*a*, Marsh et al. 2015*b*). Turbine rotation was simulated by enclosing the turbine in an inner domain as shown in Figure 7.3 that was rotated using the CFX transient rotor-stator model at the desired rotational rate. The interface between the stationary and rotating domains was modeled using a General Grid Interface (GGI) over which flow values are calculated using an intersection algorithm (ANSYS 2010*a*, Marsh et al. 2015*b*).

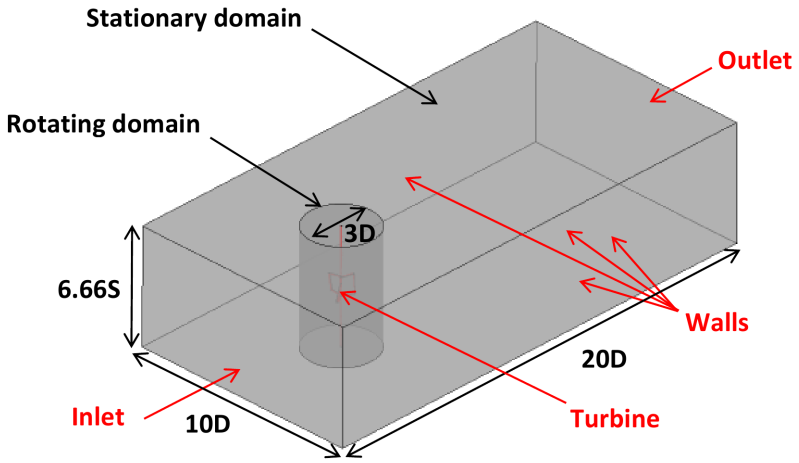

Figure 7.3: Simulation domain boundary nomenclature and sizing used for straight and helical CFD models. Dimensions in relation to turbine diameter, D, and height, S, as shared by the two turbine designs

The computational domains shown in Figure 7.3 were generated to simulate free stream conditions, with all corresponding boundary conditions outlined in Table 7.2. To ensure that the turbines were isolated from any domain wall effects and to allow for full wake development, systematic domain size studies were performed (Marsh et al. 2014, 2015*a*,*b*). All turbines were assumed to operate at sufficient depth to minimise any free surface interaction effects, and thus only the water phase was modeled.

Table 7.2: Boundary Conditions for the Straight and Helical Turbines

Boundary	Condition
Inlet	Uniform flow: 1.5 ms^{-1}
Inlet	5% turbulence
Outlet	Relative pressure: 0 Pa
Walls	Free slip walls
Turbine	No slip walls

The $k-\omega$ SST turbulence model was utilised for turbulence closure due to its ability to accurately model both free stream and boundary layer regions as well as offering improved prediction of flow separation and adverse pressure gradients by the inclusion of transport effects into the formulation of the eddy-viscosity (Menter 1994), with the $k-\omega$ SST CFD turbulence model commonly used for vertical axis turbine simulations (Castelli et al. 2010, Dai & Lam 2009, Gretton 2009, Lain & Osorio 2010, Marsh et al. 2012, 2013, 2014, 2015*b*, Malipeddi & Chatterjee 2012). To ensure numerical accuracy and stability, all simulations were performed using a high order advection and second order transient scheme (ANSYS 2010*a*). Convergence was deemed achieved when solution residuals reduced to below 10^{-4} and reduced by more than three orders of magnitude.

Studies of the influence of factors including mesh density, time step size, $y+$, domain length, width and height were conducted. Independence was deemed satisfactory when significant increases in these parameters resulted in C_p differences between successive refinements trending to less than 5% (Tu et al. 2013). This resulted in a suitable balance between solution accuracy and computational effort. Full mesh convergence studies were conducted by the authors for the straight and helical-bladed turbine simulated in this work and were presented previously in (Marsh et al. 2013, 2014, 2015*b*).

Validation of CFD methods against EFD testing of a one and three-bladed turbine from literature revealed good agreement for force coefficient predictions as outlined in Chpater 4. Maximum normal and tangential force coefficients were predicted on average to within 5.7% of EFD (Strickland et al. 1979, Webster 1978), with the relationship with rotational angle replicated accurately. Additionally, considerable validation of CFD power output was performed on both straight and helical-bladed turbines of similar design using EFD results from literature, with maximum power output predicted to within 14.3% and 6.3% of EFD results for each turbine respectively (Marsh et al. 2014, 2015*a*,*b*, Rawlings 2008).

7.3.2 Structural Simulations

Two numerical simulation models were utilised to characterise turbine loading characteristics; beam theory and FEA models. These models used either force or pressure field results from the DMS and CFD models.

Beam Theory Model

A beam theory model was developed using code scripted in Matlab. Three key assumptions were made to allow the use of this approach. The normal force was assumed to be uniformly distributed to simplify the coupling between the hydrodynamic and structural models, although the actual force distribution may be reduce near the tips of the blades due to blade end and blade-strut interaction effects. The normal force was also assumed to contribute the most to blade stress and deflection, as normal forces are on average an order of magnitude greater than the tangential forces (Paraschivoiu 2002). The normal force also acts in the direction normal to the blade chord line, resulting in large bending moments when compared to the small bending moments caused by the tangential forces. The blades were also assumed to be simply supported at each end, resulting in the assumption that the stress at the blade ends were zero as beam models were unable to model the stress at the blade-strut joints due to the geometrical layout of vertical axis turbines. The beam theory models were developed to establish their accuracy when compared to CFD-FEA models in the simulation of blade stress and deflection as they require considerably less computational requirements and solutions times.

To calculate the blade stress and deflection, first the normal force coefficients are determined using the DMS or the CFD models. The forces determined are then transformed into a uniformly distributed load across the span of the blade. The centrifugal force F_c caused by the turbine rotation is found as,

$$F_c = m\omega^2 r \tag{7.1}$$

where m is the blade mass, ω is the rotational rate, and r is the turbine radius. The total distributed load, w, acting on the blade span is the sum of hydrodynamic and centrifugal forces calculated. Using this total load, the bending moment, M_b is calculated using simple beam theory, where the bending moment is obtained as,

$$M_b = \frac{wl_e^2}{8} \tag{7.2}$$

where l_e is the blade span. The maximum stress, σ, is determined using,

$$\sigma = \frac{My}{I} \tag{7.3}$$

where y is half the maximum blade thickness, and I is the area moment of inertia determined using a simple approximations for hydrofoil sections (*Area and Bending Inertia of Airfoil Sections* 2015) given by,

$$I = K_1 c^4 t(t^2 + \epsilon^2) \tag{7.4}$$

where K_1 is a derived proportional coefficient based on values of area and bending inertia for common hydrofoil sections, c is the blade chord, t is the blade thickness, and ϵ is the camber percentage. The blade deflection is calculated using,

$$Deflection = \frac{5wl_e^4}{384EI} \tag{7.5}$$

where E is the material modulus of elasticity.

Structural Finite Element Analysis (FEA) Model

The stress and deflection on turbine blades and struts were evaluated using the ANSYS FEA linear Static Structural analysis module (ANSYS 2013). Although the loading and structural response conditions were quasi-static, inertia and gravitational loads were included to model the steady inertial loads, with the loading shown in Figure 7.4. The hydrodynamic forces on the blades were calculated by the CFD models and mapped on to the structural model surfaces using Octree mapping (ANSYS 2013). The FEA model was constrained at the shaft and hubs to allow for evaluation of the blade and strut forces, reducing computational effort. The von Mises stress and total blade deflections were calculated at each turbine azimuth angle using a custom Python script written by the authors. This script loaded the surface pressure fields from the CFD transient analysis for each time step, enabling a one-way Fluid Structure Interaction (FSI) simulation, as any deflections calculated were not reverted back to the CFD model. Two-way FSI techniques were examined, however due to their excessive simulation time they were not considered feasible, unless mesh element count was reduced which would adversely affect the accuracy of the hydrodynamic simulations. The simulated

turbines were constructed from steel with all material properties shown in Table 7.3.

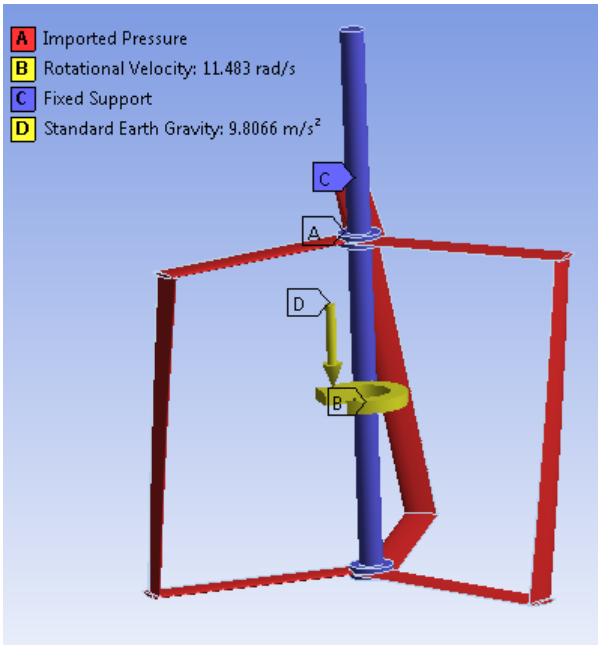

Figure 7.4: ANSYS structural model of helical turbine showing loading conditions including imported pressures, rotational velocity, gravity, and the fixed supports

Table 7.3: Material Properties used for Straight-bladed and Helical Turbine Structural Analysis

Material	Steel
Density (kg/m3)	7850
Tensile Yield Strength (MPa)	250
Compressive Yield Strength (MPa)	250
Ultimate Tensile Strength (MPa)	460
Youngs Modulus E (GPa)	200

The geometry of the FEA turbines was identical to that used in the CFD models, except for the addition of fillets at the blade-strut joints. Fillets of 0.0025m radius were added to avoid infinite or singular stress concentrations at the re-entrant corners of the joints. These can occur as forces applied to mesh cells of reducing size at the fillets will result in ever-increasing stress predictions as the mesh area reduces. To ensure that the addition of fillets did not influence simulation accuracy, maximum von Mises stress magnitudes were determined using CFD models with and without fillets. Variations of maximum stress of less than 1.5% were determined, allowing the use of de-featured CFD models to increase computational efficiency.

Mesh convergence studies were performed to verify all FEA meshing techniques utilised, with independence studies for maximum and minimum mesh sizing, face sizing refinement, growth rate, and curvature angle performed. Mesh convergence found to be highly dependent on the face sizing of the fillets between the blades and strut joints where the maximum stress magnitudes were located. Successive mesh refinement demonstrated mesh element count independence at 143,000 elements.

7.4 Results and Discussion

The loading characteristics of straight and helical-bladed turbines were investigated using the DMS-Beam, CFD-Beam, and CFD-FEA models. For each model, stress levels and total blade deflections were recorded over one rotation. All results were simulated at an inflow velocity of 1.5 ms^{-1}. Simulations of turbine loading characteristics were performed for three rotational rates representative of common turbine operational ranges corresponding to a rotational rate of:

- λ=1.5 similar to that found when starting the turbine;
- λ=2.75 corresponding to the maximum power output; and
- λ=3.5 representing an over speed condition.

where λ is the tip speed ratio defined as,

$$\lambda = \frac{rw}{V} \tag{7.6}$$

where V is the inflow velocity.

7.4.1 Normal and Tangential Force Coefficients

Using the DMS and CFD models, the normal force coefficients for the straight three-bladed turbine shown in Figure 7.1 were obtained at λ=1.5, 2.75, and 3.5 as shown in Figure 7.5. For λ=1.5 agreement between the two numerical methods was very good, with both the relationships with azimuth angle and the normal force coefficient magnitudes for each model agreeing closely. The maximum force coefficients were found to occur at approximately -22.5° by both numerical models, with the definition of rotational angle shown in Figure 7.1.

This was due to peaks in the lift generated by the favorable angle of attack over the blades and dynamic stall effects at this azimuth angle. Differences in maximum force of 8.5% were determined between the two models, which may be attributed to differences in dynamic stall modeling, as these differences were found around the force coefficient peaks. The normal force coefficients in the downstream region from 90° to 270° were not fully reversed when compared to the upstream region, as a result of reductions in the flow velocity over the downstream blades caused by the preceding blades wake. Large reductions in force in the downstream region were previously found in EFD and CFD studies in Chapter 4, with force magnitudes of less than 1/3 found when comparing peak values with average values in the downstream region (Strickland et al. 1979, Webster 1978).

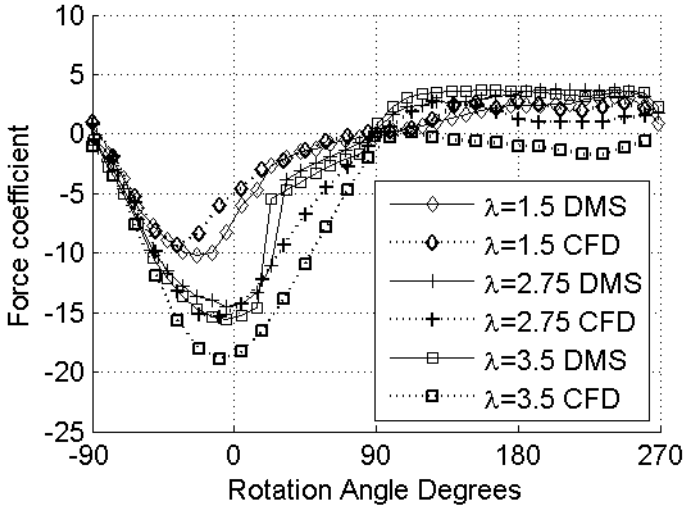

Figure 7.5: Straight-bladed turbine normal force coefficient simulations for one revolution using the DMS and CFD models at λ=1.5, 2.75, and 3.5

Figure 7.5 also compares simulations of normal force coefficients using the DMS and CFD models at λ=2.75. Maximum force coefficient predictions for both models at λ=2.75 were within 7.3% of each other, with the location of the maximum force predicted at the same azimuth angle for both models. Although the shape of the simulated normal force coefficient curves was similar, predictions of normal force coefficient diverged in the downstream region around 180°. The DMS model accounted for reductions in flow velocity in the downstream region, but it did not account for the increased levels of turbulent flow over the downstream blades, which reduces lift and hence normal force coefficients. However, these turbulent flow effects were simulated by the CFD model, resulting in discrepancies between the two models in the wake-influenced downstream regions. The jump in force coefficient around 22.5° to

45° was caused by jumps in the lift and drag tables used in the DMS model, as well as the by the rapid reduction in the additional lift determined by the dynamic stall model.

Figure 7.5 also shows the normal force simulations at λ=3.5 as determined using the DMS-Beam and CFD-Beam models. The predicted azimuth location of maximum force coefficients agreed well, however reduced correspondence was found when comparing maximum force coefficient values predictions, which were within 21% of each other. This reduction in force coefficient similarities between the numerical models when compared to the λ=1.5 and 2.75 results may be due to the over prediction of the increasing influence of strut drag on the turbine as λ increases by the DMS model. Similar to the simulations of normal force coefficient at λ=1.5 and 2.75, differences in the downstream region between the CFD and DMS model were apparent.

7.4.2 Straight-Bladed Turbine Loading and Deflection Simulations

Figure 7.6 compares von Mises blade stress and deflection levels at λ=1.5 for the DMS-Beam, CFD-Beam, and CFD-FEA models. The CFD-FEA blade results ignored the stress concentrations at the blade-strut joints, allowing comparison between the simulation models. The highest blade stress and deflection levels were found around -22.5° coinciding with the peaks in the normal force coefficients shown in Figure 7.5. Similarities across all λ were found between the three simulation models, with the location of maximum stress and deflection found at the middle of the blade span. The maximum stress and total deflection results determined using the DMS-Beam and CFD-Beam models were within 8.4% of each other, as they were calculated using similar values of normal force coefficient as shown in Figure 7.5. At high absolute values of force coefficients the DMS-Beam and CFD-Beam results diverged from the CFD-FEA simulations due to differences in the structural support conditions at the blade ends. In the CFD model the deflection of the struts reduced the blade stress levels, whereas the beam theory models assumed that the blade was simply supported, resulting in increased stress levels. The stress on the blades was cyclic; however it is not fully reversed, with reduced levels found in the downstream region around 180°.

The rapid change in deflection shown in Figure 7.6 at rotational angles around 45° was due to the rapid changing of the blade angle of attack as well as strut deflection and gravity effects. At 0° the blade was deflected inwards, with the maximum deflection occurring near the middle of the turbine blade. As the blade continued to rotate it started to deflect out-

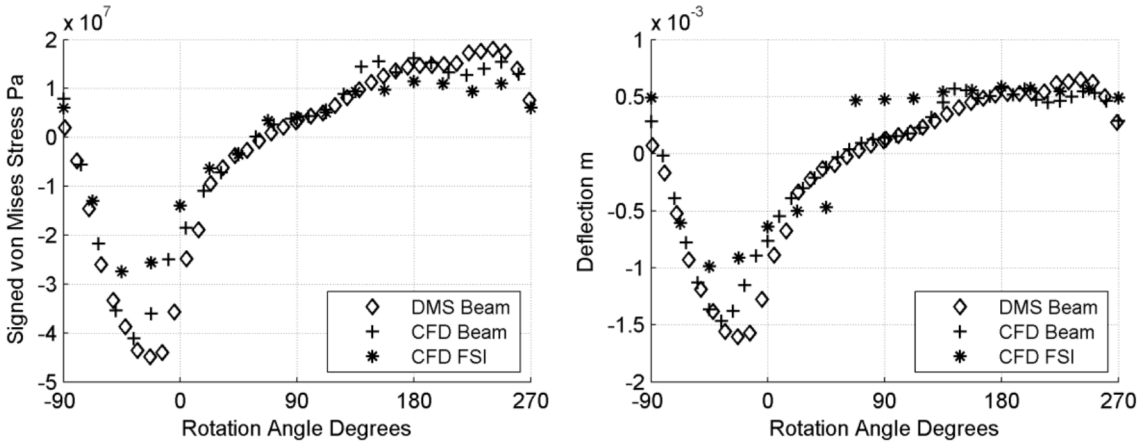

Figure 7.6: Signed maximum von Mises blade stress and total deflection comparisons for the DMS-Beam, CFD-Beam, and CFD-FEA straight-bladed turbine models at λ=1.5. Positive deflection is outwards away from the shaft

wards, however the strut deflection at the blade-strut joints did not change significantly due to the low hydrodynamic and centrifugal force magnitudes. This caused a rapid change in both the magnitude and location of the blade deflection as shown in Figure 7.7; where the location of the maximum deflection can be seen to move down then back up again to the center span location as the hydrodynamic force increased as shown in Figure 7.5. However, this change in location of the maximum stress and deflection was not significant, as the stress and deflection levels are low compared to the maximum values found around -22.5°. This effect was not found at higher λ.

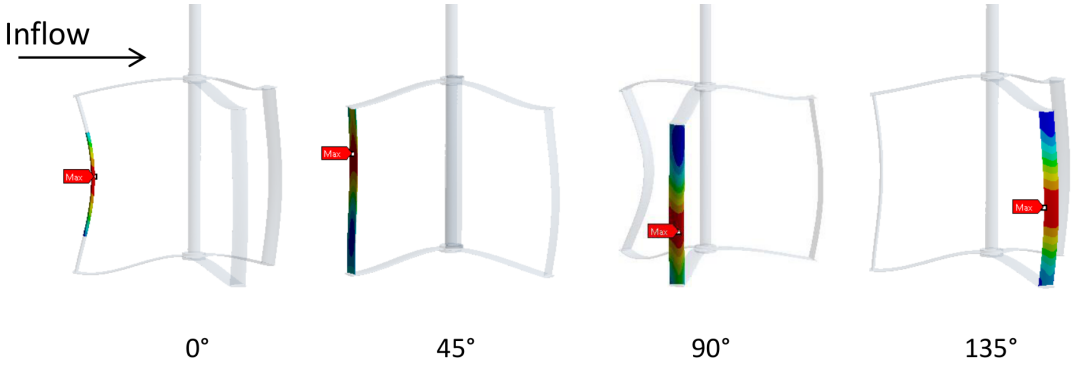

Figure 7.7: Change in location of maximum blade stress and deflection between 0° and 135° found by CFD-FEA straight-bladed turbine model at λ=1.5. The location of the maximum stress and deflection is shown by the red label

Comparisons of blade von Mises blade stress and deflection at λ=2.75 are shown in Figure 7.8. The three simulation model curves prescribe similar stress and deflection curves, with maximum values located at the middle of the blade span. The highest stress and blade deflection was found at approximately 0°, with peak stress loads increased on average by 45% when compared to the λ=1.5 case. This increase in stress was caused by increases in blade lift due to the blade angle of attack variations reducing to more favorable levels below stall as λ increased (Paraschivoiu 2002). Similar to that found at λ=1.5, the DMS-Beam and CFD-Beam models differed in maximum stress level prediction from the CFD-FEA model, as a result of the blade end support conditions. The von Mises stresses were not fully reversed, due to reductions in flow velocity and increased flow turbulence generated by the wake of the upstream blades. The DMS model predicted higher stress and deflection levels in the downstream regions, as it was unable to simulate the influence of this upstream blade vortex shedding on the downstream blades.

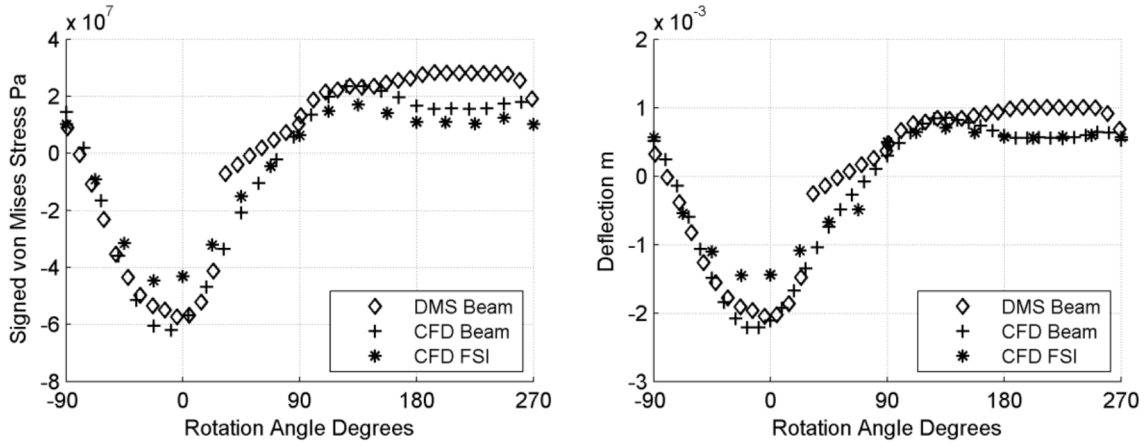

Figure 7.8: Signed von Mises blade stress and total deflection comparisons for the DMS-Beam, CFD-Beam, and CFD-FEA straight-bladed turbine models at λ=2.75. Positive deflection is outwards away from the shaft

Figure 7.9 shows the simulated von Mises blade stress and total deflection at λ=3.5, with the maximum values located at the middle of the blade span. The maximum stresses were found at approximately 0°, as a result of peaks in normal force coefficient in the upstream region as shown in Figure 7.5. Peak stress values were found to increase on average by 10.6% when compared to the λ=2.75 case. This increase was less than that found between λ=1.5 and 2.75, as the increase in λ resulted in increased centrifugal forces on the blades which oppose the hydrodynamic forces in the upstream direction. Similar to results in Figures 7.6 and 7.8, the maximum stress levels simulated by the CFD-FEA model were reduced when

compared to the DMS-Beam and CFD-Beam Theory models, as a result of the differences in the blade end support conditions. The DMS-Beam downstream stress and deflection magnitudes differed from the CFD-Beam and CFD-FEA models due to differences in normal forces coefficient simulated by the DMS model when compared to the CFD simulations, similar to that found at λ=2.75.

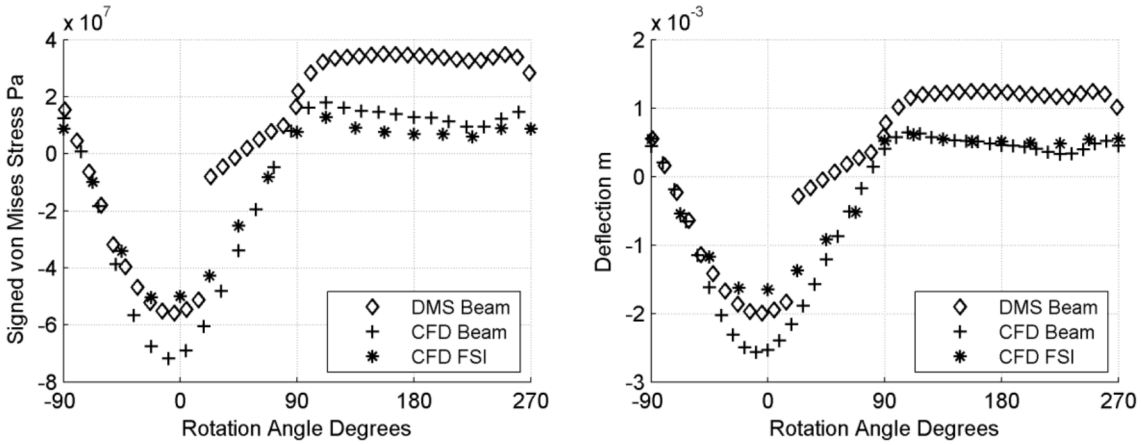

Figure 7.9: Signed von Mises blade stress and deflection comparisons for the DMS-Beam, CFD-Beam, and CFD-FEA straight-bladed turbine models at λ=3.5. Positive deflection is outwards away from the shaft

For all simulation models, the highest magnitude of the blade deflection versus blade span was 0.4%. The small blade deflections found would have minimal impact on the lift and drag generated over the blade, allowing one-way FSI models to be used. However, if the turbine was constructed from a more flexible material with a lower modulus of elasticity, these deflection levels would be much higher as a percentage of the blade span, possibly requiring a two-way FSI approach.

Figure 7.10 illustrates strut and blade deflection over one rotation using the CFD-FEA model. The blades can be seen to deflect inwards between the rotational angles of -90° to 45°, after which they deflected outwards for the rest of the rotational cycle. This cyclic pattern repeats over each revolution, generating tension and compression cycles on the blades. The struts can also be seen to deflect with the blades, particular at the blade-strut joints.

The centrifugal forces generated by the turbine's rotation opposed the hydrodynamic forces in the upstream region from approximately -90° to 90°, reducing blade stress and deflection

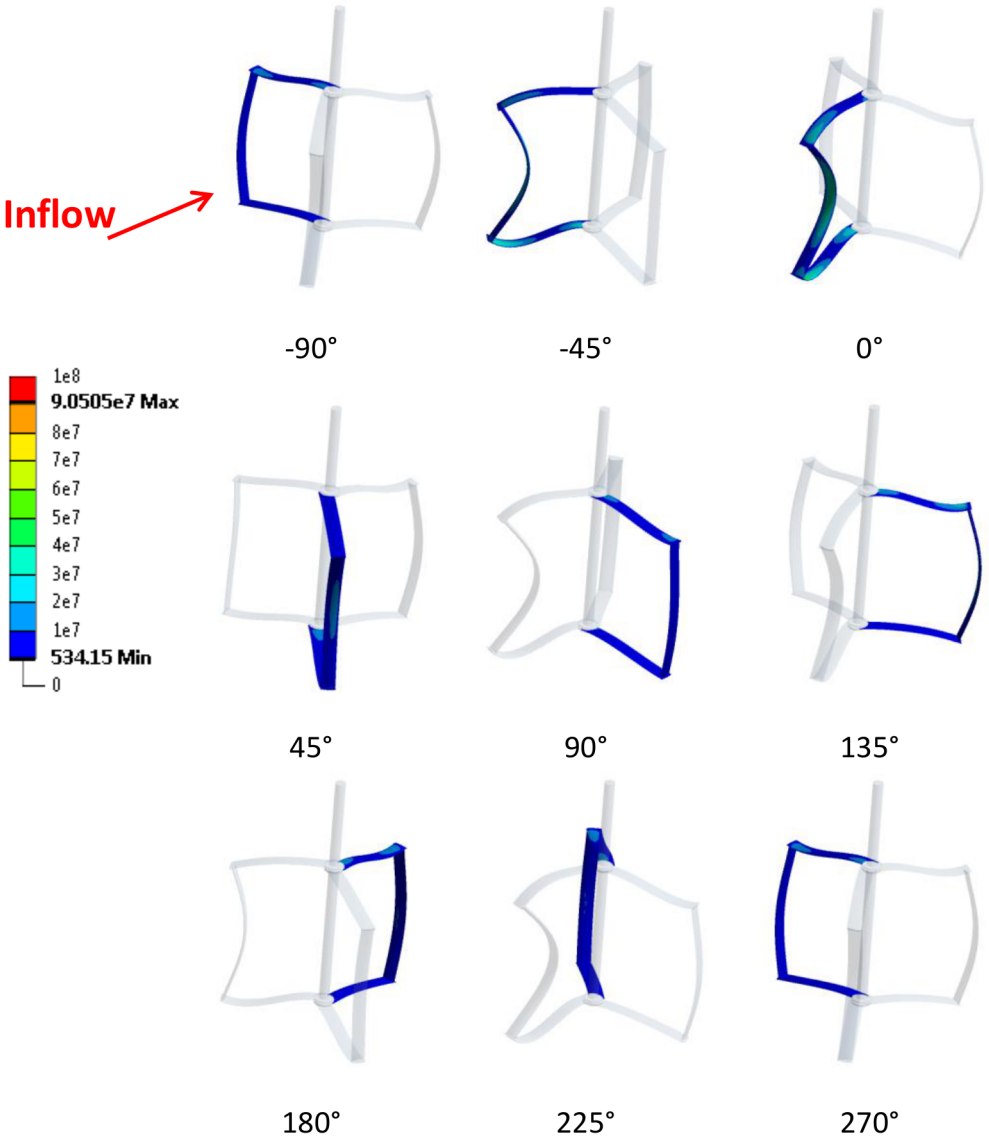

Figure 7.10: Turbine von Mises stress magnitudes in Pa for one turbine rotation at λ=2.75. Deflection scale increased by 150 to highlight structural deformation

levels, whereas in the downstream region from 90° to 270° the hydrodynamic and centrifugal forces combined. However, the hydrodynamic normal blade forces in the downstream region were significantly reduced when compared to upstream normal force values as shown in Figure 7.5, due to the reduction in flow velocity in the downstream region and the turbulent flow effects of the preceding blades wake. Thus, the combined downstream total hydrodynamic and centrifugal forces and hence blade stress and deflections were reduced when compared to upstream values. For the turbines studied here the hydrodynamic force was dominant, with upstream force magnitudes and hence blade stress and deflection levels higher than downstream values for all λ simulated.

The CFD-FEA model was then used to predict the maximum stress magnitudes within the blades and the struts. The maximum stress was found to occur at the bottom blade-strut joint for all λ, as a result of the combination of hydrodynamic and gravitational loading, with levels significantly higher than blade stress levels shown in Figures 7.6, 7.8 and 7.9. An example at λ=2.75 is shown in Figure 7.11, with results in Figure 7.12 showing the maximum stress relationships with azimuth angle for each λ simulated. The maximum stress occurred at approximately 0° at the bottom blade-strut joint, as the maximum normal force occurs at this azimuth angle as shown in Figure 7.5. These normal force peaks generated large bending moments, and hence large stress concentration at the blade-strut joints, with peak magnitudes of approximately 101 MPa noted. The use of beam theory models will not resolve this depending on the location of the strut on the blades.

Comparison of yield safety factors are shown in Figure 7.13, where the yield safety factor was defined as the ratio of the material yield stress shown in Table 7.3 to the maximum stress. For each λ, the maximum stress levels were below the material yield strength, with minimum safety factors of 3.84, 2.76, and 2.49 found for λ=1.5, 2.75, and 3.5. However, the analysis of yield safety factors does not take into consideration any fatigue issues as a result of the cyclical loading. If the tidal velocity distribution is known, the models developed here can be used to determine the fatigue life of turbine using rainflow counting methods combined with Miners cumulative damage rule for lifetime calculations (Veers 1981).

7.4.3 Helical Turbine Normal Force Coefficients

Using the CFD model, the normal blade coefficients were determined for the helical turbine at λ=1.5, 2.75, and 3.5 as shown in Figure 7.14. Similar to the coefficient curves deter-

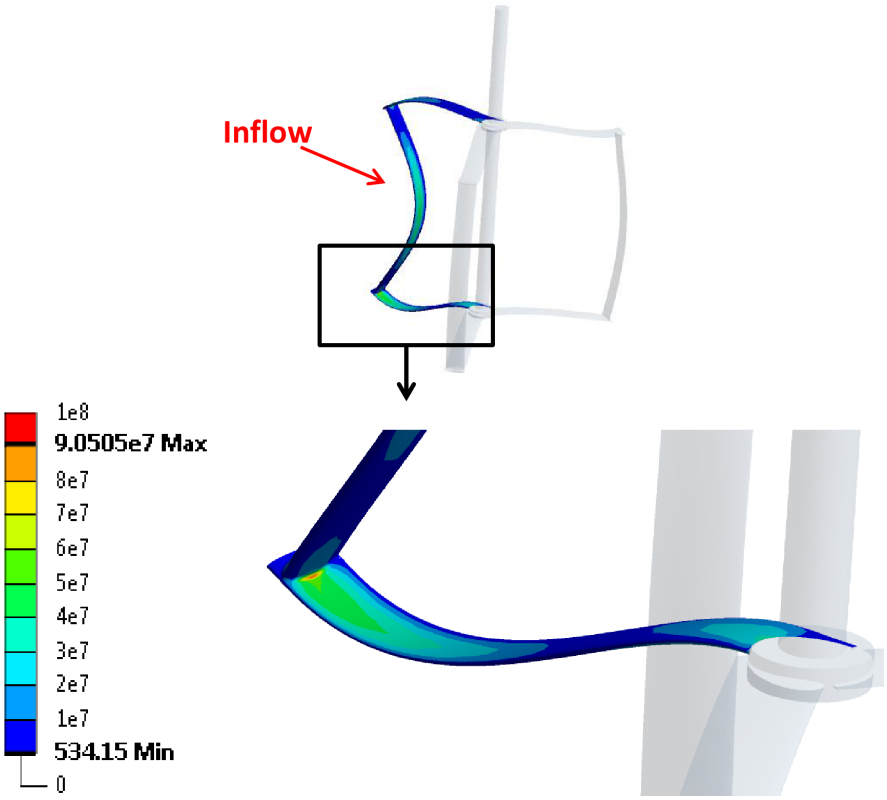

Figure 7.11: Stress concentration in Pa at bottom blade-strut fillet showing the location of maximum von Mises Stress of 90.51 MPa at the azimuth angle of 0° at λ=2.75

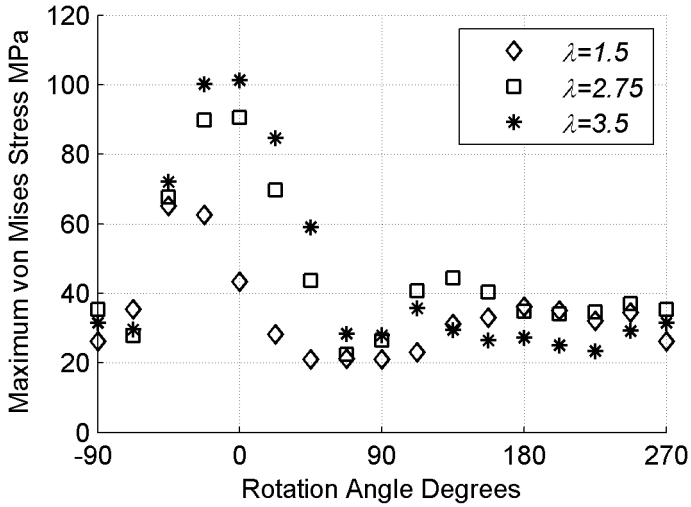

Figure 7.12: Maximum von Mises Stress at the bottom blade-strut fillet over one revolution determined using the straight-bladed CFD-FEA turbine model at λ=1.5, 2.75, and 3.5

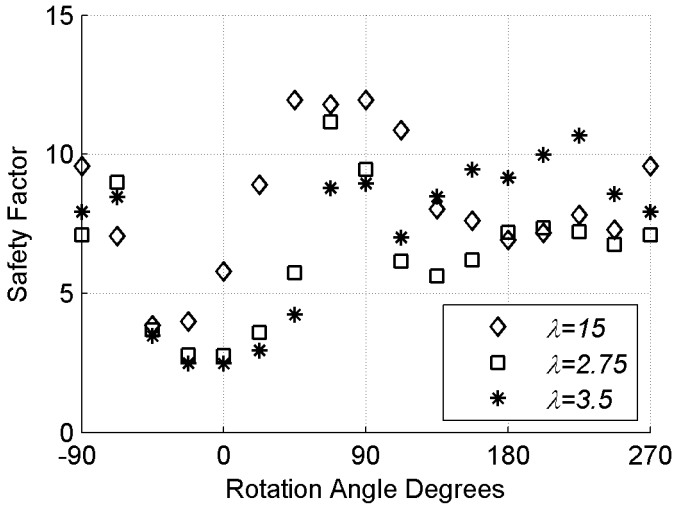

Figure 7.13: Yield safety factor for the straight-bladed CFD-FEA simulation results for one revolution at λ=1.5, 2.75, and 3.5

mined for the straight-bladed turbine shown in Figure 7.5, maximum force was found at approximately -45° to -22.5°, due to peaks in the lift generated by the favorable angle of attack over the blades and dynamic stall. The normal force coefficients in the downstream region from 90° to 270° were not fully reversed when compared to the upstream region, as a result of reductions in the flow velocity over the downstream blades and blade wake effects.

The normal force coefficients for the helical turbine shown in Figure 7.14 were reduced when compared to the values found for the straight-bladed turbine shown in Figure 7.5. The reduction in maximum normal force coefficients resulted as the angle of attack over the blades varies along the blade span resulting in varying force coefficients. This variation is caused by the helical distribution of the blade around the rotational axis, and as a result the blade does not generate lift force peaks simultaneously along its full length as it rotates in the upstream section at azimuth angles from -90° to 0°.

7.4.4 Helical Turbine Loading and Deflection

Figure 7.15 shows the helical turbine von Mises blade stress magnitudes and deflection using the CFD-FEA analysis model. These results focused on the blades and ignored the stress concentrations at the blade-strut joints to allow for comparison with the blade force simu-

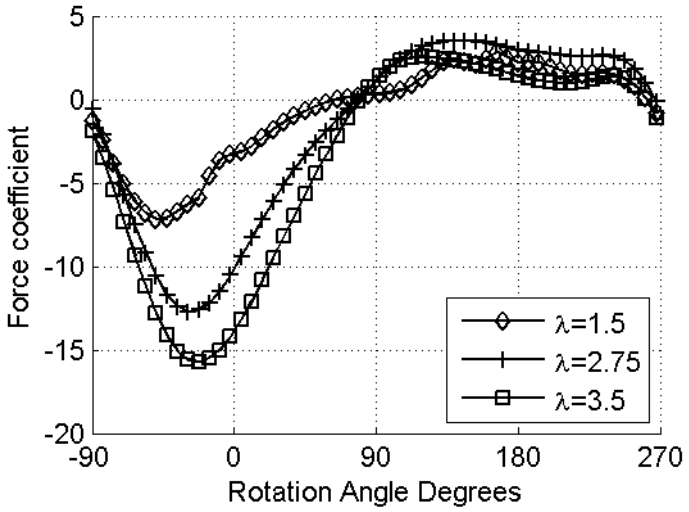

Figure 7.14: Normal force coefficient simulations for one revolution for the helical CFD model at λ=1.5, 2.75, and 3.5

lations shown in Figures 7.6, 7.8, and 7.9. Peaks in stress and total deflection occurred for all λ at approximately -45° to -22.5°, with the blades deflected inwards by up to 0.0014 m. In the downstream region the blade deflected outwards, however the stress magnitudes were not fully reversed. This was due to reductions in flow velocity through the turbine, and the shedding of vortices from the upstream blades, which generated turbulence over the downstream blades thereby reducing their hydrodynamic efficiency. The helical blade stress and deflection levels were reduced when compared to the straight-bladed turbine results shown in Figures 7.6, 7.8 and 7.9 as the normal force coefficient levels were lower, shown when comparing CFD force predictions in Figures 7.5 and 7.14.

Figure 7.16 compares the blade and strut maximum von Mises stress magnitudes at λ=1.5, 2.75, and 3.5. Similar to the straight-bladed turbine results shown in Figure 7.11, stress peaks occurred at the bottom blade-strut joint due to the combination of hydrodynamic and gravitational forces. Peaks in maximum stress levels were found to occur at azimuth angle of -45° to -22.5°, due to the peaks in normal force generated by the blade in the upstream regions. Downstream maximum stress levels were half that of the upstream values, due to reductions in flow velocity caused by the wake of the preceding blades. If the tidal velocity distribution is known, the models developed here can be used to determine the fatigue life of turbine using rainflow counting methods combined with Miners rule for lifetime calculations (Veers 1981).

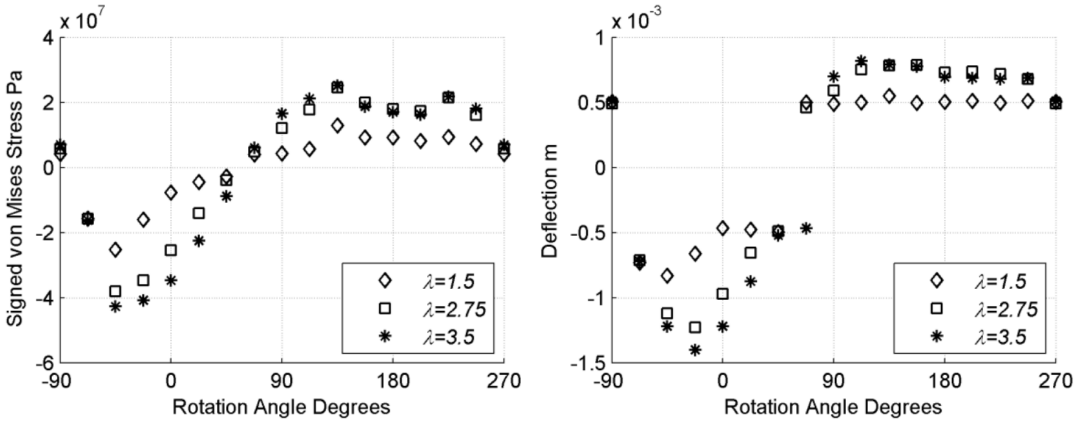

Figure 7.15: Helical turbine signed von Mises blade stress and deflection comparisons found using CFD-FEA models at λ=1.5, 2.75, and 3.5. Positive deflection is outwards away from the shaft

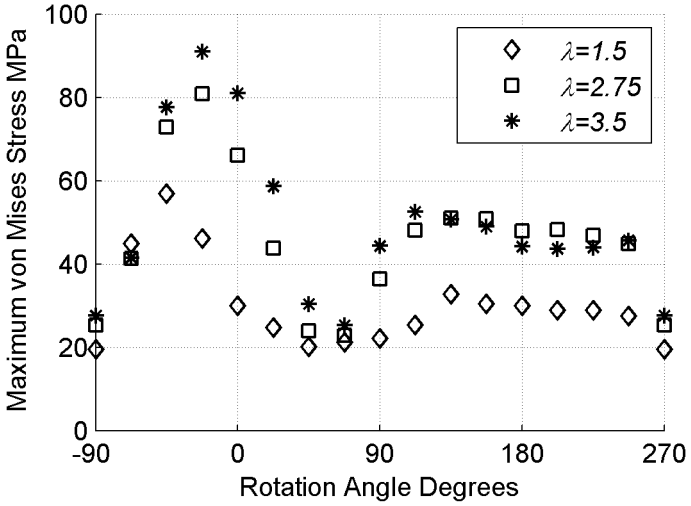

Figure 7.16: Maximum helical-bladed turbine von Mises stress levels comparing λ=1.5, 2.75, and 3.5

7.4.5 Straight and Helical Bladed Turbine Loading Comparisons

Comparisons of maximum von Mises stress levels for the straight and helical turbines are shown in Figure 7.17. For all λ, the straight-bladed turbine maximum stress levels were approximately 12.9% higher than for the helical turbine values. The straight-bladed turbine stress peaks were higher as the blade generates peaks in lift along its full length simultaneously, whereas the helical turbine blade lift peaks occur along the blade span at differing rotational angles due to the blades distribution around the rotational axis. The decrease in maximum stress levels found for the helical turbine reduces blade bending moments when compared to the straight-bladed turbine. In addition, the distribution of the helical blades around the rotational axis is better suited to resist bending when compared to the straight blades. Similarly, the blade stress and deflection levels of the helical-bladed turbines were lower than that of the straight-bladed turbines for all λ.

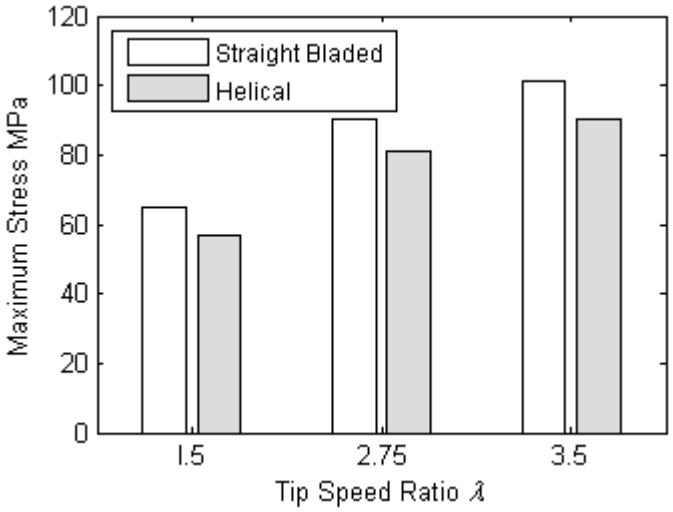

Figure 7.17: Comparisons of the maximum von Mises Stress magnitudes determined using the CFD-FEA models for the straight and helical turbine models at λ=1.5, 2.75, and 3.5

For ocean and tidal power installations, the authors suggest that straight-bladed turbines are more suitable as they generate more power for the same frontal area (Marsh et al. 2015*a*), without any significant increase in stress levels as shown in Figure 7.17. These factors will increase installed power generation capacity while not reducing turbine longevity. Additionally, straight-bladed turbines are much simpler to manufacture than the curved blades of helical turbines, reducing blade manufacturing costs.

Although no EFD data was available to validate force coefficient simulations for the DMS and CFD models, close agreement between the two models provides some verification and gives confidence in the predicted results. Although the two numerical methods use different techniques, one based on EFD lift and drag data tables and the other on solutions to the Navier-Stokes equations, the normal force coefficient predictions found were on average within 12% of each other for all rotational rates. Combined with the previous validation of the DMS in Chapter 4 and (Marsh et al. 2013) and CFD (Marsh et al. 2013, 2014, 2015*a*,*b*) models, this high level of agreement gives confidence in the hydrodynamic simulation results presented in this paper. Additionally, although no validation data was available for the structural simulations, the level of agreement between the predicted blade stress and deflection results through the use of two separate structural analysis methods gives confidence in the results presented.

7.4.6 Computational Requirements

Significant differences in total simulation time and files sizes were required between simulation models as shown in Table 7.4. All numerical solutions were performed on an Intel i7 860 2.8 GHz based cluster with 2GB ram per core. The significant variations in simulation time suggest that the turbine design process should be performed in two stages. For initial geometrical design studies DMS-Beam models allow the quick estimation of normal forces, blade stress, and deflection levels; enabling the optimization of both power output and blade loading. However, the determination of maximum stress magnitudes as found at the blade-strut joints required the use of CFD-FEA models, as beam theory-based models were unable to resolve the blade-strut stresses.

Table 7.4: Computational Requirements for One Revolution of the Straight-Bladed Turbine at λ=2.75

Model	Hydrodynamic	Cores	Structural	Cores	File Size
DMS-Beam	1 minute	1	1 minute	1	1 Mb
CFD-Beam	2400 minutes	24	1 minute	1	80 Gb
CFD-FEA	2440 minutes	24	500 minutes	2	160 Gb

Simulations using coupled two-way FSI models were attempted, however they were not completed as it was estimated that the simulations would take around 140 days to complete one revolution, due to the combination of large CFD mesh element counts and reductions in numerical speed due to the coupling of the CFD and FEA models. This compared poorly with the one-way FSI simulations reported here, with total run times of less than 2 days.

7.5 Conclusions

Numerical evaluations of the hydrodynamic and structural loading of straight and helical-bladed turbines were performed using DMS, CFD, beam theory, and FEA methods. These simulations were performed at multiple rotational rates to characterise blade and strut loading. This study revealed three key findings:

- straight-bladed turbines exhibit 12.9% higher maximum stress and deflection levels than helical turbines;
- maximum stress levels were found at the bottom blade-strut joints for both straight and helical-bladed turbines; and
- maximum stress levels for straight and helical turbines were well below yield strength at an inflow velocity of 1.5 ms^{-1}.

Combined, the key outcomes listed above lead to an important finding; that straight-bladed turbines are better suited for ocean power than helical turbines, as they generate higher power output without any significant increases in blade loading.

The simulation models developed in this paper open up considerable possibilities to improve vertical axis turbine designs from both hydrodynamic and structural perspectives. Based on this work the following is recommended:

- investigate blade-strut joint designs using FEA to reduce maximum stress concentration levels; and
- conduct EFD using strain gauges to evaluate turbine loading characteristics and provide validation data for the models developed in this work.

Chapter 8

Summary, Conclusions and Future Work

8.1 Summary and Conclusions

This study set out to characterise and compare the hydrodynamic and structural loading characteristics of straight and helical-bladed vertical axis turbines, allowing the evaluation of their suitability for harnessing ocean kinetic energy. In this chapter, key findings are presented with conclusions and discussion of any limitations determined as part of this work. Recommendations for future work are also presented along with guidelines for numerical simulation.

Initial efforts outlined in Chapter 2 focused on the establishment, verification, and validation of CFD modelling techniques, including the influence of turbulence model selection and the influence of 2D and 3D domain model approaches on power output simulation accuracy. Chapter 3 continued this research on with a more in-depth analysis of transient URANS CFD simulations of straight-bladed turbines with two differing strut configurations. The DMS model, an alternate model to CFD, was presented in Chapters 4 and 5, with the results compared with EFD and CFD results to investigate straight-bladed turbine blade force and power output levels. The CFD techniques developed in Chapters 2 and 3 were subsequently used in Chapter 6 to determine the performance characteristics of helical turbines, with verification and validation performed against EFD from literature. These studies investigated the effect of blade helicity on performance parameters, with simulation results also compared to the straight-bladed turbine results outlined in Chapters 2 and 3. Finally in Chapter 7, FEA and Beam Theory structural analysis models were coupled with the CFD and DMS models outlined in Chapters 2 to 6, resulting in the development of numerical simulation models of the hydrodynamic and structural characteristics of straight and helical-bladed turbines. The development of these models allowed for comparisons of the relative merits of the two turbine configurations to be performed.

Comparisons were made between straight and helical-bladed turbines by evaluating the respective levels of power output, torque fluctuation, mounting force, blade stress, and deflection levels between the two geometrical layouts. These comparisons are important, as they allow for the determination of the most suitable turbine design, ensuring longevity and efficiency. This work specifically reports on efforts to answer the following question: "Are straight or helical-bladed vertical axis turbines more suited for ocean tidal and current power generation when evaluated using hydrodynamic and structural loading criteria?"

The aggregated approach to the work outlined in Chapters 2 to 7 arrived at the following key conclusion; straight-bladed, rather than helical-bladed turbines, are more suited for ocean tidal and current energy. Straight-bladed turbines generate higher power output than helical-bladed turbines of the same frontal area, without suffering any significant increases in blade and strut stress, torque fluctuations, or mounting force levels. This makes straight-bladed turbines better suited for ocean installation, as they will generate the highest energy output whilst not significantly reducing service life in comparison to comparable helical-bladed configurations. As most vertical axis turbines use similar blade profiles to those studied here, these results will hold for turbine with other hydrdynamic blade profiles.

This work also found that the numerical simulation models utilised in this work were able to accurately simulate vertical axis turbine parameters including power output and mounting force levels. This finding is important as in-depth determination of turbine performance and structural parameters can now be obtained before manufacture and installation, allowing the use of computational means to investigate and improve turbine geometrical layout and design.

As part of this work, numerical simulation guidelines for future use in determining turbine hydrodynamic and structural parameters, including power output and blade stress levels were developed. For initial design studies, the DMS and Beam Theory models are recommended, as they are computationally efficient allowing their use on stand-alone desktop computers with fast solution times. However, for more in-depth analysis, coupled CFD and FEA models should be utilised as they offer the ability to model the entire turbine structure. Combined, these simulation models form a multi-stage toolbox for turbine engineers to analyse and evaluate vertical axis turbine hydrodynamics and structural characteristics.

8.2 Findings and Limitations

The findings of this thesis were obtained by two methods; investigation into the influence of geometrical layout on performance and structural parameters, and evaluating the accuracy and suitability of the numerical methods chosen to perform these investigations. The following section summarises the key findings and limitations determined in Chapters 2 to 7, pointing towards the determination that straight-bladed turbines are more suited for ocean installations than helical-bladed turbines of the same frontal area.

8.2.1 Geometrical Findings

- Power output: Straight-bladed turbines were found to generate higher maximum power outputs than helical-bladed turbines of the same frontal area, as the inclination of the helical blades to the inflow was found to generate spanwise flow, reducing their hydrodynamic efficiency. Inclination of the blades past 15° was found to significantly reduce power output, making turbines with high degrees of blade helicity inefficient for power generation purposes.

- Maximum Stress levels: Straight-bladed turbines exhibited approximately 13% higher maximum stress than helical turbines for the same blade chord, section and turbine frontal area, with the highest stress found at the blade-strut joints. However, this increase was not significant, and for all turbines studied the stress levels determined were significantly less than the material yield strength limit, with the lowest safety factor obtained as 2.49.

- Torque fluctuations: Helical turbines exhibited reduced torque fluctuation levels when compared to straight-bladed turbines, with levels reducing as helicity increased. For the 15° helical turbine the reduction in maximum torque fluctuation level when compared to the straight-blade design was less than 16%. Significant reductions in torque fluctuation levels were determined for turbines with high levels of blade helicity; however this was accompanied by significant reductions in power output.

- Mounting forces: Blade helicity was found to reduce mounting force levels when compared to straight-bladed force values. However, the reduction in maximum mounting forces determined for the 15° helical turbine when compared to straight-bladed turbines was less than 7%.

8.2.2 Numerical Simulation Models Findings and Limitations

Computational Fluid Dynamics (CFD) Models

- Flow modelling using CFD: The CFD models were able to accurately model the influence of differences in geometrical configuration on power output and mounting forces, including variations of blade helicity, strut location, strut section, and blade-strut connection design, with results comparing favourable with EFD results published in literature for six different turbine designs. Greater understanding of turbine performance

was gained using flow visualisation made possible through the use of CFD models, providing key insights into vortex shedding and flow diffusion effects. Torque fluctuation levels were also determined using the CFD models. The CFD results obtained were found to be highly dependent upon modelling variables, making verification of the models, such as grid independence studies, vital to ensure confidence in the results obtained. Validation of the CFD models was also found to be essential given the complexity of the discretisation and modelling variables.

- URANS-based turbulence models: Studies of turbulence models found that the k-ω SST model resulted in the closest agreement of blade force and power output predictions with EFD for both straight and helical-bladed turbines. The use of transition models was found to offer increased power output simulation accuracy when compared to the fully turbulent models. However, this increase in accuracy, usually at high rotational rates, came at a considerable increase in computational cost.

- Computational Domain: Examination of 2D and 3D domain models revealed that simulations should be performed using all geometrical turbine features, including all blades, struts and shafts, necessitating a 3D approach. Simulations using 2D models were found to over predict turbine power output, as the influence of strut drag, spanwise flow, and blade end effects could not be accounted for.

- Mesh requirements: The accuracy of the CFD results was highly dependent upon grid resolution factors, and was influenced by the selection of turbulence model, mesh density, time step size, boundary layer thickness, and $y+$. The highest simulation accuracy when compared to EFD was found using 3D CFD models that included all geometrical features, allowing the simulation of complex hydrodynamic flow features such as tip losses and restive strut torque.

- Computational requirements: The k-ω SST models required on average 24 cores with 2Gb of memory per core, with solutions taking 20 hours for one revolution of the straight-bladed turbine. As the helical-bladed turbine models could not use symmetry to reduce the size of the computational domain, they required approximately twice the simulation time.

- Limitations of Study and/or Model: The computational power required to solve the CFD models was at times excessive. The simulations performed required considerable computational capacity, and could only be performed using a High Performance Cluster (HPC). Even with the availability of HPC, two-way FSI and laminar-to-turbulent

models were found to be excessively computationally demanding, with simulation times running into multiple months for one revolution at one rotational rate.

Double Multiple Streamtube (DMS) Models

- DMS model: The DMS model was able to accurately simulate turbine power output and blade forces, with results comparing favourably with EFD published in literature and the CFD results presented in this work, although some limitations in dynamic stall modeling were found. The accuracy of the DMS model resulted from the inclusion of correction factors for effects such as the resistive torque generated by strut drag and Reynolds number corrections.
- Computational Requirements: The DMS model was computationally efficient due to its formulation based on a double actuator-disk model. All DMS simulations were performed on a standalone desktop computer, with total run times of less than 1 minute. This was significantly lower than the run time required for equivalent CFD models.
- Limitations of Study and/or Model: The DMS model developed was unable to be utilised to model helical-bladed turbines, as the influence of the helical blade inclination to the inflow was not accounted for. The DMS model requires as input lift and drag data for the sections obtained either by numerical or EFD means; however this data may not be readily available for the blade and strut sections chosen, thus requiring numerical modelling such as CFD of the sections. DMS models are also unable to generate flow visualisation, unlike CFD models. For one turbine geometry studied the DMS simulations under predicted the influence of dynamic stall on turbine blade force magnitudes.

Beam Theory

- Beam Theory: Beam Theory models were able to determine blade stress and deflection levels, with results comparing favourably with FEA simulations. Beam theory models can also simulate blade loading for turbines with differing strut locations to efficiently determine blade stress and deflection magnitudes.
- Computational Requirements: The beam theory models were highly computational efficient when compared to the FEA structural models, as geometrical discretisation was not required. All beam theory models were performed on a standalone desktop computer, with simulation run times of less than 1 minute.

- Limitations of Study and/or Model: The Beam theory can only model simple turbine blade geometries, and cannot be utilised for determining the stress and deflection levels for some turbine geometrical layouts. The predicted stress and deflection results were not validated against EFD, as experiments using strain gauges are rarely, if ever, performed and published. However, given that the DMS and CFD models developed were able to simulate blade forces accurately when compared to the equivalent EFD, it was concluded that simulated stress and deflection levels were of similar accuracy given the simplicity of the force-stress and force-deflection relationships. The beam theory stress and deflection models developed as part of this work can be used in the future for simulations to confirm this hypothesis once suitable EFD results become available.

Finite Element Analysis (FEA) Models

- FEA Models: The use of FEA models enabled the evaluation of structural loading characteristics including stress and deflection magnitudes, with maximum stress magnitudes found at the blade-strut joints. The strength of FEA models when compared to the beam theory model was its ability to model complex geometries such as blade-strut joints, and to allow visualisation of blade loading cycles as the turbine rotates.

- Meshing requirements: The FEA model mesh discretisation requirements were significantly less than that required by the CFD models. Mesh density was found to be critical at the blade-strut joints, with fillets needed to avoid stress singularities.

- Computational Requirements: The FEA models were computationally efficient mainly due to the one-way FSI approach utilised. Thus, a standalone desktop computer was used for all FEA simulations. The one-way FSI approach using transient pressure data files resulted in the need for large computational storage facilities, with each simulation at one rotational rate requiring approximately 0.5TB.

- Limitations of the Study and/or Model: The results from the FEA models were unable to be validated against EFD, as no results were available in the literature. However, the FEA software utilised has been widely verified and validated using standard test cases. Given that the DMS and CFD modes used to generate the loads on the structural were validated, the stress and deflection results should be simulated with similar accuracy given the simplicity of the force-stress and force-deflection relationships. This hypothesis should be confirmed once suitable EFD stress and deflection results become available.

8.3 Future Work

The work performed in this thesis could be extended by:

- Conduct EFD to validate the structural loading calculations using methods outlined in Chapter 7. These EFD studies could be performed by installing strain gauges on the turbine blades and struts. The numerical methods developed as part of this thesis could be utilised to design the EFD turbines and mountings, and determine any limitations that may occur during EFD. Comparison between EFD and the simulationed results would give confidence in both the results obtained using EFD as well as the simulations.

- Using the models developed in this work to perform in-depth analyses of strut and blade-strut connection design. This would enable reductions in maximum stress magnitudes though careful consideration of the structural influence of variations in joint design, as well as the evaluation of the impact of strut and strut-blade joint design on turbine performace. This work would entail the use of FSI modelling techniques with the CFD and FEA models outlined in Chapter 7. Material selection would be a critical component of this work, with the models developed able to simulate most common materials used for turbine construction.

- Use the hydrodynamic and structural models developed in this work to determine the fatigue life-cycle of vertical axis turbines using Miner's law to account for the influence of inflow velocity and rotational rate variations on stress magnitudes, allowing the evaluation of expected longevity.

- As computational power and efficiency increases, simulations using LES, DNS, and laminar-to-turbulent transition models could be performed, with results compared to those reported in this study as well as EFD.

- Perform loading investigations using two-way FSI models and compare results with the one-way FSI simulations. Two-way FSI simulations were estimated to take approximately 140 days to simulate one rotation, due to the fine mesh density and small time step size required for grid independence. Increases in computational efficiency however will reduce simulation timeframes, making two-way FSI simulations feasible.

- Optimisation studies of turbine power output and strucutral loading could be performed using the hydrodynamic and structural loading models developed. This work could be completed in two stages to reduce simulatiuon time using the DMS-Beam theory for initial studies, and the CFD-FEA models for more in-depth analysis.

8.4 Implications for the future

The work outlined in this thesis has demonstrated that the extension of numerical simulation studies from the consideration of power output to more extensive studies of structural variables such as blade stress, deflection, and material selection can now be performed. This extension allows a more holistic approach to turbine design than could previously be performed. Numerical modellers can now concentrate on whole-of-system design, rather than focus on power output, as advances in computational modelling power enable more in-depth investigations of vertical axis turbine designs. This opens up new opportunities to improve design and hence turbine efficiency and longevity.

Vertical axis cross flow turbines are shown in this study to generate power whilst not suffering any significant structural or performance penalties, and thus are suitable for ocean energy deployments. Of the two designs studied in this work, straight-bladed turbines appear promising, as they generate higher power output than helical-bladed turbines, whilst only exhibiting 13% higher stress levels and are simpler to manufacture. Additionally, the benefits of vertical over horizontal axis designs appear to be significant, as due to their geometrical layout all electrical components can be installed above the water surface. Combined with the lack of need for any yawing mechanism, this can ease design, installation and servicing challenges, ensuring simplicity and hence longevity of turbines in ocean environments.

More work is required before the success of vertical axis turbine designs is assured. For example, optimisation studies are required to ensure that the turbines operate as efficiently as possible. This will enable vertical axis designs to generate power output efficiency levels similar to that of on-shore horizontal axis wind turbines. The generation of electrical power using the ocean's kinetic energy opens up huge potential for energy production, as it is both massive and highly predictable. Indeed, the deployment of vertical axis turbines may change our perception of the ocean, from being the source of fossil fuel-based power that is held beneath it, to a source of renewable energy that can be harnessed to power humanity.

REFERENCES

Abbott, I. H. (1959), *Theory of wing sections, including a summary of airfoil data*, Courier Corporation.

Alidadi, M. (2009), Duct optimization for a ducted vertical axis hydro current turbine, PhD thesis, Mechanical Engineering, University of British Columbia.

Anderson Jr, J. D. (1985), *Fundamentals of aerodynamics*, Tata McGraw-Hill Education.

ANSYS (2010*a*), *ANSYS CFX-Solver Thoery Guide Release 13.0*, ANSYS INC.

ANSYS (2010*b*), *ANSYS Meshing User's Guide: Release 13.0*, ANSYS INC.

ANSYS (2010*c*), *ANSYS Meshing User's Guide Release 13.0*, ANSYS INC.

ANSYS (2013), *ANSYS Mechanical User's Guide: Release 15.0*, ANSYS INC.

Area and Bending Inertia of Airfoil Sections (2015).
URL: *http://ocw.mit.edu/courses/aeronautics-and-astronautics*

Arvizu, D., Bruckner, T., Edenhofer, O., Estefen, S., Faaij, A., Fischedick, M. et al. (2011), 'IPCC special report on renewable energy sources and climate change mitigation', *Cambridge University Press Technical Summary* .

Bachant, P. (2011), Experimental investigation of helical cross-flow axis hydrokinetic turbines, including effects of waves and turbulence, MSc thesis, University of New Hampshire.

Bachant, P. & Wosnik, M. (2015), 'Performance measurements of cylindrical-and spherical-helical cross-flow marine hydrokinetic turbines, with estimates of exergy efficiency', *Renewable Energy* **74**, 318–325.

Bahaj, A., Molland, A., Chaplin, J. & Batten, W. (2007), 'Power and thrust measurements of marine current turbines under various hydrodynamic flow conditions in a cavitation tunnel and a towing tank', *Renewable energy* **32**(3), 407–426.

Behrens, S., Griffin, D., Hayward, J., Hemer, A., Knight, C., McGarry, S., Osman, P. & Wright, J. (2012), *Ocean Renewable Energy, 2015-2050: An Analysis of Ocean Energy in Australia*, CSIRO.

Beri, H., Yao, Y. et al. (2011), 'Double multiple streamtube model and numerical analysis of vertical axis wind turbine', *Energy and Power Engineering* **3**(03), 262–270.

Castelli, M. R., Ardizzon, G., Battisti, L., Benini, E. & Pavesi, G. (2010), Modeling strategy and numerical validation for a Darrieus vertical axis micro-wind turbine, *in* 'ASME 2010 International Mechanical Engineering Congress and Exposition', Vancouver, Canada.

Castelli, M. R. & Benini, E. (2012), 'Effect of blade inclination angle on a darrieus wind turbine', *Journal of Turbomachinery* **134**(3), 031016.

Chakroun, W. Al-Mesri, I. & Al-Fahad, S. (2004), 'Effect of surface roughness on the aerodynamic characteristics of a symmetrical airfoil', *Wind Engineering* **28**(5), 547–564.

Chen, Y. (2011), Numerical Simulation of the Aerodynamic Performance of an H-rotor, PhD thesis, University of Louisville.

Choudhry, A., Arjomandi, M. & Kelso, R. (2014), Lift curve breakdown for airfoil undergoing dynamic stall, *in* 'Proceedings of the 19th Australasian Fluid Mechanics Conference', Melbourne, Australia.

Circulating Water Channel (2014).
URL: *http://www.amc.edu.au*

Council, A. W. (2007), *Design Aid No. 6: Beam Formulas with Shear and Moment Diagrams*, American Forrest and Paper Association.

Dai, Y. & Lam, W. (2009), 'Numerical study of straight-bladed Darrieus-type tidal turbine', *ICE-Energy* **162**, 67–76.

Danao, L. (2012), The Influence of Unsteady Wind on the Performance and Aerodynamics of Vertical Axis Wind Turbines, PhD thesis, University of Sheffield.

Drela, M. (1989), *XFOIL: An analysis and design system for low Reynolds number airfoils*, Springer.

Duraisamy, K. & Lakshminarayan, V. (2014), Flow physics and performance of vertical axis wind turbine arrays, *in* '32nd AIAA Applied Aerodynamics Conference, Atlanta, GA'.

Elmiligui, A., Abdol-Hamid, K. S., Massey, S. J. & Pao, S. P. (2004), Numerical study of flow past a circular cylinder using RANS, Hybrid RANS/LES and PANS formulations, *in* '22nd Applied Aerodynamics Conference and Exhibit', Rhode Island, USA.

Ferreira, S. (2009*a*), The near wake of the VAWT: 2D and 3D views of the VAWT aerodynamics, PhD thesis, TU Delft, Delft University of Technology.

Ferreira, S. (2009*b*), The near wake of the VAWT: 2D and 3D views of the VAWT aerodynamics, PhD thesis, Delft University of Technology.

Fraenkel, P. (2010), Development and testing of marine current turbines SeaGen 1.2 MW tidal stream turbine, *in* 'Proc. 3rd International Conference on Ocean Energy', Bilbao, Spain.

Gorlov, A. M. (1998), 'Helical turbines for the gulf stream: conceptual approach to design of a large-scale floating power farm', *Marine Technology* **35**(3), 175–182.

Gorlov, A. M. (2002), The helical turbine and its applications for hydropower without dams, *in* 'ASME 2002 International Mechanical Engineering Congress and Exposition', New Orleans, USA.

Gretton, G. (2009), Hydrodynamic analysis of a vertical axis tidal current turbine, PhD thesis, University of Edinburgh.

Hall, T. J. (2012), Numerical simulation of a cross flow marine hydrokinetic turbine, PhD thesis, University of Washington.

Hameed, M. S. & Afaq, S. K. (2013), 'Design and analysis of a straight bladed vertical axis wind turbine blade using analytical and numerical techniques', *Ocean Engineering* **57**, 248–255.

Iida, A., Kato, K. & Mizuno, A. (2007), Numerical simulation of unsteady flow and aerodynamic performance of vertical axis wind turbines with les, *in* 'Proceedings of the 16th Australasian Fluid Mechanics Conference', Brisbane, Australia.

Islam, M., Ting, D. S.-K. & Fartaj, A. (2008), 'Aerodynamic models for Darrieus-type straight-bladed vertical axis wind turbines', *Renewable and Sustainable Energy Reviews* **12**(4), 1087–1109.

Khalid, S.-s., Zhang, L., Zhang, X.-w. & Sun, K. (2013), 'Three-dimensional numerical simulation of a vertical axis tidal turbine using the two-way fluid structure interaction approach', *Journal of Zhejiang University SCIENCE A* **14**(8), 574–582.

Kiho, S., Shiono, M. & Suzuki, K. (1996), 'The power generation from tidal currents by Darrieus turbine', *Renewable Energy* **9**(1), 1242–1245.

Kirke, B. (2011), 'Tests on ducted and bare helical and straight blade Darrieus hydrokinetic turbines', *Renewable Energy* **36**(11), 3013–3022.

Klimas, P. (1982), 'Darrieus rotor aerodynamics', *Journal of Solar Energy Engineering* **104**, 102–105.

Lain, S. & Osorio, C. (2010), 'Simulation and evaluation of a straight-bladed darrieus-type cross flow marine turbine', *Journal of scientific & industrial research* **69**(12), 906–912.

Leu, T. S., Yu, J., Hu, C., Miau, J., Liang, S., Li, J., Cheng, J. & Chen, S. (2012), 'Experimental study of free stream turbulent effects on dynamic stall of pitching airfoil by using particle image velocimetry', **225**, 103–108.

Li, C., Zhu, S., lin Xu, Y. & Xiao, Y. (2013), '2.5d large eddy simulation of vertical axis wind turbine in consideration of high angle of attack flow', *Renewable Energy* **51**(0), 317–330.

Li, Y. & Çalişal, S. M. (2010*a*), 'Numerical analysis of the characteristics of vertical axis tidal current turbines', *Renewable Energy* **35**(2), 435–442.

Li, Y. & Calisal, S. M. (2010*b*), 'Three-dimensional effects and arm effects on modeling a vertical axis tidal current turbine', *Renewable energy* **35**(10), 2325–2334.

Li, Y., Karri, N. & Wang, Q. (2014), 'Three-dimensional numerical analysis on blade response of a vertical-axis tidal current turbine under operational conditions', *Journal of Renewable and Sustainable Energy* **6**(4), 043123.

Maganga, F., Germain, G., King, J., Pinon, G. & Rivoalen, E. (2010), 'Experimental characterisation of flow effects on marine current turbine behaviour and on its wake properties', *IET Renewable Power Generation* **4**(6), 498–509.

Malipeddi, A. & Chatterjee, D. (2012), 'Influence of duct geometry on the performance of Darrieus hydroturbine', *Renewable Energy* **43**(C), 292–300.

Marine Renewable Energy Technologies (2008).
URL: *www.alaska.gov/mlw/wslca/appendixg/verdantpowermarinerenewables.pdf*

Marsh, P., Ranmuthugala, D., Penesis, I. & Thomas, G. (2012), Three dimensional numerical simulations of a straight-bladed vertical axis tidal turbine, *in* 'Proceedings of the 18th Australasian Fluid Mechanics Conference', Launceston, Australia.

Marsh, P., Ranmuthugala, D., Penesis, I. & Thomas, G. (2014), Numerical simulation of straight-bladed vertical axis turbines, *in* '2nd Asian Wave and Tidal Energy Conference', Tokyo, Japan.

Marsh, P., Ranmuthugala, D., Penesis, I. & Thomas, G. (2015*a*), 'Numerical investigation of the influence of blade helicity on the performance characteristics of vertical axis tidal turbines', *Renewable Energy* **81**, 926–935.

Marsh, P., Ranmuthugala, D., Penesis, I. & Thomas, G. (2015*b*), 'Three-dimensional numerical simulations of straight-bladed vertical axis tidal turbines investigating power output, torque ripple and mounting forces', *Renewable Energy* **83**, 67–77.

Marsh, P., Ranmuthugala, S., Penesis, I. & Thomas, G. (2013), 'Performance predictions of a straight-bladed vertical axis turbine using double-multiple streamtube and computational fluid dynamics models', *Journal of Ocean Technology* **8**(1), 86–103.

Masson, C., Leclerc, C. & Paraschivoiu, I. (1998), 'Appropriate dynamic-stall models for performance predictions of vawts with nlf blades', *International Journal of Rotating Machinery* **4**(2), 129–139.

Matre, T., Amet, E. & Pellone, C. (2013), 'Modeling of the flow in a darrieus water turbine: Wall grid refinement analysis and comparison with experiments', *Renewable Energy* **51**(C), 497–512.

McLaren, K. (2011), A numerical and experimental study of unsteady loading of high solidity vertical axis wind turbines, PhD thesis, McMaster University.

Menter, F. R. (1994), 'Two-equation eddy-viscosity turbulence models for engineering applications', *AIAA Journal* **32**(8), 1598–1605.

Mittal, S. & Kumar, B. (2003), 'Flow past a rotating cylinder', *Journal of Fluid Mechanics* **476**, 303–334.

Navabi, Y. (2008), Numerical Study of the Duct Shape Effect on the Performance of a Ducted Vertical Axis Tidal Turbine, Masters thesis, University of British Columbia.

New Energy Corporation (2014).
URL: *http://www.newenergycorp.ca*

Niblick, A. L. (2012), Experimental and analytical study of helical cross-flow turbines for a tidal micropower generation system, PhD thesis, University of Washington.

Nobile, R., Vahdati, M., Barlow, J. & Mewburn-Crook, A. (2011), 'Dynamic stall for a vertical axis wind turbine in a two-dimensional study', *World Renew. Energ. Congr* pp. 4225–4232.

OpenHydro (2015).
URL: *http://www.fundyforce.ca/technology/openhydro-nova-scotia-power/*

Osman, P., Behrens, S., Griffin, D., Hayward, J., Hemer, M., Knight, C., McGarry, S. & Wright, J. (2011), Ocean renewable energy: 2015–2050, Technical report, Commonwealth Scientific and Industrial Research Organisation (CSIRO).

Paraschivoiu, I. (2002), *Wind Turbine Design: With Emphasis on Darrieus Concept*, Polytechnic International Press.

Paraschivoiu, I., Dy, N. V. et al. (2012), A numerical study of Darrieus water turbine, *in* 'The Twenty-second International Offshore and Polar Engineering Conference', Rhodes, Grece.

Rawlings, G. (2008), Parametric Characterization of an Experimental Vertical Axis Hydro Turbine, PhD thesis, Mechanical Engineering, University of British Columbia.

Rawlings, G., Alidadi, M., Klaptocz, V., Nabavi, Y., Li, Y., Mikkelsen, J., Calisal, S. et al. (2008), Application of end plates for vertical axis hydro turbine performance enhancement, *in* 'Proceedings of the Eighteenth International Offshore and Polar Engineering Conference', Vancouver, Canada.

Reuter, R., of Energy, U. S. D. & Laboratories, S. (1980), *Torque Ripple in a Darrieus, Vertical Axis Wind Turbine*, Sandia Laboratories, New Mexico, USA.

Rossetti, A. & Pavesi, G. (2013), 'Comparison of different numerical approaches to the study of the h-darrieus turbines start-up', *Renewable Energy* **50**(C), 7–19.

Scheurich, F., Fletcher, T. M. & Brown, R. E. (2011), 'Simulating the aerodynamic performance and wake dynamics of a vertical-axis wind turbine', *Wind Energy* **14**(2), 159–177.

Sheldahl, R., Klimas, P., of Energy, U. S. D. & Laboratories, S. N. (1981), *Aerodynamic Characteristics of Seven Symmetrical Airfoil Sections Through 180-degree Angle of Attack for Use in Aerodynamic Analysis of Vertical Axis Wind Turbines*, Sandia National Laboratories, New Mexico, USA.

Shiono, M., Suzuki, K. & Kiho, S. (2002), Output characteristics of darrieus water turbine with helical blades for tidal current generations, *in* 'Proceedings of the Twelfth International Offshore and Polar Engineering Conference', Kitakyushu, Japan.

Sørensen, N. N. (2009), 'CFD modelling of laminar-turbulent transition for airfoils and rotors using the γ- model', *Wind Energy* **12**(8), 715–733.

Strickland, J., Webster, B. & Nguyen, T. (1979), 'A vortex model of the darrieus turbine: an analytical and experimental study', *Journal of Fluids Engineering* **101**(4), 500–505.

Sutherland, H. J., Berg, D. E. & Ashwill, T. D. (2012), 'A retrospective of VAWT technology', *Sandia Report, SAND2012* **304**.

Templin, R. (1974), 'Aerodynamic performance theory for the nrc vertical-axis wind turbine', *NASA STIRecon Technical Report* **76**(LTR-LA-160).

Thomson, J., Polagye, B., Richmond, M. & Durgesh, V. (2010), Quantifying turbulence for tidal power applications, *in* 'OCEANS 2010', Seattle, USA.

Tsai, J.-S. & Chen, F. (2014), 'The conceptual design of a tidal power plant in Taiwan', *Journal of Marine Science and Engineering* **2**(2), 506–533.

Tu, J., Liu, C. & Yeoh, G. H. (2013), *Computational fluid dynamics : a practical approach / Jiyuan Tu, Guan-Heng Yeoh, Chaoqun Liu*, 2nd ed. edn, Butterworth-Heinemann/Elsevier Waltham, MA.

T-Vision (2015).
URL: *http://www.ropatec.it/content/T-Vision/9/en*

Update on AK1000 blade replacement (2015).
URL: *www.atlantisresourcesltd.com/media-centre/atlantis-annoucements/74-2010-annoucements/123-december-3rd-2010-update-on-ak1000-blade-replacement.html*

Veers, P. S. (1981), *An Approach to the Fatigue Analysis of Vertical Axis Wind Turbine Blades*, Sandia National Laboratories.

Vertical Axis Wind Turbines vs Horizontal Axis Wind Turbines (2015).
URL: *http://www.windpowerengineering.com/construction/vertical-axis-wind-turbines-vs-horizontal-axis-wind-turbines*

Webster, B. T. (1978), An experimental study of an airfoil undergoing cycloidal motion, PhD thesis, Texas Tech University.

Winchester, j. & Quayle, S. (2011), Torque ripple and power in a variable pitch vertical axis tidal turbine, *in* 'Proceedings of the 9th European Wave and Tidal Conference', Southampton, United Kingdom.

Appendix A

Three Dimensional Numerical Simulations of a Straight-Bladed Vertical Axis Tidal Turbine

This refereed journal paper was published in the *Journal of Ocean Technology*. The citation for this journal paper is:

Marsh, P and Ranmuthugala, D and Penesis, I & Thomas, G., Performance predictions of a straight-bladed vertical axis turbine using double-multiple streamtube and computational fluid dynamic models, *Journal of Ocean Technology*, 8 (1) (2013) pp. 87-103.

Appendix B

Performance Predictions of a Straight-Bladed Vertical Axis Turbine Using Double-Multiple Streamtube and Computational Fluid Dynamics Models

This refereed conference paper was published in the Proceedings of the 18^{th} Australasian Fluid Mechanics Conference. The citation for this conference paper is:

Marsh, P and Ranmuthugala, D and Penesis, I and Thomas, G, Three dimensional numerical simulations of a straight-bladed bertical axis tidal turbine, *Proceedings of the 18th Australasian Fluid Mechanics Conference*, 3-7 December 2012, Lauceston, Tasmania, Australia, pp. 1-4. ISBN 9780646583730 (2012).